EXPERIMENTAL INVESTIGATION ON PERMEABILITY ENHANCEMENT DUE TO ROCK FAILURE USING ROCK BRITTLENESS QUANTIFICATION

A Dissertation

by

JIHOON WANG

Submitted to the Office of Graduate and Professional Studies of
Texas A&M University
in partial fulfillment of the requirements for the degree of

DOCTOR OF PHILOSOPHY

Chair of Committee,	Peter Valko
Committee Members,	Jerome Schubert
	Eduardo Gildin
	Yuefeng Sun
Head of Department,	A. Daniel Hill

December 2017

Major Subject: Petroleum Engineering

ABSTRACT

Brittleness index is the rock failure property frequently used to predict the efficiency of the fracturing process in unconventional reservoir development. Although there have been various approaches in the brittleness quantification and its application, research on the relation of brittleness and permeability enhancement is hardly available. In this study, we analyze the ability of the various brittleness indices to predict the permeability enhancement observed in the laboratory scale.

Brittleness characterization approaches related to unconventional reservoirs were reviewed. Focusing on the laboratory scale, the multistage triaxial testing method was adopted to measure the rock properties without heterogeneity effect over the rock specimens.

Prior to the permeability measurement, the effect of the heterogeneity of the rock specimen was computationally analyzed. The permeability enhancement due to failure can be reliably obtained from the newly introduced characteristic time ratio measured before and after failure, even if the rock specimen is heterogeneous.

Rock property measurement tests were performed on 15 rock specimens including Newberry tuffs, Mancos shales and Middle East carbonates. It was found that the rock dilatancy and pre-existing natural fractures have influences on the failure properties, such as internal friction angle.

The nonlinear behavior on the stress-strain curves were computationally approached with finite element method. The local Poisson's ratio was approximately formulated for both dilatant and non-dilatant rock specimens.

19 brittleness index theories were reviewed. Based on the availability of the measured data and the consistency of the calculated values, 4 indices were selected for further analysis. The brittleness index for each rock specimen was calculated by the selected theories.

The selected brittleness indices were calculated from the measured properties and were related to the permeability enhancement ratio. The results show that the brittleness indices determined from the stress-strain curve and the Mohr-Coulomb failure property are more predictive than the others.

DEDICATION

To Eunmi

ACKNOWLEDGEMENTS

I would like to thank my advisor Dr. Valko, for his valuable advice which allowed my research to focus on practical application. Moreover, I would also like to mention that his passion in research and teaching provided me important virtues for my future career. And I could overcome the hardships with his emotional and financial support.

I also appreciate my committee members, Dr. Schubert, Dr. Gildin and Dr. Sun for the acute and brilliant comments. With their time and concern, my thought and knowledge could be more plentiful.

At last, it should be mentioned that a part of the dissertation has been accepted for publication in forthcoming issue of *International Journal of Oil, Gas and Coal Technology*.

CONTRIBUTORS AND FUNDING SOURCES

This work was supervised by a dissertation committee consisting of Dr. Valko, Dr. Schubert and Dr. Gildin of the Department of Petroleum Engineering and Dr. Sun of the Department of Geology.

This study was supported by Crisman Institute for Petroleum Research. Additional financial support was received from the Petroleum Engineering department as a teaching assistantship.

NOMENCLATURE

a_s	Ratios of pore volume of the specimen to the upstream volume
A [L^2]	Cross-sectional area of rock specimen
A_u [$ML^{-1}T^{-2}$]	Pressure amplitude at upstream vessel
A_d [$ML^{-1}T^{-2}$]	Pressure amplitude at downstream vessel
b_s	Ratios of pore volume of the specimen to the downstream volume
BI	Brittleness index or indices
c_g [$M^{-1}LT^2$]	Gas compressibility
C [$ML^{-1}T^{-2}$]	Pure shear strength
dW_r [$ML^{-1}T^{-2}$]	Post-peak rupture strain energy,
dW_e [$ML^{-1}T^{-2}$]	Withdrawn elastic strain energy
dW_α [$ML^{-1}T^{-2}$]	Released strain energy
D [L]	Specimen diameter
E [$ML^{-1}T^{-2}$]	Young modulus (or unloading elastic modulus)
F_R	Ratio of remaining gas over total gas taken by the rock specimen
FEM	Finite Element Method
H_u	Micro indentation hardness
H	Macro indentation hardness
IFA [°]	Internal friction angle
k [L^2]	Permeability
k_0 [L^2]	Permeability at reference condition

k_{post} [L^2]	Permeability of the rock specimen after failure
k_{pre} [L^2]	Permeability of the rock specimen before failure
K_a	Partial derivative of adsorbate density with respect to gas density
L [L]	Length of rock specimen
L_d [L]	Length of downstream vessel
L_u [L]	Length of upstream vessel
M [$ML^{-1}T^{-2}$]	Post-peak modulus
p_d [$ML^{-1}T^{-2}$]	Downstream pressure
p_D	Dimensionless pressure
p_{final} [$ML^{-1}T^{-2}$]	Final stabilized pressure
p_{pulse} [$ML^{-1}T^{-2}$]	Pulse pressure located at the upstream volume
p_u [$ML^{-1}T^{-2}$]	Upstream pressure
Δp_0 [$ML^{-1}T^{-2}$]	Initial step change in the upstream pressure
Δp_D	Dimensionless pressure difference
Pc [$ML^{-1}T^{-2}$]	Confining pressure
q	Percentage of fines formed (-28 mesh) in the test
R_a [L]	Diameter of a spherical particle
s_1	Slope of $\ln(F_R)$ vs. square root of dimensionless time at late-time
S_{max} [$ML^{-1}T^{-2}$]	Maximum in-situ stress
t_{ch} [T]	Characteristic time
$t_{ch,post}$ [T]	Characteristic time after failure
$t_{ch,pre}$ [T]	Characteristic time before failure

t_D	Dimensionless time
T [T]	Period of oscillation
UCS [$ML^{-1}T^{-2}$]	Unconfined compressive strength
V_s [L^3]	Bulk volume of the rock specimen
V_u [L^3]	Upstream volume
V_d [L^3]	Downstream volume
W_e [$ML^{-1}T^{-2}$]	Elastic strain energy
W_{ir} [$ML^{-1}T^{-2}$]	Pre-peak irreversible strain energy
W_r [$ML^{-1}T^{-2}$]	Reversible strain energy
W_T [$ML^{-1}T^{-2}$]	Total strain energy
x_D	Dimensionless length
β	Ratio of pore volume of specimen to upstream volume
γ	Power law index for axial strain
δ	Power law index for lateral strain
δ_{ND}	Power law index of non-dilatant rock
ε_a	Axial strain
$\varepsilon_{a,dil}$	Axial strain at dilatancy point
$\varepsilon_{a,ND}$	Axial strain of non-dilatant rock at stopping point
ε_e	Elastic strain
ε_l	Lateral strain
$\varepsilon_{l,dil}$	Lateral strain at dilatancy point
$\varepsilon_{l,ND}$	Lateral strain of non-dilatant rock at stopping point

ε_P	Post-peak strain
ε_r	Reversible strain
ε_V	Volumetric strain
ε_T	Total strain
ε_{Tp}	Total irreversible post-peak strain
θ_u [°]	Pressure oscillating phase of upstream vessel
θ_d [°]	Pressure oscillating phase of downstream vessel
μ [$ML^{-1}T^{-1}$]	Gas viscosity
ν	Poisson's ratio
ν_{local}	Local Poisson's ratio
$\nu_{local,ND}$	Local Poisson's ratio of non-dilatant rock at stopping point
σ [$ML^{-1}T^{-2}$]	Normal stress
σ_1 [$ML^{-1}T^{-2}$]	Maximum principal stress
σ_3 [$ML^{-1}T^{-2}$]	Minimum principal stress
σ_c [$ML^{-1}T^{-2}$]	Compressive strength
σ_{dil} [$ML^{-1}T^{-2}$]	Stress at dilatancy point
σ_D [$ML^{-1}T^{-2}$]	Deviatoric stress, $\sigma_1 - \sigma_3$
σ_m [$ML^{-1}T^{-2}$]	Mean normal stress
σ_{ND} [$ML^{-1}T^{-2}$]	Stress at stopping point
σ_n [$ML^{-1}T^{-2}$]	Normal stress
σ_t [$ML^{-1}T^{-2}$]	Tensile strength
τ [$ML^{-1}T^{-2}$]	Shear stress

τ_m [$ML^{-1}T^{-2}$]	Maximum shear stress
ϕ	Porosity
ϕ_0	Porosity at reference condition
φ [°]	Internal friction angle.
ψ [$M^2L^{-2}T^{-4}$]	Pressure square
ω [$M^{-1}LT^2$]	Storage capacity of specimen
ω_d [$M^{-1}LT^2$]	Storage capacity of downstream vessel

TABLE OF CONTENTS

Page

LIST OF FIGURES

Page

LIST OF TABLES

Page

1. INTRODUCTION

Unconventional resources have been recently focused by the energy industry. Especially, shale plays have led the energy revolution by changing the geographical map of the energy supply and demand. Taking advantage of the shale plays, the U.S. has become not only the biggest crude producer, but also a crude exporter. The revolution began with the efficient production from shale reservoirs which had not been seen as commercial hydrocarbon source due to the ultra-low permeability. Most often shale was considered as a cap rock preventing the hydrocarbon migration out of the reservoir because it was thought to be impermeable.

The concept of the shale has changed from cap rock or source rock into potentially commercial reservoir by the revolutionary technology, known as hydraulic fracturing. Applying the fracturing process to the ultra-low permeability reservoirs, it is possible to enhance the fluid transport property by creating a new flow path and to enlarge the drainage volume of a well. While current ultimate recoveries are still low compared to traditional reservoirs, they have grown by orders of magnitude. Therefore, the effectiveness of the fracturing process is one of the key factors in the unconventional reservoir development. In order to assess the efficiency and to optimize the fracturing treatments, the reservoir needs to be properly characterized with respect to its response to fracturing.

Unconventional resources are difficult to characterize due to many reasons. Their distinctive characteristics such as nanoscale pores, adsorptive kerogen, heterogeneity,

etc. hinder the traditional methods and procedures of reliable characterization (Chen et al., 2015). Moreover, even the laboratory measurement of core permeability, which used to have a distinguished role in traditional petroleum engineering, is much less informative when developing unconventional resources. In an attempt to obtain reliable rock properties in the lab scale, many researchers have proposed improved methods and procedures.

Another question to be answered by engineers and geologists is if it were possible to predict the fracturing efficiency in the unconventional reservoir prior to spending enormous development cost. The concept of the rock brittleness has been frequently used as a tool to answer this question. This is because it is widely accepted that brittle rocks are failed with a set of induced or re-opened micro fractures and this enhances the rock's ability to conduct flow. If quantitatively determined, it would suggest valuable information in establishing the unconventional reservoir development plan.

In spite of a number of attempts made to establish a reliable brittleness quantification method, its concepts are still far from consensus, except the representative characteristic of the brittle rocks. Researchers have taken an indirect route to present the 'index' theory instead of directly quantifying the rather qualitative failure behavior, i.e. failure with fractures. Determining the rock properties representing the failure behavior, the quantification can be achieved by constructing formula with the representative properties. In other words, each brittleness index theory contains the author's insight about what kind of a rock is most likely to be failed with sets of fractures.

Based on the data obtained from the laboratory scale (Bergman and Stille, 1983, Coates and Parsons, 1966, He et al., 1990, Hucka and Das, 1974, Tarasov, 2011) or the near-wellbore scale (Rickman et al., 2008), the authors suggested that the brittle rock would have higher reversible strain before than after failure, higher ratio of compressive to tensile strength, higher Young modulus, lower Poisson's ratio, lower clay content, etc. By constructing a formula with the characteristics above, some widely used brittleness index equations were derived to predict the achievable productivity from the hydraulically fractured reservoirs.

Although each theory is based on the observations obtained from the laboratory or logs, the linkage between the index and the actual brittleness is ambiguous. In the meantime, Altindag (2003) and Yarali and Soyer (2011) suggested a brilliant approach in brittleness index verification. Instead of trying to link the brittleness index with the failure behavior of rock, they focused on their final goal, to estimate the drillability in various rocks. They measured rock properties and the drillability from the same rock specimens and calculated 3 brittleness indices from the measured properties. Comparing the drillability and the brittleness indices, they selected the most applicable index in the drillability estimation.

In unconventional resource development, the brittleness index takes a major role to assess the effectiveness of the hydraulic fracturing treatment. Since it is not practically available to direct link the index and the actual brittleness, we would like to focus on the primary objective of the fracturing process, to establish the "stimulated reservoir volume" with "enhanced permeability" compared to the virgin state of the formation.

In this study, our main objective is to determine the relationship between the permeability enhancement due to rock failure and the brittleness indices. In order to pursue the main objective, we proceed in the following steps

1) review the geomechanical properties and permeability characterization methods in the laboratory scale,

2) perform the computational approach to analyze the rock heterogeneity effect during the permeability measurement,

3) experimentally measure the properties from various rocks by multistage triaxial testing method,

4) calculate the various brittleness indices suggested in the literature from measured rock properties,

5) measure the permeability of the rock specimens before and after failure and

6) analyze the ability of the various brittleness indices to predict the permeability enhancement observed on the same laboratory scale.

2. LITERATURE REVIEW

Laboratory measurement of rock properties takes a distinguished role in reservoir characteristics. Although the outcomes obtained from the laboratory scale measurement are more reliable, the scale cannot solely represent the characteristics of the field. Therefore, a few inch scale data is generally extended by correlating with larger scale data. However, unconventional reservoirs are not as simply interpretable as conventional reservoirs even in the lab scale. Despite of the enormous investments made, operators are still at the beginning of understanding unconventional reservoir characterization (Prasad et al., 2015).

In the literature review section, we will briefly review the difficulties in characterization of unconventional reservoirs and the proposed methods to strengthen the reliability of the lab scale measurements, including the permeability measurement methods. Furthermore, we review brittleness quantification methods developed for various purposes.

2.1 Application of Lab Scale Measurement in Unconventional Reservoir Development

Laboratory scale characterization of rock is crucial for any type of reservoir development. The properties measured in the lab are credible blue-prints for determining rock mechanical properties, porosity, permeability, petrophysical properties and anisotropy (Josh et al., 2012).

However, to characterize unconventional reservoirs in the lab scale is more challenging and complicated than conventional reservoirs. For instance, the pore structure and distribution, which are the core data for reserve estimation, mechanical and transport properties determination, are very difficult to be generalized because of its complexity and nanometer scale (Ross and Bustin, 2008).

The rock specimens are usually limited to a few depths and are commonly insufficient to generate reliable statistics (Prasad et al., 2015). Thus, the size and scale of the lab tests would also cause the misleading results (Brezovski and Cui, 2013). The unreliability is more severe for the tight and low permeability rocks, because the nonuniformly distributed natural fracture has significant effect on the rock mechanical and fluid transport properties (Kovaleva, 1974, Ning et al., 1993). Therefore, applying the conventional characterization tools and procedures in the unconventional rocks yield erroneous results (Chen et al., 2015).

In order to overcome the difficulties, the researchers have been focusing on revising the conventional procedures and tools for application in the unconventional reservoirs.

Brezovski and Cui (2013) performed permeability measurement experiments on Montney shale specimens and insisted that the multiple specimens with different directions need to be tested to examine the anisotropy effect. They also pointed out it is necessary to verify the existence of natural fracture in the specimen for better integrity of the results. Kamath et al. (1992) performed experiments on specimens with transverse and longitudinal heterogeneity. Under various upstream and downstream vessel

volumes, they found that the transverse heterogeneity can be detected on the early time pressure behavior. Ning et al. (1993) derived a modified analytical solution for the low permeability rock specimen which contains high conductive fracture. The results show that the early time pressure behavior can be used to identify the fracture existence.

Islam and Skalle (2013) recommended to perform CT scan on the specimen prior to the property measurement in attempt to assign the effect of irregularity. Tran et al. (2010) suggested the multistage triaxial testing method in rock mechanical property measurement in order to avoid misinterpretation caused by heterogeneity. Britt and Schoeffler (2009) suggested and recommended the ultrasonic wave velocity measurement during the triaxial test to enhance the correlation process from the static properties to the dynamic properties.

Prasad et al. (2015) insisted that not only the reliability on the lab scale data, but the accuracy of the larger scale data including near-wellbore scale and field scale measurement is also important to characterize the reservoir. Emphasizing the pore-dependent logs are not sensitive enough to gather the unique characteristics of shale, they pointed out that the integrated analysis is required for the more reliable unconventional reservoir characterization.

2.2 Permeability Measurement in Low Permeability Rock

To determine the transport properties of the reservoir is one of the key processes in the reservoir productivity estimation. Although there are several indirect permeability

measurement methods applicable in larger scale, the direct measurement in the lab is more reliable (Sander et al., 2017).

The permeability measurement methods on the lab scale can be categorized into steady state and unsteady state methods. In general, the unsteady state methods are considered appropriate for low permeability rock because the results can be obtained in shorter time (Cui et al., 2009). In this section, we will review the commonly used unsteady state permeability measurement methods, i.e. the pulse decay method, the GRI method and the oscillating pressure method.

The pulse decay permeability measurement method firstly proposed by Brace et al. (1968) is the most widely used method on low permeability rocks (Sander et al., 2017). The method has been modified and improved by many researchers, including experimental designs, analysis techniques, etc. (Feng et al., 2017, Kamath et al., 1992, Lin et al., 1986).

Figure 1 shows the pressure behavior in the system during the permeability measurement. The initial pressure pulse located at the upstream vessel starts to move through the rock specimen. The pressure in the upstream and downstream vessels is continuously recorded until the pressure is completely stabilized.

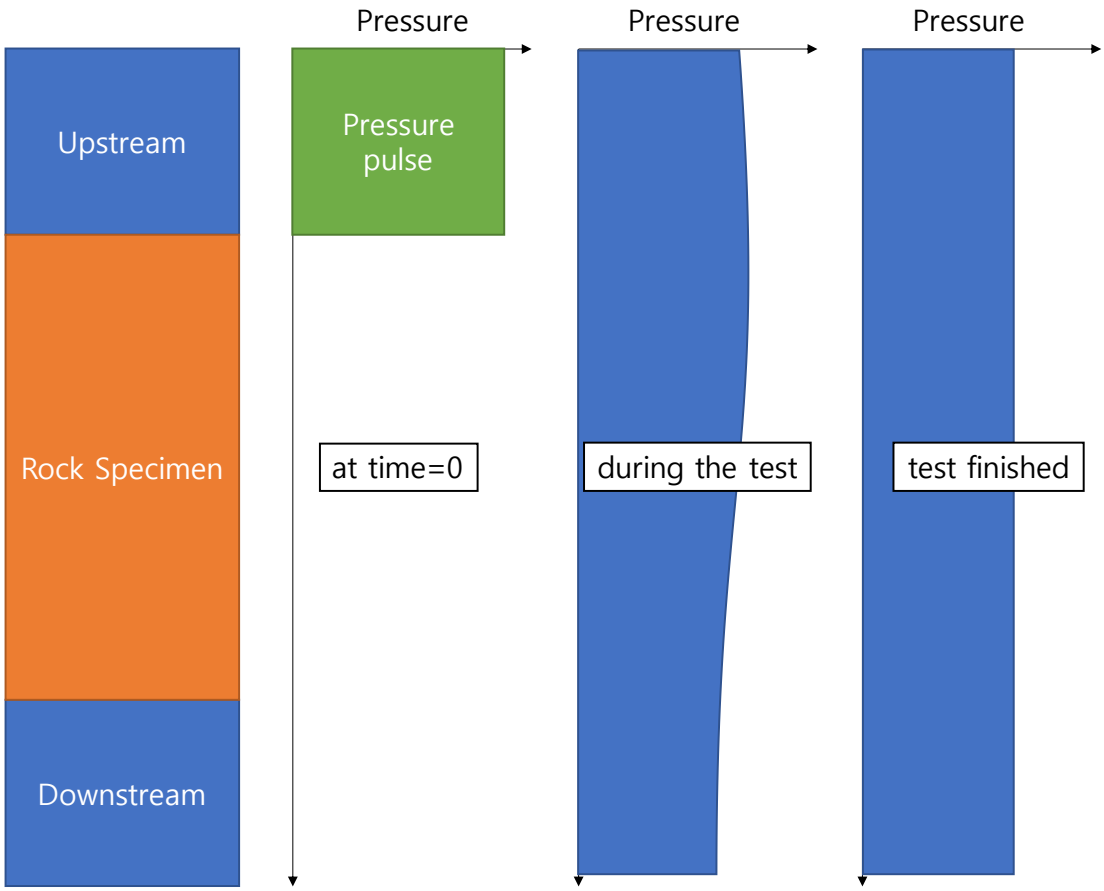

Figure 1. Pressure behavior of the pulse decay permeameter during permeability measurement test.

Assuming that the pressure gradient in the specimen is constant, Brace et al. (1968) derived the approximate solution for the permeability measurement.

$$(p_u - p_{final}) = \Delta p_0 \cdot \frac{\mathrm{V}_d}{V_u + V_d} \cdot e^{-\alpha t} \tag{2.1}$$

where, p_u is the upstream pressure, p_{final} is the final stabilized pressure at the same location, Δp_0 is the initial step change in the upstream pressure, V_u and V_d are the upstream and downstream volume, respectively. Then, the permeability of the rock specimen is calculated by the α value with the equation given by,

$$k = -\frac{\alpha \mu c_g L}{A\left(\frac{1}{V_u} + \frac{1}{V_d}\right)} \tag{2.2}$$

where, μ is the gas viscosity, c_g is the gas compressibility, A and L are the cross-sectional area and length of the rock specimen

Dicker and Smits (1988) derived a modified analytical solution of the pressure difference between the upstream and downstream during the test.

$$\Delta p_D = 2\sum_{n}^{\infty} \frac{a_s(b_s^2 + \theta_n^2) - (-1)^n b_s \sqrt{(a_s^2 + \theta_n^2)(b_s^2 + \theta_n^2)}}{\theta_n^2(\theta_n^2 + a_s + a_s^2 + b_s + b_s^2) + a_s b_s(a_s + b_s + a_s b_s)} \cdot \exp(\theta_n^2 \cdot t_D) \tag{2.3}$$

where, Δp_D is the dimensionless pressure difference given by,

$$\Delta p_D(t_D) = \frac{\left(p_u(t_D) - p_d(t_D)\right)}{\left(p_u(0) - p_d(0)\right)} = \frac{\Delta p}{\Delta p_0} \tag{2.4}$$

and where, θ_n is the nth root of the equation given by,

$$\tan\theta = \frac{(a_s + b_s)\theta}{(\theta^2 - a_s b_s)} \tag{2.5}$$

where, a_s and b_s are the ratios of pore volume of the specimen (V_p) to the upstream and downstream volume.

$$a_s = \frac{V_p}{V_u} \tag{2.6}$$

$$b_s = \frac{V_p}{V_d} \tag{2.7}$$

Here the dimensionless time is given by,

$$t_D = \frac{kt}{\mu\phi c_f L^2} \tag{2.8}$$

GRI method is a modified version of the pulse decay permeability measurement method. Instead of placing two vessels at both ends of the specimen, only the upstream vessel is used (Figure 2). The method was firstly developed to measure the permeability of crushed sample from drill cutting (Luffel and Guidry, 1992) and was modified to apply to the intact core specimen (Brezovski and Cui, 2013). Since the GRI method using the crushed sample can be used to measure the adsorption ability of rock, it has gained popularity in application to adsorptive rocks, such as shale and coal.

During the permeability analysis, either early time or late time techniques can be applied. Based on the results from numerical analyses, Cui et al. (2009) recommended usage of the late time technique as below.

$$\mathrm{k} = \frac{R_a^2[\phi + (1-\phi)K_a]\mu c_g s_1}{(\alpha_1)^2} \tag{2.9}$$

where, R_a is the diameter of a spherical particle, K_a is the partial derivative of adsorbate density with respect to gas density, s_1 is the slope of the straight-line portion of $\ln(F_R)$ versus square root of dimensionless time at late-time, F_R is the ratio of remaining gas over total gas taken by the rock specimen and α_1 is the first root of the equation given by,

$$\tan\alpha = \frac{3\alpha}{3 + K_c\alpha^2} \tag{2.10}$$

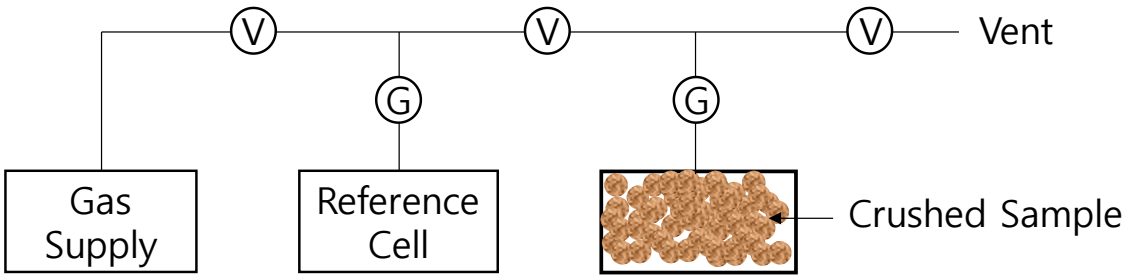

Figure 2. Schematic diagram for GRI method. The valves and gauges are marked as "V" and "G", respectively.

The oscillating pressure method was developed by Kranz et al. (1990) and Fischer (1992). With similar experimental system to the pulse decay permeameter, the pressure at the one edge of the specimen oscillates with specific amplitude and frequency. Transmitted through the rock specimen, the pressure at the other edge would have a shifted phase and a smaller amplitude (Figure 3). The permeability can be calculated from the equation

$$A_R \cdot e^{-i\theta_s} = \left(\frac{1+i}{\sqrt{\beta_D k_D}} \sinh\left[(1+i)\sqrt{\frac{\beta_D}{k_D}} \right] + \cosh\left[(1+i)\sqrt{\frac{\beta_D}{k_D}} \right] \right)^{-1} \tag{2.11}$$

where, the amplitude ratio (A_R) and the phase shift (θ_S)

$$A_R = \frac{A_d}{A_u} \tag{2.12}$$

$$\theta_S = \theta_d - \theta_u \tag{2.13}$$

where, A_u and A_d are the pressure amplitude at the upstream and downstream vessels and θ_u and θ_d are the phase of the upstream and downstream vessels, respectively. The dimensionless storage capacity and dimensionless permeability are given by,

$$\omega_D = \frac{AL\omega}{\omega_d} \tag{2.14}$$

$$k_D = \frac{ATk}{\pi L \mu \omega_d} \tag{2.15}$$

where, ω and ω_d are the specimen and downstream storage capacity and T is the period of the oscillation.

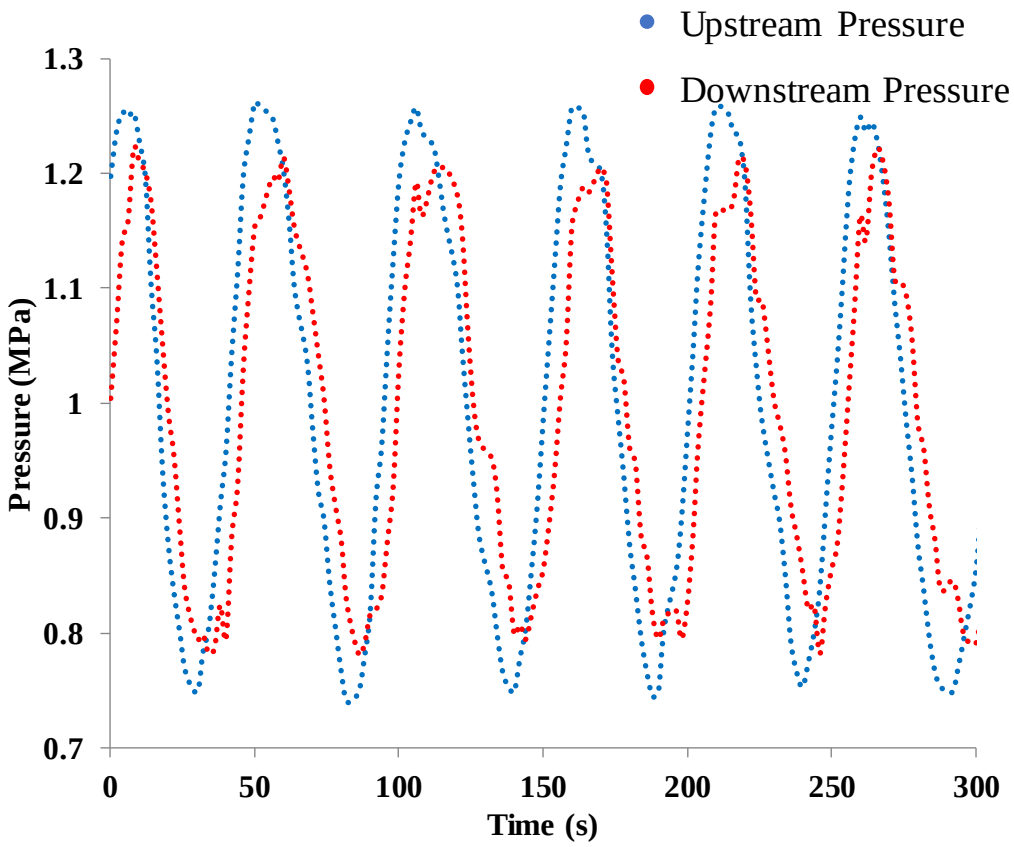

Figure 3. Pressure behavior during oscillating pressure permeability measurement test on a Berea sandstone.

2.3 Rock Brittleness Quantification Method

In unconventional reservoir development, the concept of brittleness is significantly important. This is because it is widely accepted that brittle rock is failed with sets of induced fractures and complex geometry, which ultimately improves the reservoir productivity by generating high conductive flow paths. Once properly and reliably established, the rock brittleness quantification method would be the valuable tool to predict the failure behavior of rocks and the productivity of the reservoir.

However, neither has the definition of the rock brittleness met consensus, nor is a direct measurement method available. Consequently, researchers have attempted to calculate the brittleness indirectly. The first step taken is to determine the rock properties representing the brittle behavior. Then, the brittleness can be quantified by a specific formula consisting of the chosen properties with weighting factor in accordance with the author's insight. Therefore, each index theory is based on a somewhat subjective judgement.

In an attempt to quantify the brittleness on the lab scale, the stress-strain curve has been widely applied (Bergman and Stille (1983), Coates and Parsons (1966), He *et al.* (1990), Hucka and Das (1974), Tarasov (2011)). Focusing on the stress-strain behavior of rock under external stress, the researchers assumed that the absorbed strain energy by the rock is quickly released by creation of a set of micro fractures. Instead of sudden release of the absorbed energy, a ductile rock shows plastic strain that is considerably larger than typical brittle strain.

Altindag (2003) supposed that brittle rocks have higher ratio of compressive to tensile strength and suggested three formulas. Su et al. (2014) also focused on the rock strength and insisted that brittle rocks would have higher unconfined compressive strength. In addition, they insisted that the result would be more reliable if the maximum in-situ stress is taken into account. Hucka and Das (1974) assumed that higher brittle rocks have the higher internal friction angle.

The brittleness index proposed by Rickman et al. (2008) would be one of the most widely used in the field of petroleum engineering with advantages, such as the simplicity of the method and the availability of the data. Insisting that brittle rocks have higher Young modulus and lower Poisson's ratio, they presented a brittleness quantification formula using both elastic properties of the rock.

On the other hand, Jarvie et al. (2007) and Wang and Gale (2009) suggested methods using the mineral composition of the rock. They assumed that the silica mineral would increase the brittleness and the clay and calcite would negatively affect the brittleness.

More detailed information about the quantification methods including equations, advantages and disadvantages will be provided in section 7.

3. MULTISTAGE TRIAXIAL COMPRESSION TEST

The triaxial compression testing method has become one of the most widely used methods in rock mechanical property measurement since von Kármán firstly proposed experimental results from a triaxial test (Vásárhelyi, 2010). In the field of petroleum engineering, the primary objectives of the method are to determine how much strength is required for the rock failure and to estimate how much deformation the rock gains under specific stress level. The testing system consists of an axial loading actuator, a confining pressure cell, strain gauges and a data acquisition device. The stress-strain response of the rock specimen under desired pressure condition is acquired and the obtained data is used to calculate the parameters.

In order to determine rock properties representing the behavior with depth, it requires multiple rock specimens. For example, if we are interested in construction of the failure envelope, at least 2 rock specimens need to be tested separately under different confining pressure conditions.

However, when heterogeneity over the specimens is significant, the reliability of the data is undermined. Figure 4 shows the Mohr-Coulomb failure envelope determined by Mohr circles obtained from sets of triaxial tests. It can be seen that the heterogeneity over the specimens yields unreliable results when separate triaxial tests are performed.

A new approach named “Multistage Test”, proposed by Kovari et al. (1983), allows us to minimize the effect of heterogeneity over the rock specimens and to

overcome the unreliability. In this section, we are going to overview the multistage triaxial testing method, including theories, procedures and interpretation of the results.

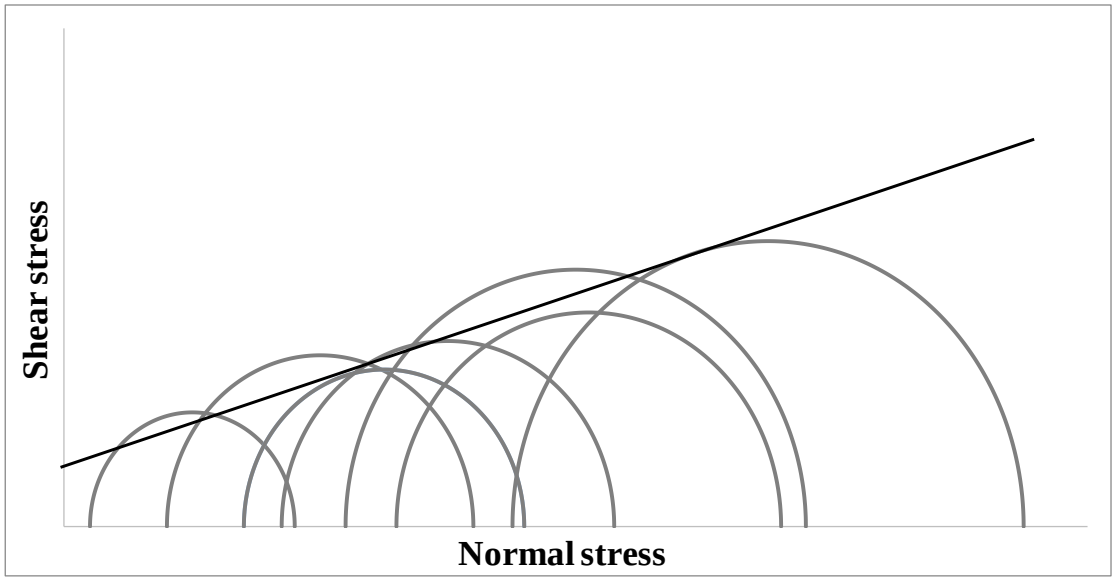

Figure 4. Mohr-Coulomb failure envelope determined from multiple triaxial tests.

3.1 Multistage Triaxial Compression Test

Multistage triaxial compression testing method was firstly proposed by Kovari et al. (1983). The authors indicated that the rock properties under different condition can be obtained from a single specimen, if the test is stopped before the rock specimen fails and is re-performed under different condition.

In order to re-use the formation cores at various conditions, it is necessary to choose an appropriate stopping point where the axial compression stops before the rock loses its intrinsic property. There have been a debate over the stopping point selection methods for the multistage triaxial testing method as shown in Figure 5 (Kovári and Tisa (1975), Kovari et al. (1983), Crawford and Wylie (1987) , Taheri and Tani (2008) , Pagoulatos (2004) and Tran et al. (2010)).

Kovári and Tisa (1975) and Kovari et al. (1983) suggested stopping the axial load when the tangent Young modulus on the stress-strain curves is observed, which is the International Society of Rock Mechanics suggested method. Crawford and Wylie (1987) defined that the stopping point should be when the volumetric strain reaches zero. Taheri and Tani (2008) suggested the stopping point to be when the secant Young modulus becomes constant. Tran et al. (2010) proposed that these methods for determining the stopping point are not suitable. This is because the sample can fail before the constant secant Young modulus and zero volumetric strain are observed and the relationship between non-failure and failure Mohr circles for each loading stage is not well-established.

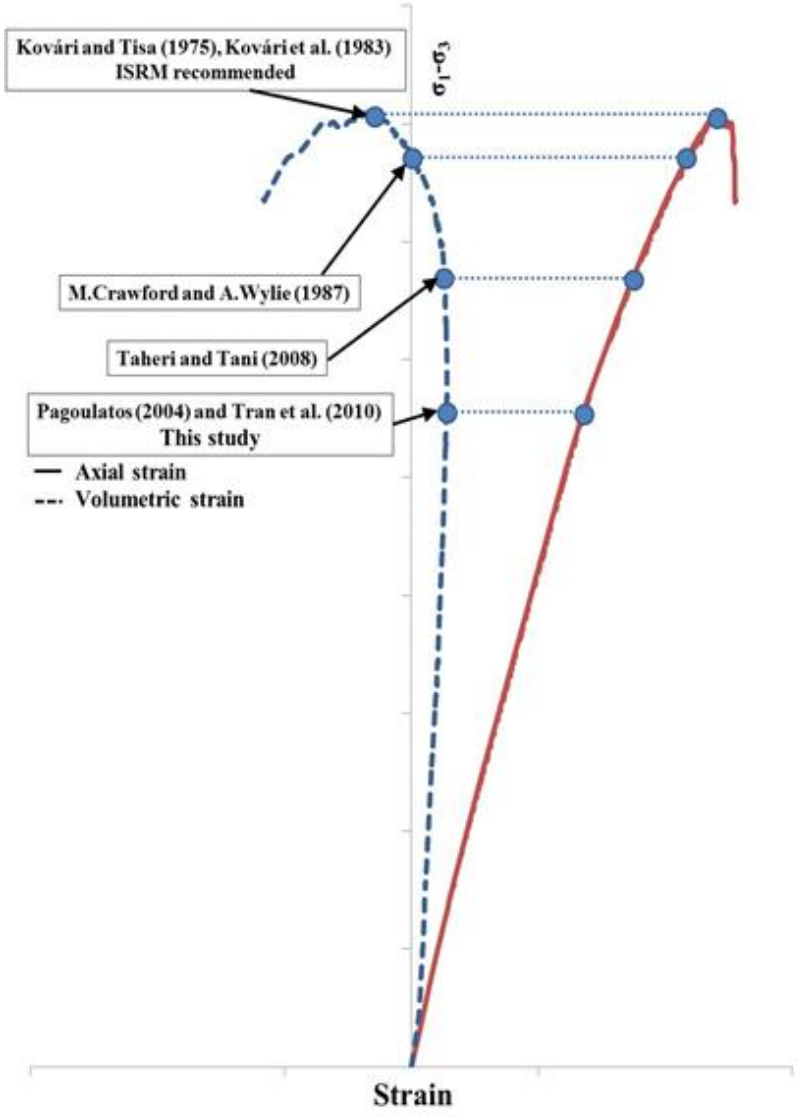

Figure 5. Proposed criteria for stopping points.

On the other hand, Pagoulatos (2004) and Tran et al. (2010) suggested to stop the test at the dilatancy point, when the volumetric strain starts to decrease. According to their analysis, using the dilatancy point as stopping point enables to prevent the irreversible deformation of the specimen. In addition, they pointed out that the analyses over non-failure and failure stages can be established well. However, Taheri and Tani (2008) insist that this method is not suitable for some rock types which do not show dilatancy under high confining pressure.

According to the authors, it is possible to prevent irreversible deformation of the specimen while the interpretation over non-failure and failure stages can be still established reliably. This argument shows the basic dilemma of stopping point selection: one wishes to avoid inducing irreversible deformation in the specimen but without sacrificing collectible information.

In this study, we follow Pagoulatos (2004) and Tran et al. (2010) and select the "dilatancy point" as a stopping point, when the volumetric strain starts to decrease. The practical advantage of this method is that the dilatancy point is easy to observe in the stress-strain curve during the test.

On the other hand, some of the specimens tested showed non-dilatant behavior until failure, which indicates that the volume of the rock specimen keeps decreasing. For this type of rocks, another stopping point criterion needs to be established.

In 3 dimensional cartesian coordinate, each strain of the tested specimen can be expressed as shown in Figure 6. The dashed and solid cylinders represent the rock

specimens before and after deformation. Then the volumetric strain is calculated by the equation given by,

$$\varepsilon_V = \frac{dx}{x} + \frac{dy}{y} + \frac{dz}{z} = \varepsilon_x + \varepsilon_y + \varepsilon_z = \varepsilon_a + 2\varepsilon_l \tag{3.1}$$

where, ε_V is the volumetric strain, ε_a is the axial strain and ε_l is the average lateral strain. Differentiating both hand sides with ε_a, we can get,

$$\frac{d\varepsilon_V}{d\varepsilon_a} = \frac{d\varepsilon_V}{d\sigma}\frac{d\sigma}{d\varepsilon_a} = 1 + 2\frac{d\varepsilon_l}{d\varepsilon_a} = 1 - 2\nu \tag{3.2}$$

where, ν is the Poisson's ratio.

Therefore, the dilatancy point, ($\frac{d\varepsilon_V}{d\sigma} = 0$) is defined when the local Poisson's ratio reaches 0.5.

Figure 7 (a) and (b) show the stress-strain behavior and the local Poisson's ratio of dilatant and non-dilatant rock specimen during the triaxial test, respectively. As it can be seen, the dilatancy point is achieved when the local Poisson's ratio reaches 0.5.

However, the Poisson's ratio of non-dilatant rocks does not increase to reach 0.5 even if the axial strain response indicates the rock starts inelastic behavior. This is because the axial strain is much larger than the lateral strain, implying that the rock deforms more in axial direction than it expands laterally. The phenomenon indicates that the rock deforms by pore collapse. Additional analysis will be provided in section 5.

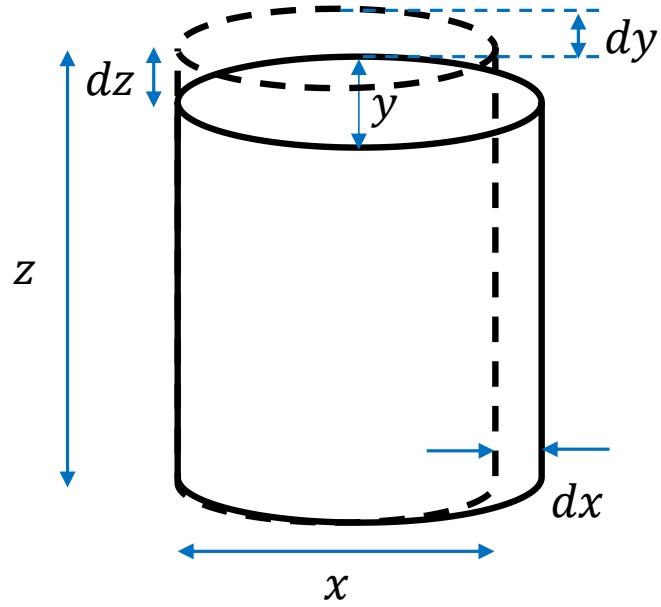

Figure 6. Schematic view of rock deformation
during the test in 3-dimensional cartesian coordinate.

In other words, the dilatancy of the rock specimen during the triaxial test can be distinguished by monitoring the local Poisson's ratio and the stress-axial strain behavior. If the local Poisson's ratio is less than 0.5 and the inelastic behavior on the local Young modulus is detected, we can say that the rock specimen is non-dilatant. Thus, the local Young modulus can be used as a precursor of rock failure for non-dilatant specimens.

In our experiments on non-dilatant specimens, the triaxial test stage was stopped when the local Young modulus decreases 2% from that of the elastic region, which is the minimum value to be clearly detected over the systematic noise. Applying the criterion for stopping point, the multi stage triaxial compression test could be performed on both dilatant and non-dilatant rock specimens.

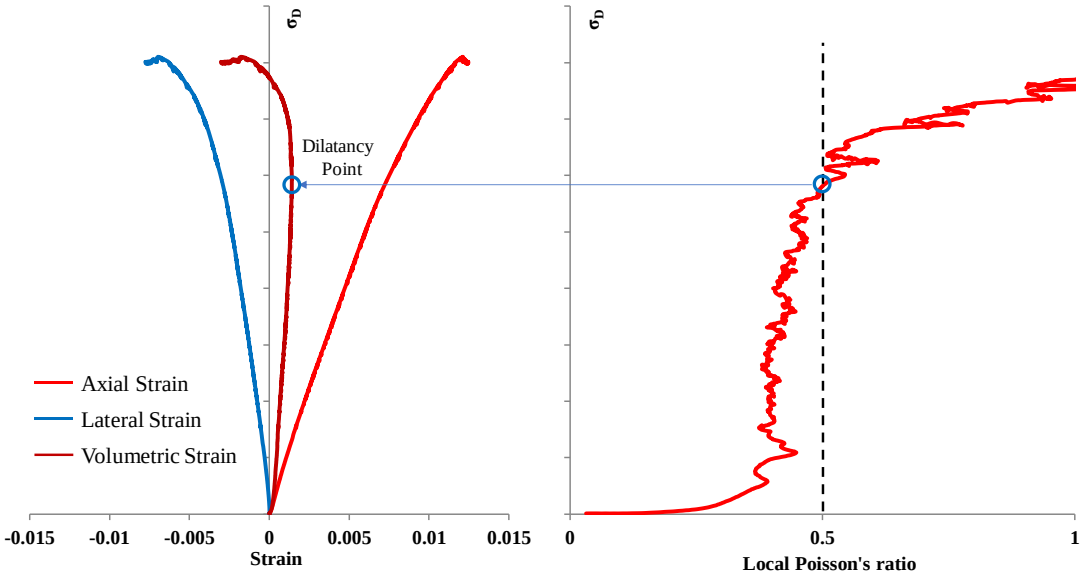

(a)

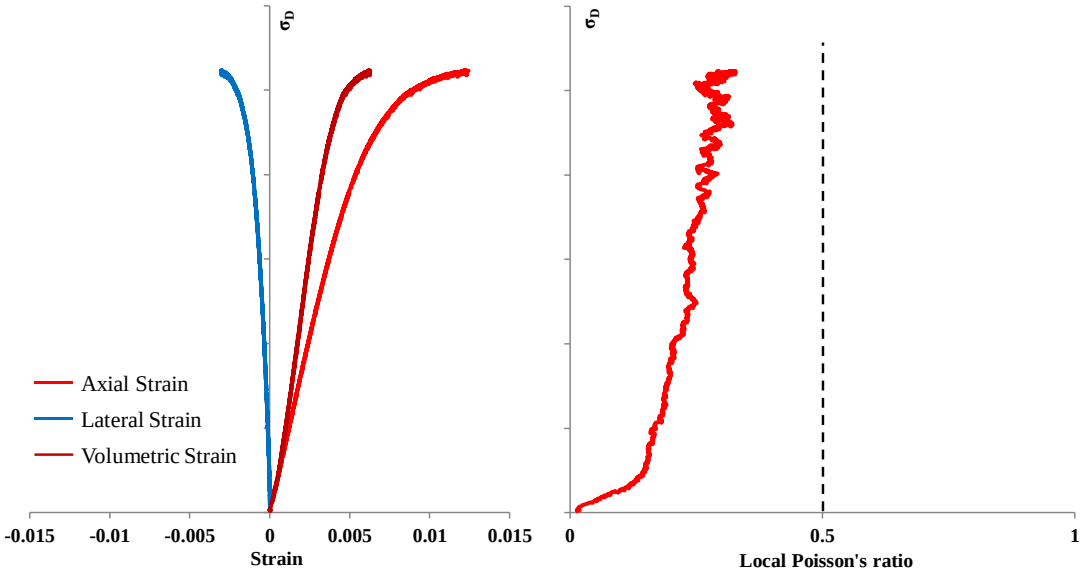

(b)

Figure 7. Identification of dilatancy point by local Poisson's ratio. (a) With dilatancy and (b) non-dilatancy.

Figure 8 and Figure 9 shows the stress-strain responses of 5 stages during multistage triaxial tests on a dilatant and a non-dilatant rock specimen. At each stage, the test is stopped (at red circles), then the confining pressure is increased and a new stage is started to gain the rock properties under different overburden pressure condition. At the last stage, the rock specimen is subjected to failure and the axial strain is further increased until the post-peak response on the stress-strain curve is observed.

3.2 Mohr-Coulomb Failure Criterion

Among the various rock failure criteria, the most commonly used is the Mohr-Coulomb failure criterion due to its mathematical simplicity and straightforward physical meaning of the determined parameters. The failure envelope determined from triaxial tests describes the relationship between shear stress and normal stress along the failure plane (Goodman, 1989). According to Labuz and Zang (2012), the criterion works well with rocks when all principal stresses are compressive.

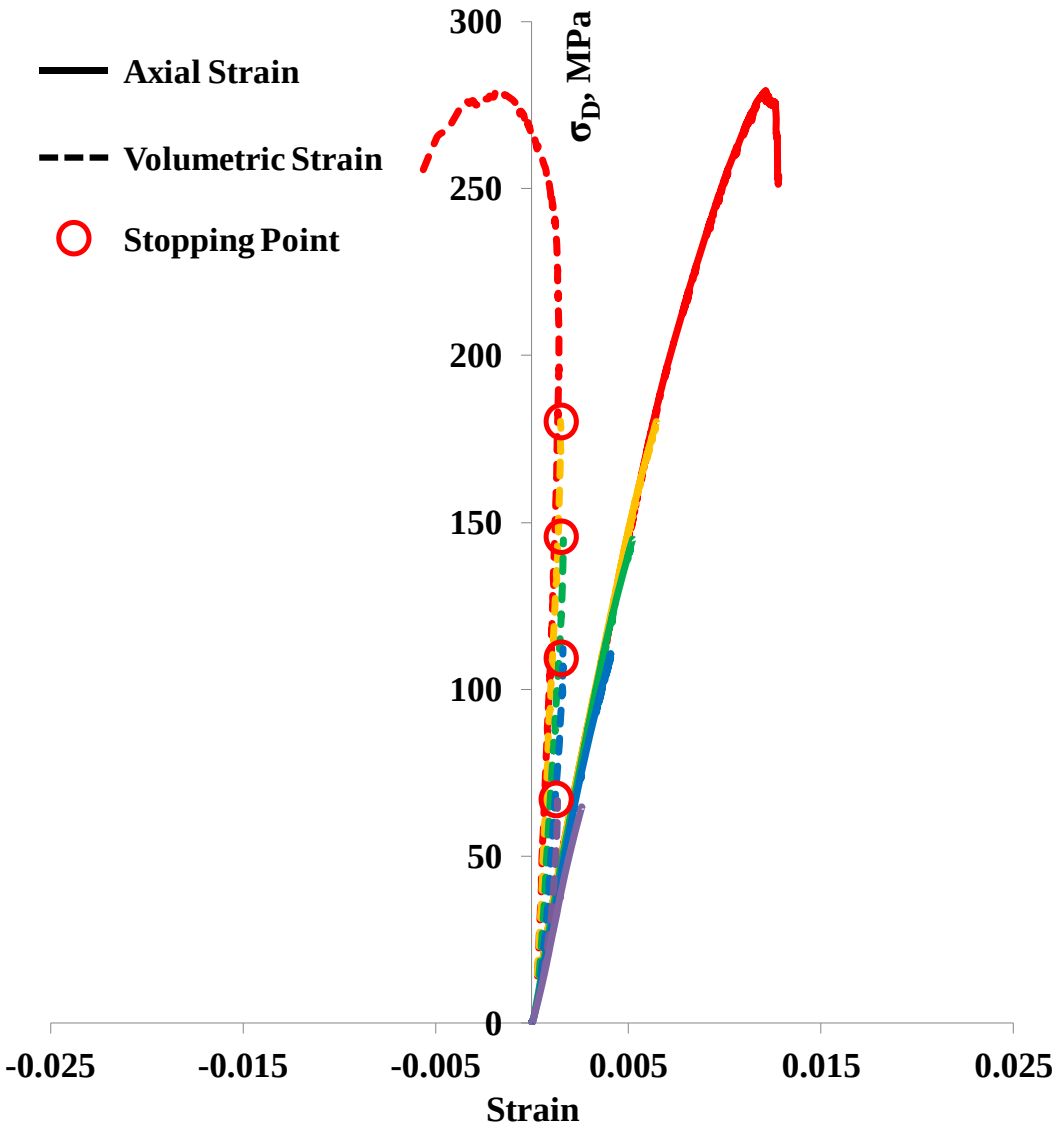

Figure 8. Stress-strain curves for 5-stage multistage triaxial test on dilatant specimen. The red circles indicate the stopping points.

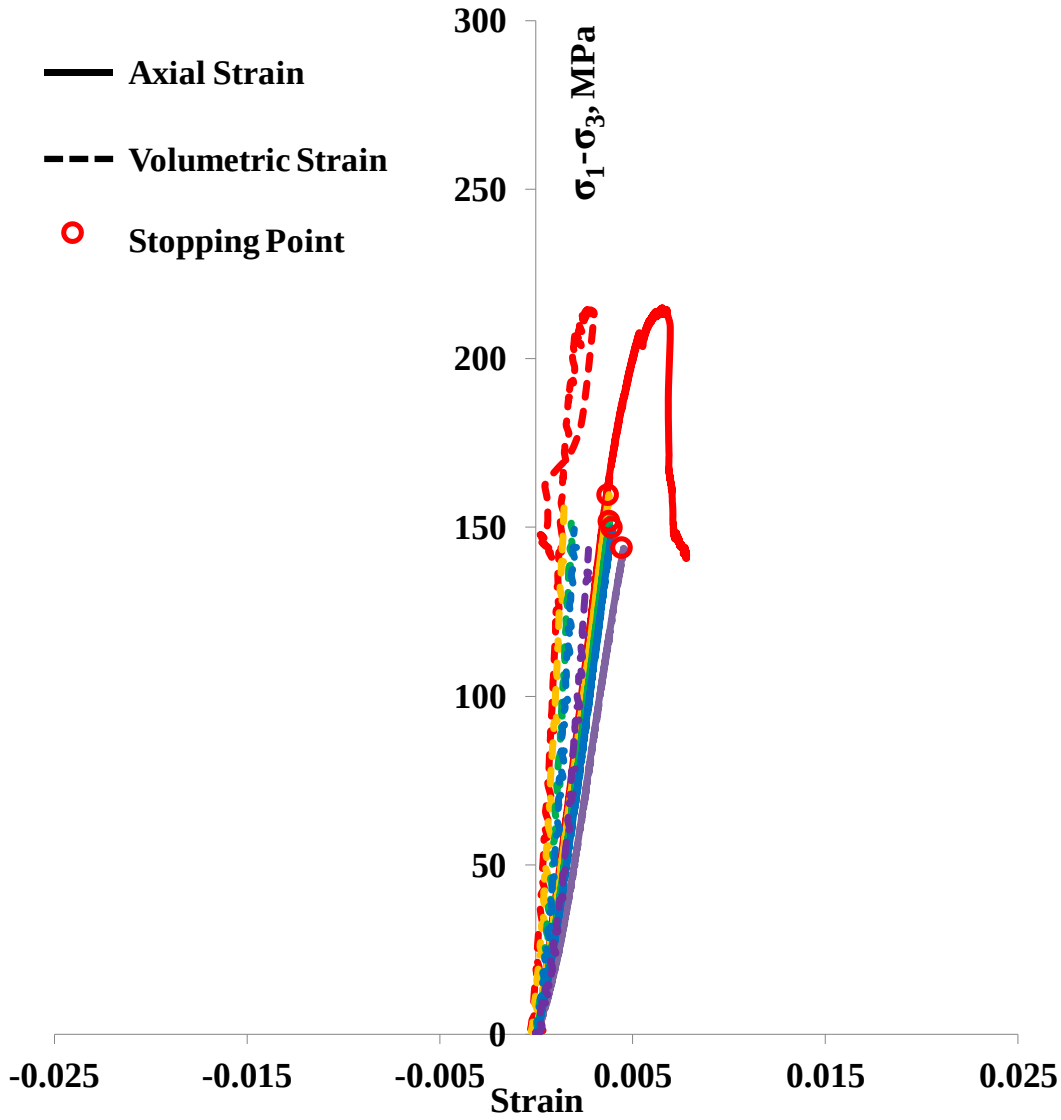

Figure 9. Stress-strain curves for 5-stage multistage triaxial test on non-dilatant specimens. The red circles indicate the stopping points.

Coulomb proposed a relationship

$$\tau = C + \sigma_n \tan \varphi \tag{3.3}$$

where, τ is the shear strength on the failure plane, C is the pure shear strength also known as cohesion, σ_n is the normal stress on the failure plane and φ is the internal friction angle (Figure 10). The relationship between the shear and normal stress can be established by the Mohr's failure criterion given by,

$$\tau_m = \mathrm{f}(\sigma_m) \tag{3.4}$$

where, τ_m is the maximum shear stress given by,

$$\tau_m = \frac{(\sigma_1 - \sigma_3)}{2} \tag{3.5}$$

and σ_m is the mean normal stress given by,

$$\sigma_m = \frac{(\sigma_1 + \sigma_3)}{2} \tag{3.6}$$

where, σ_1 and σ_3 are the maximum and minimum principal stresses, respectively.

Therefore, if a Mohr circle with the radius of τ_m and the center of σ_m are constructed in shear stress-normal stress domain and the circle is tangent to the failure envelope, the rock is at the failure state. In addition, when sets of Mohr circles are drawn, the Coulomb failure envelope can be constructed by fitting a line tangent to the circles. Thus, the Coulomb failure criterion in (3.3) is a linear type of the Mohr failure criterion in (3.4) and the combined criterion is called Mohr-Coulomb failure criterion (Labuz and Zang, 2012).

The failure envelope expressed by equation (3.3) is determined by the rock strengths measured in the laboratory. The Mohr circles are constructed with the measured peak strength values of the rock specimens under specific minimum principal stresses, i.e. confining pressure. Then the failure envelope is determined from the line tangent to the constructed Mohr circles (Figure 10).

In this study, the Mohr-Coulomb failure criterion is applied to determine the rock failure parameters. The failure envelope obtained from multistage triaxial testing results were used to estimate rock strength under different confining pressure condition. How to interpret and to construct the Mohr-Coulomb failure envelope is addressed in detail in the next section.

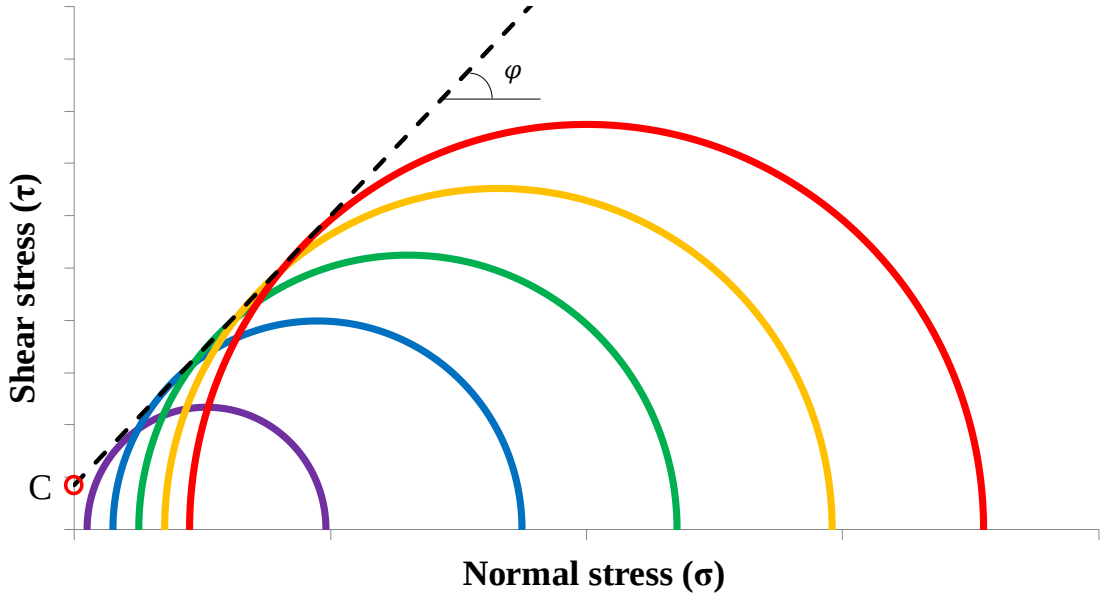

Figure 10. Mohr-Coulomb failure envelope.

3.3 Interpretation of Data Obtained from Multistage Triaxial Test

During a multistage triaxial test, a set of the stress-strain curves is obtained. Except the last stage, the stress-strain behavior is partially available up to the stopping point. From the stress state at the stopping points, where the rock starts the irreversible deformation, the non-failure Mohr circles can be constructed as shown in Figure 11. With the assumption that the best fit tangent line of non-failure Mohr circles has the same slope as the failure envelope, the Mohr-Coulomb failure envelope is established by moving the non-failure line, determined by the non-failure circles, to let the line tangent to the failure circle. The constructed failure envelope then can be used to determine the Mohr-Coulomb parameters, such as internal friction angle and pure shear strength.

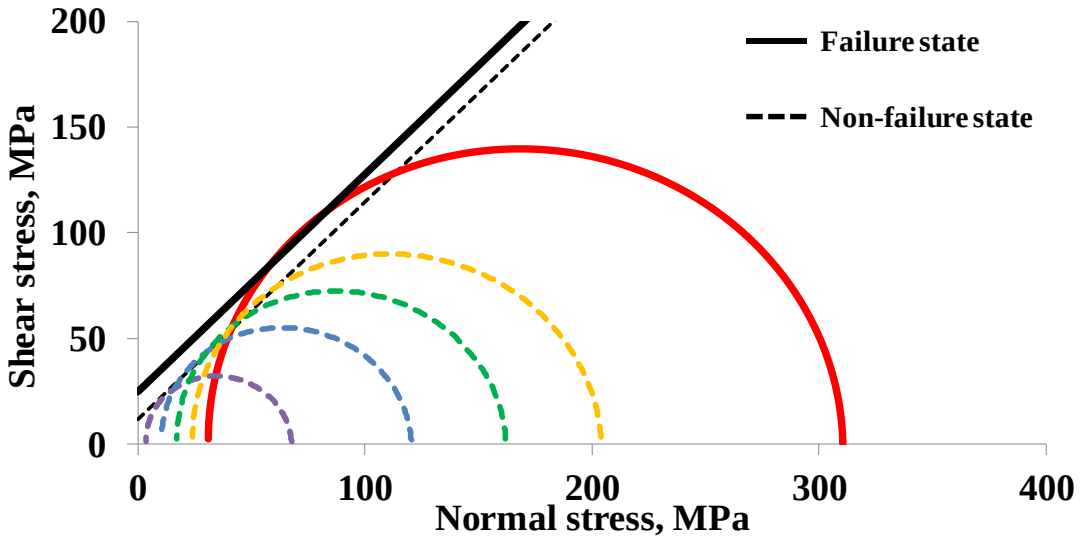

Figure 11. Construction of the rock failure envelope from the multistage triaxial test results. The Mohr circles and failure envelopes determined from the non-failure (dashed) and the failure state(solid).

In addition, the compressive strengths at each confining pressure condition is estimated by constructing the Mohr circles tangent to the failure envelope. In the same manner, the unconfined compressive strength (UCS) can be calculated (Figure 12).

The Young modulus for each stage is determined by the slope of the stress and the axial strain curves. The Young modulus is calculated from the stress-strain curve using the slope of the linear portion of the curves. The average Poisson's ratio is determined by fitting straight lines to the axial and radial strain curves for the same stress range used for the Young modulus. Additional interpretation of the data will be discussed in the section 6.

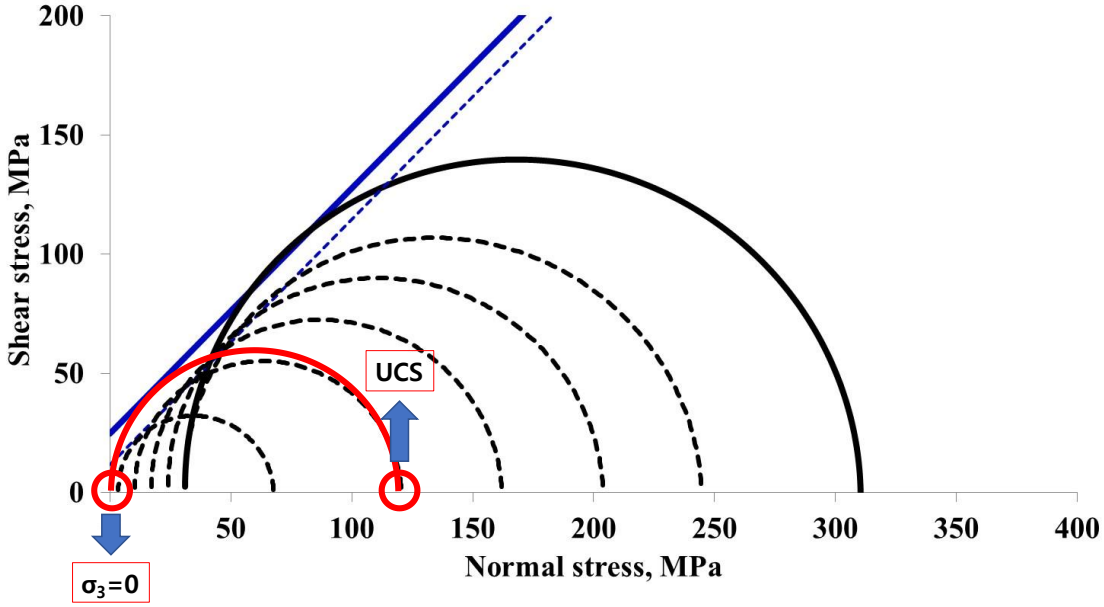

Figure 12. Estimation of unconfined compressive strength.

4. NUMERICAL APPROACH FOR PRESSURE BEHAVIOR DURING PULSE DECAY PERMEABILITY MEASUREMENT

Permeability quantifies how much fluid can flow through a porous medium. Since it is a great interest to estimate the reservoir productivity, the permeability measurement has a significant importance in the field of petroleum engineering.

Core permeability measurement methods can be categorized into 2 groups, steady state and unsteady state methods. Although the steady state measurement method is easy to calculate and is more straightforward, it takes long to reach the steady state during the test, i.e. time independent pressure and flow behaviors. For the low-perm rocks, the time required for the steady state takes much longer, which makes the method inapplicable.

In order to overcome the drawback of the steady state method, numerous researches proposed new approaches in permeability measurement using unsteady state during fluid flow through the rock specimen. One of the most widely used is the pulse decay permeability measurement method proposed by Brace et al. (1968).

In this section, the analytical solution of the pressure behavior during the pulse decay permeability measurement will be reviewed. Applying the finite element method, the test will be computationally simulated to analyze the effect of the heterogeneity in the core specimen.

4.1 Analytical Solution of the Pulse Decay Permeability Measurement Method

The pressure behavior at both edges can be described by analytical solutions (Dacunha, 2014). The 1-D diffusivity equation which governs the fluid flow in the system is written as

$$\frac{\partial^2 \psi}{\partial x^2} = \frac{\phi c_g \mu}{k} \frac{\partial \psi}{\partial t} \tag{4.1}$$

where, ψ is p^2, ϕ is the porosity, c_g is the gas compressibility, μ is the gas viscosity and k is the permeability of the tested specimen.

The boundary conditions are given by

$$\frac{\partial \psi}{\partial x} - \frac{\mu c_g V_u}{Ak} \frac{\partial \psi}{\partial x} = 0 \quad \text{for } x = L \tag{4.2}$$

$$\frac{\partial \psi}{\partial x} - \frac{\mu c_g V_d}{Ak} \frac{\partial \psi}{\partial x} = 0 \quad \text{for } x = 0 \tag{4.3}$$

where, L is the length, A is the cross-section area of the specimen, V_u and V_d are upstream and downstream volumes.

The initial conditions are given by

$$\psi(x, 0) = p_{pulse} \quad \text{for x} > \text{L} \tag{4.4}$$

$$\psi(x,0) = 0 \qquad \text{for } 0 \le x \le L \tag{4.5}$$

where, p_{pulse} is the pulse pressure initially located at the upstream vessel. Solving the equations above, the analytical solutions can be expressed as,

$$p(x_D, t_D) = p_{pulse} \cdot \sqrt{\frac{1}{1+\beta+\gamma} + 2\sum_{n=1}^{\infty} \frac{e^{-\alpha_n{}^2 t_D}(\cos(\alpha_n x_D) - \frac{\alpha_n \gamma}{\beta}\sin(\alpha_n x_D))}{(1+\gamma+\beta-\frac{\alpha_n{}^2\gamma}{\beta})\cos(\alpha_n) - \alpha_n(1+\gamma+2\gamma/\beta)\sin(\alpha_n)}} \tag{4.6}$$

where, α_n is the nth root of

$$\alpha_n\beta(\gamma+1)\cos(\alpha_n) + (\beta^2 - \alpha_n{}^2\gamma)\sin(\alpha_n) = 0 \tag{4.7}$$

where,

$$\beta = \frac{\phi V_s}{V_u} \tag{4.8}$$

$$\gamma = \frac{V_d}{V_u} \tag{4.9}$$

And the dimensionless variables are given by,

$$x_D = \frac{x}{L} \tag{4.10}$$

$$t_D = \frac{\mathrm{kt}}{\phi \mu c_g L^2} \tag{4.11}$$

Using the analytical solution, the pressure behavior at both edges of the rock specimen can be calculated as in Figure 13. In order for simplification, the dimensionless pressure is adopted to normalize the pressure.

$$p_D = \frac{p}{p_{pulse}} \tag{4.12}$$

As the results show, the pressure is stabilized at earlier time when the permeability of the specimen is higher.

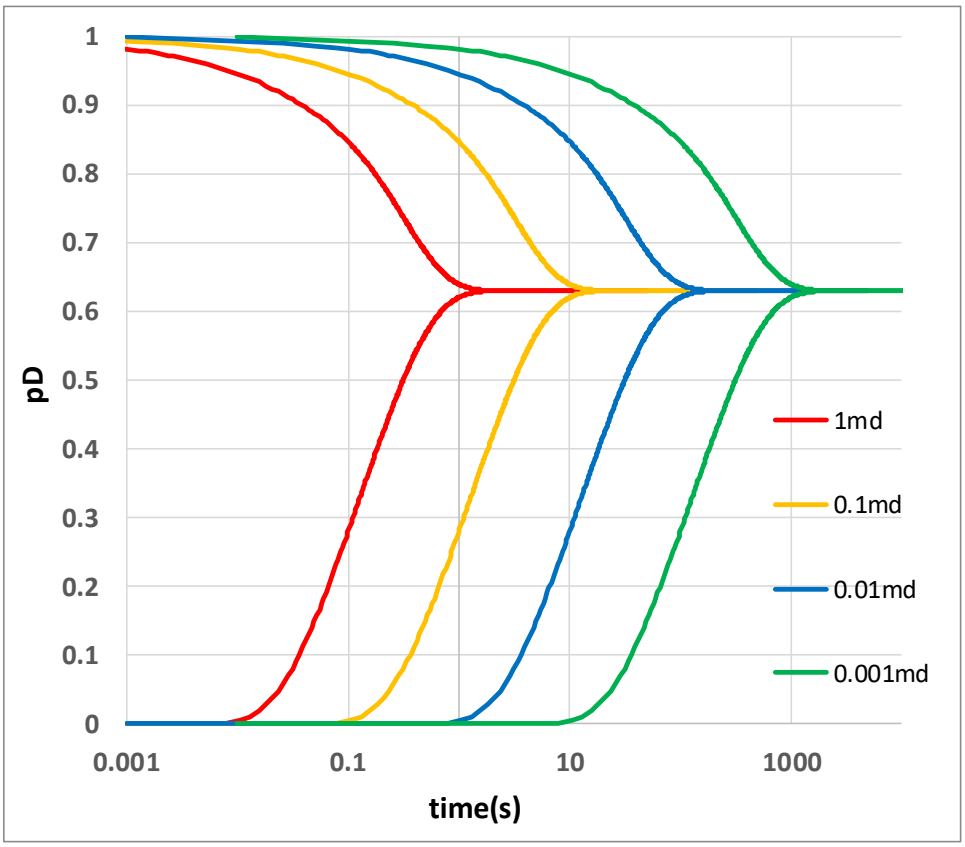

Figure 13. Analytical solution of pulse decay permeability measurement method. Pressure behavior at both edges of the specimen during the test.

4.2 Numerical Approach for Pulse Decay Permeability Measurement

The analytical approach of the pulse decay method proposed by Brace et al. (1968) is based on the assumption that the core specimen is homogeneous and isotropy. For low permeability rocks from unconventional reservoirs, however, the effect of heterogeneity needs to be accounted to avoid any misleading results. The heterogeneity effect was reviewed by Kamath et al. (1992), who focused on the effect of a high conductive fracture in the low permeability rock during the pulse decay measurement. The authors found that the transverse heterogeneity can be detected on the early time pressure behavior.

In this section, the rock specimen and the testing system were modelled in 2-dimension (2D) using finite element method (FEM) to investigate the heterogeneity effect on the pressure behavior during the test.

4.2.1 Finite Element Model Construction

The pulse decay permeability is simulated in 2D FEM using Mathematica software. The governing equation is given by,

$$\nabla^2\psi = \frac{\phi c_g \mu}{k}\frac{\partial \psi}{\partial t} \tag{4.13}$$

The boundary conditions are given by,

$$\frac{\partial \psi}{\partial x} = 0 \quad for\ x = 0\ and\ D \tag{4.14}$$

$$\frac{\partial \psi}{\partial y} = 0 \quad for\ y = 0\ and\ y = L + L_d + L_u \tag{4.15}$$

where, D is the specimen diameter, L is the specimen length, L_d is the length of downstream and L_u is the length of upstream.

The initial conditions are given by,

$$\psi(x, y, 0) = {p_{pul}}^2 \ \ for\ y > L + L_d \tag{4.16}$$

$$\psi(x, y, 0) = 0 \quad for\ y \leq L + L_d \tag{4.17}$$

The permeability of the upstream and downstream volumes is set as 10 Darcy, in order to mimic the high-conductive flow behavior. The cross-sectional areas and porosity of the upstream and downstream volumes are assumed same as the rock specimen. Then the lengths of both volumes can be calculated by

$$L_u = \frac{V_u}{\phi\, A} \tag{4.18}$$

$$L_d = \frac{V_d}{\phi\, A} \tag{4.19}$$

The system was modelled in 2D with 324 rectangular elements as shown in Figure 14.

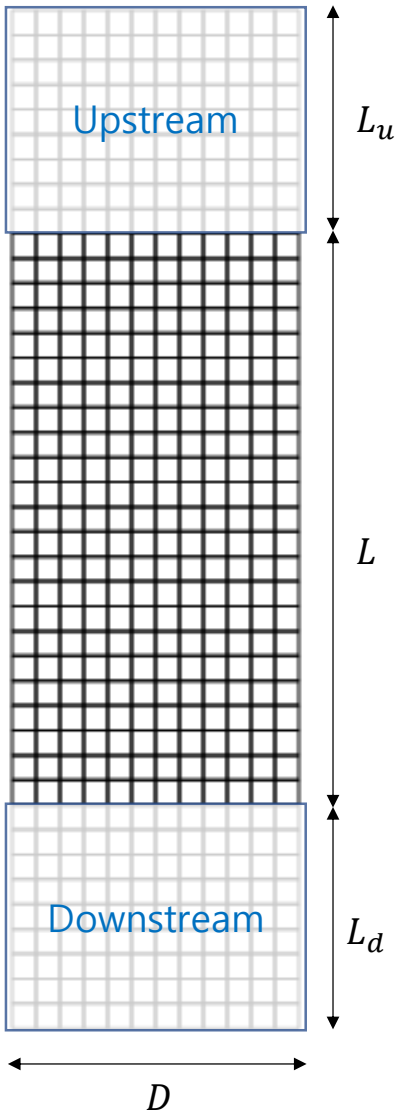

Figure 14. 2D element mesh.

4.2.2 Verification of the Constructed Model with Analytical Solution

In order to verify the constructed model, the results were compared with the analytical solution. Assuming identical testing system and condition, the pressure behaviors of the rock specimen with different permeability values during the test were calculated using both numerical and analytical approaches. The input data is shown in Table 1.

According to the calculated pressure behavior in Figure 15, it appears that the results from both methods are identical which implies that the 2-dimensional FEM model can appropriately represent the pressure behavior.

Table 1. Input parameters for the 2D FEM model verification.

Specimen diameter (m)	0.0254
Specimen length (m)	0.0508
Porosity (fraction)	10%
Upstream volume (m^3)	5×10^{-6}
Downstream volume (m^3)	5×10^{-6}
Gas viscosity (kPa·s)	10^{-8}
Gas compressibility (kPa^{-1})	10^{-3}

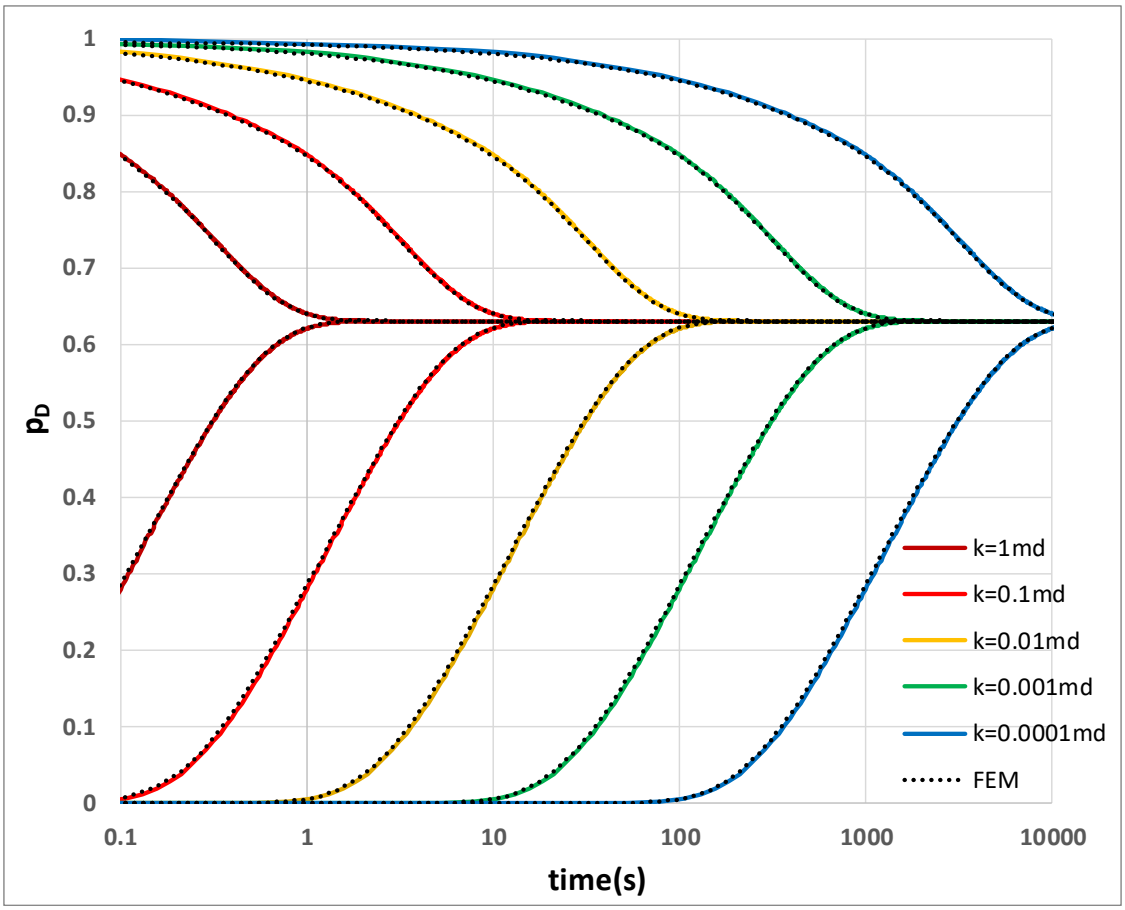

Figure 15. Pressure behaviors calculated by analytical (colored solid) and numerical methods (black dots).

4.2.3 Heterogeneity Effect on Pressure Behavior during Pulse Decay Permeability Measurement Test

According to Kamath et al. (1992) and Ning et al. (1993), the transverse heterogeneity of the rock specimen affects the pressure behavior during the pulse decay permeability measurement. Since the analytical solution assumes that the specimen is homogeneous, the heterogeneity might yield misinterpretation of the measured data.

In this section, both transverse and longitudinal heterogeneity effects will be analyzed by the 2D FEM model. Assuming various structure of heterogeneity, the pressure behavior during the pulse decay permeability measurement will be simulated.

For the transversely heterogeneous specimen, it was assumed that the low permeability specimen contains a high permeability region with the width of 0.001m at the center which vertically cuts through the specimen (Figure 16 (a)). On the other hand, to model rock specimen with longitudinal heterogeneity, 2 lateral layers were considered, one with high and one with low permeability. Consequently, there are 2 cases for the longitudinal heterogeneity, the one with high permeability at the upper side of the specimen and the other with higher permeability at the lower side of the specimen (Figure 16 (b) and (c)). The computational analysis was performed with the input data shown in Table 1.

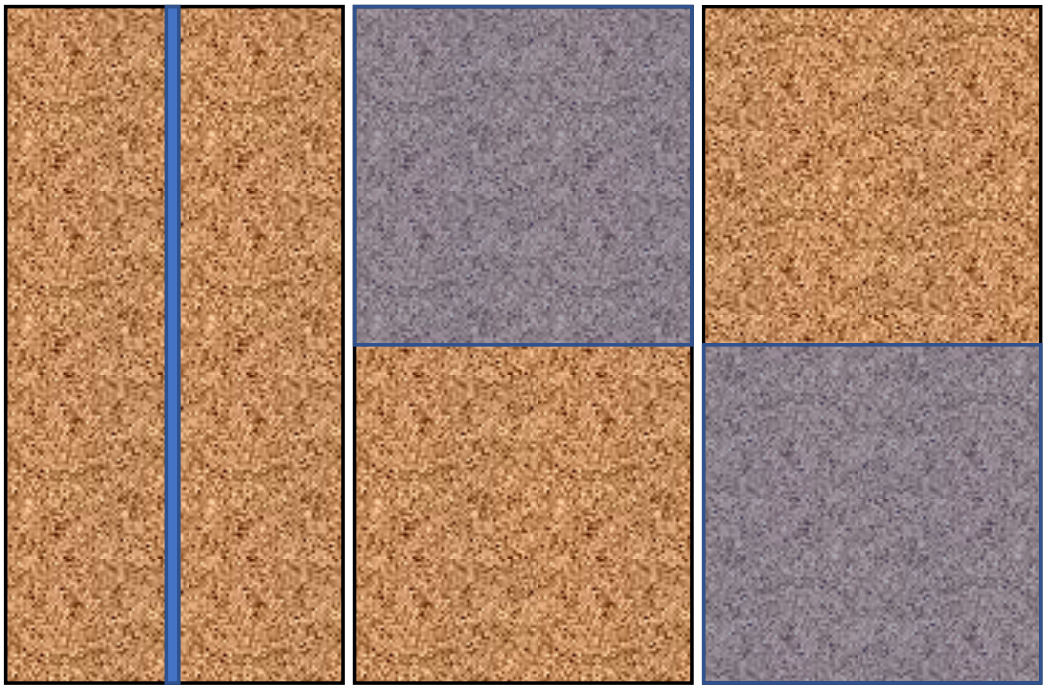

(a) (b) (c)

Figure 16. Rock specimens with (a) transverse and (b) longitudinal heterogeneity. Blue color areas stand for higher permeability regions.

The permeability values of the high and low permeability regions are described in Table 2. For the transverse heterogeneity, the lower permeability (k_L) was fixed at 0.00001md, while the higher permeability was increased from 0.00001 to 1md. Therefore, when the higher permeability is 0.00001md, the specimen is homogeneous. On the other hand, the higher permeability in the longitudinally heterogeneous specimen was fixed at 1md and the lower permeability is increased from 0.00001 to 1md. The specimen is homogeneous when the lower permeability is 1md.

In order to analyze the distinctive pressure behavior of the heterogeneous specimen, the results will be compared with the pressure behaviors of the homogeneous specimens having the same equivalent permeability. Table 2 shows the calculated equivalent permeability at the very right column of each case.

Figure 17 shows the pressure behaviors of the transversely heterogeneous specimen (solid curves) and of the homogeneous specimen with the same equivalent permeability (dashed curves). When the permeability difference is less than 10 times ($k_H \leq 0.01\text{md}$), the heterogeneity does not yield any significant difference compared to the homogeneous rock. However, the discrepancy at the downstream pressure is observed when the difference in permeability is lower than 100 times ($k_H \geq 0.001\text{md}$). When the higher permeability region has the permeability of 0.1md, the pressure equilibrium between the upstream and downstream occurs before the final stabilization is achieved. This is the distinctive pressure behavior from the transverse heterogeneity emphasized by Kamath et al. (1992) and Ning et al. (1993).

Table 2. Permeability values for heterogeneity effect analysis.

Transverse Heterogeneity (md)			Longitudinal Heterogeneity (md)		
k_L	k_H	k_e	k_L	k_H	k_e
0.00001	0.00001	0.000010	0.00001	1	0.000020
	0.0001	0.000015	0.0001		0.000200
	0.001	0.000060	0.001		0.001990
	0.01	0.000511	0.01		0.019800
	0.1	0.005022	0.1		0.181810
	1	0.050137	1		1

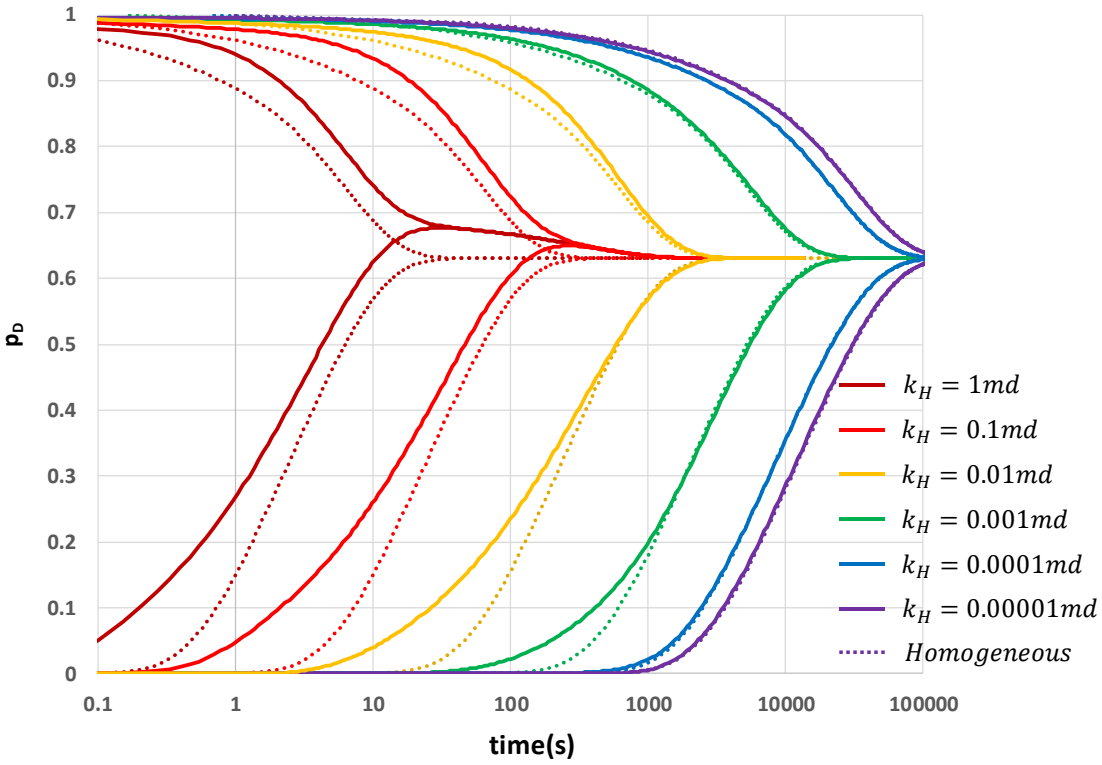

Figure 17. Pressure behaviors during the tests on the specimen with transverse heterogeneity (solid) and the homogeneous specimen with same equivalent permeability (dotted).

Figure 18 (a) shows the pressure distribution of the rock specimen with higher permeability region with 0.1md. Since the permeability heterogeneity is significant, the pressure equilibrium between the upstream and downstream vessels is achieved earlier than the final stabilization of the specimen. It can be seen that there is still a residual portion of the specimen remaining unstabilized at 500 seconds. On the other hand, when the permeability difference is small, the stabilization occurs at both high and low permeability regions (Figure 18 (b)).

Comparing the pressure behaviors with the homogeneous specimens having same equivalent permeability, the following important feature was observed. The time when the pressure difference between the upstream and downstream disappears is identical even if the specimen contains transverse heterogeneity. In other words, the pressure equilibrium time is uniquely determined by the equivalent permeability during the pulse decay permeability measurement. We name the equilibrium time as “characteristic time”. The characteristic time is inversely proportional to the equivalent permeability of the rock. We will see that this statement is valid for quite general conditions.

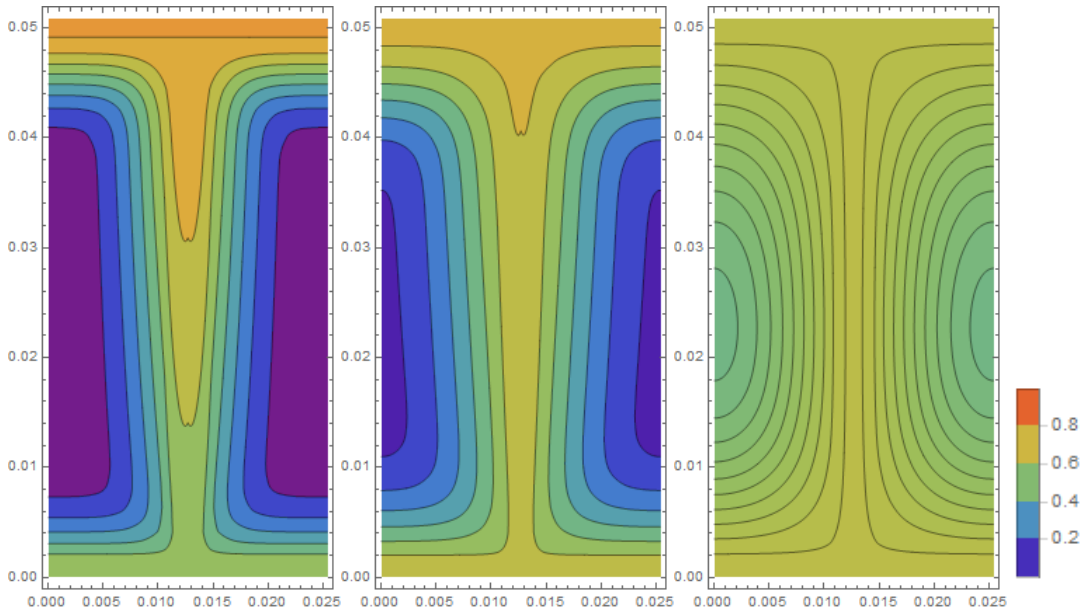

(a)

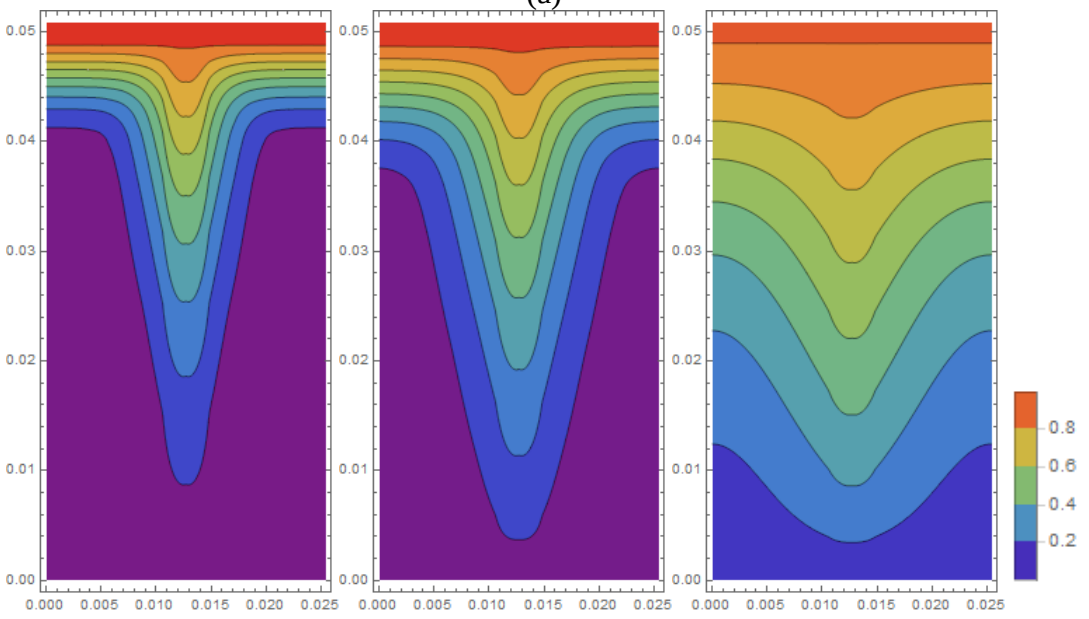

(b)

Figure 18. FEM calculated pressure distribution in rock specimen, 50, 100 and 500 second after test begins (from left). Lower permeability is 0.00001md and higher permeability is (a) 0.1md and (b) 0.001md. Axes units are in *mm*. Colors represent p_D values.

In order to analyze the longitudinal heterogeneity effect, it is assumed that the rock specimen consists of 2 lateral layers, as shown in Figure 16 (b) and (c). Figure 19 shows the pressure behavior during the pulse decay permeability measurement on the rock specimen with the high permeability upper layer. The upstream pressure decreases with the same rate at the early time, while the downstream pressure shows small discrepancy comparing to the results from the homogeneous specimens.

Figure 20 shows the pressure distribution in the homogeneous specimen with 1md and the heterogeneous specimen with 1md upper layer and 0.001md lower layer (Figure 20 (a) and (b), respectively). The pressure distributions in the both specimens are almost same at 0.1 second after the test begins. In both cases, the pressure pulse at the upstream flows through the 1md area of the rock. Therefore, the upstream pressure behaviors are identical until the pulse reaches the lower layer. Consequently, the upstream pressure behavior at early time depends on the permeability of the upper portion of the specimen.

However, if the lower portion of the specimen has higher permeability, there is not any significant discrepancy (Figure 21).

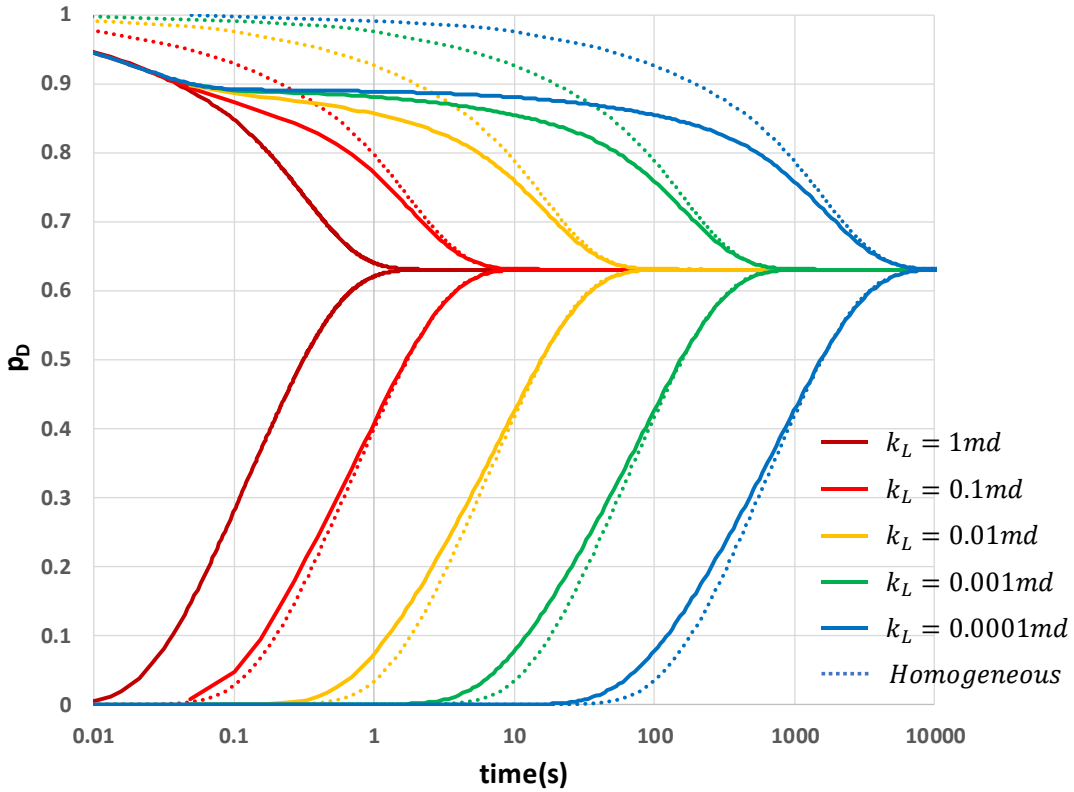

Figure 19. Pressure behaviors during the tests on the specimen with longitudinal heterogeneity (solid) and the homogeneous specimen with same equivalent permeability (dotted). The high permeability layer of 1md is located at the upper part of the specimen.

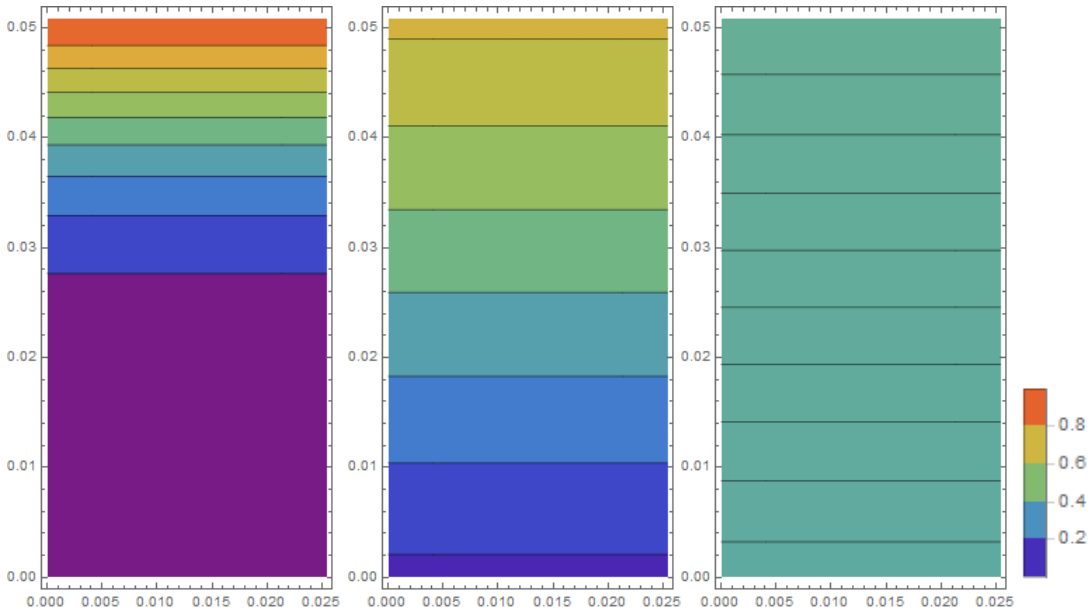

(a)

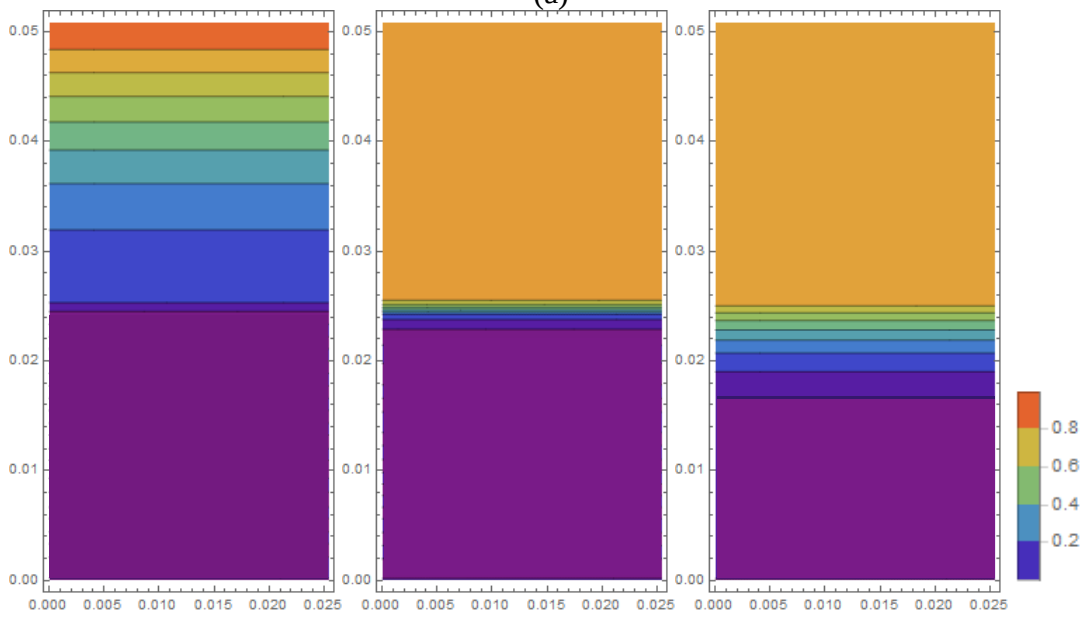

(b)

Figure 20. FEM calculated pressure distribution at 0.1, 1 and 10 seconds after the test begins (from left). (a) Homogeneous specimen with 1md permeability and (b) heterogeneous specimen with 1md permeability at the upper layer and 0.001md permeability at the lower layer. Axes units are in *mm*. Colors represent p_D values.

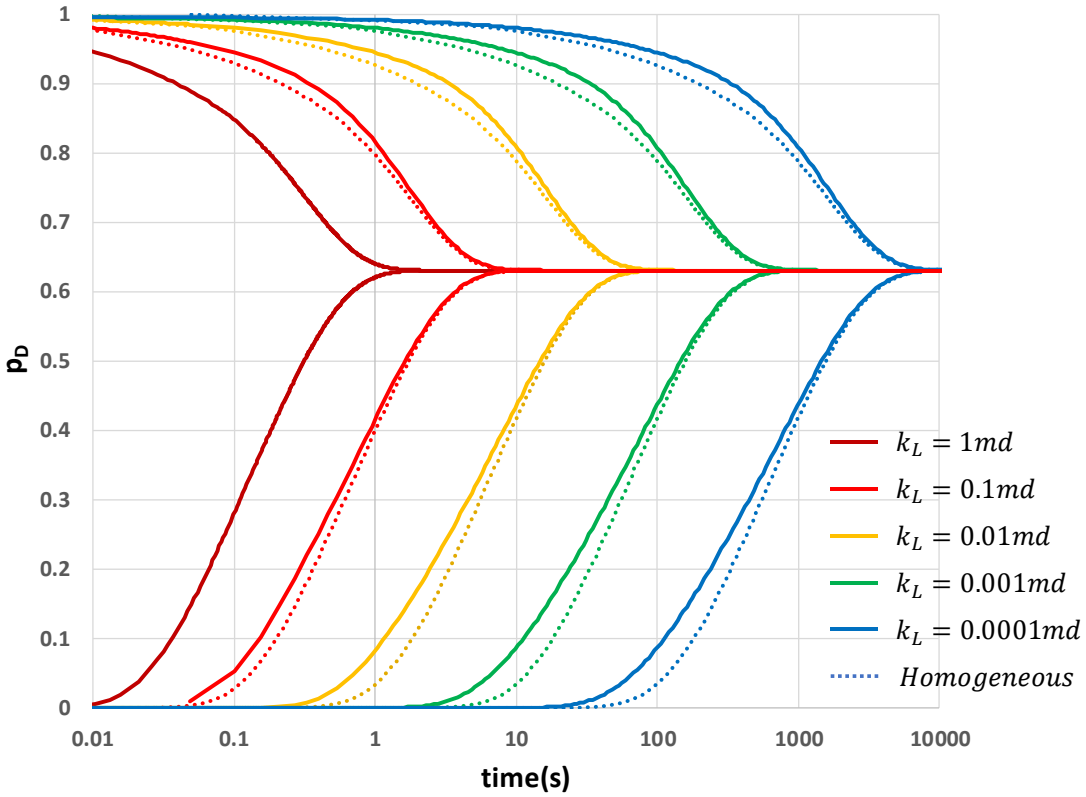

Figure 21. Pressure behaviors during the tests on the specimen with longitudinal heterogeneity (solid) and the homogeneous specimen with same equivalent permeability (dotted). The higher permeability layer of 1md is located at the lower part of the specimen.

It was found that the equivalent permeability of the longitudinally heterogeneous specimen uniquely determines the characteristic time. As a result, the characteristic time can be reliably used to determine the permeability of the rock specimen even if there is significant heterogeneity effect. We will show a practical application of the characteristic time in section 8.2.

4.3 Summary

In this section, the pulse decay permeability measurement was simulated to analyze the heterogeneity effect on the pressure behavior. First the 2D FEM model built in Mathematica was validated using the analytical solution available for the homogenous case.

In order to analyze the heterogeneity effect, cases with transverse and longitudinal heterogeneity were investigated by comparing them to the homogeneous specimen with the same equivalent permeability. For the transverse heterogeneity, some discrepancy is clearly seen in the early time. The longitudinal heterogeneity induces a distinctive pressure behavior in the early time if the upper part of the rock specimen is the one with higher permeability.

The important feature achieved from this section is that the characteristic time depends only on the equivalent permeability irrespective to the actual structure of the heterogeneity. Therefore, we will use the characteristic time as a reliable indicator of the permeability of the rock specimen.

5. ROCK MECHANICAL PROPERTY MEASUREMENT BY TRIAXIAL COMPRESSION TESTS*

Triaxial compressive testing is widely used method to measure the rock properties in laboratories. A cylindrical rock specimen is axially compressed with a specific confining pressure as the stress-strain response is simultaneously measured. If the test focuses on parameters describing the rock behavior under different confining pressure conditions, it needs to be conducted on multiple specimens. Although the specimens are obtained from the same interval of the target formation, heterogeneity over the specimens would still exist.

Since one of our primary goals is to obtain the permeability of intact and failed rock specimen, the non-uniform distribution of natural fractures would have considerable influence. Therefore, the multistage triaxial testing method was adopted to determine the rock properties on each specimen in order to avoid any misleading outcome from the heterogeneity over the specimens. During the test, careful stopping criterion was used to prevent irreversible deformation (except for the last stage).

* Reprinted with permission from "Laboratory scale characterization of brittleness and permeability enhancement due to rock failure." by Jihoon Wang, Peter Valko and Ahmad Ghassemi, accepted for publication in forthcoming issue of *International Journal of Oil, Gas and Coal Technology*.

5.1 Experimental Procedure

The tests were performed using TerraTek Model FX-S-33090 triaxial load frame. The schematic diagram of the testing system is shown in Figure 22. Prior to the test, the specimen was fully saturated with water, using a vacuum pump for 24 hours. The specimen was jacketed with a teflon tube to isolate the specimen from the confining oil. Then, the axial and lateral strain gauges are installed on the core specimen and connected to the data acquisition system. After the installment process is finished, the hydraulic cell is filled with the confining oil. The desired confining pressure in the cell is achieved by the control system.

The axial stress is applied in strain controlled mode at a rate of 7×10^{-6} strain/second. During the first 4 stages, axial loading is stopped and released at the stopping point, as discussed in section 3.1. At the last stage, the rock is loaded to failure, and hence we are able to determine its compressive strength. Afterwards, the axial compression is continued to detect the post-peak behavior.

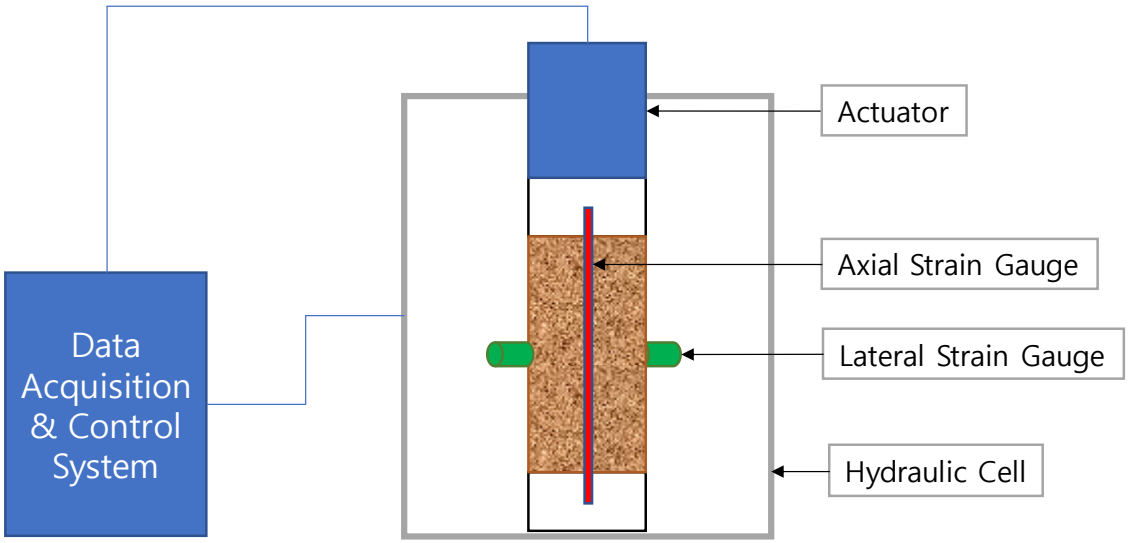

Figure 22. Schematic diagram of the triaxial testing system.

5.2 Core Specimen Description

From a lithological point of view, the rock specimens used in this study are categorized as Newberry tuffs, Mancos shales and Middle East carbonates.

The Newberry tuff specimens were obtained from 3 wells located on the western flank of Newberry volcano, Geo N-1, Geo N-2 and Oxy. The 5.08 by 30.48 cm (2 by 12 inches) drill cores were extracted from 5 different intervals of the wells. Geo N-1 samples were from 1,223.2-1,223.6 m (4,013-4,014.5 feet) and 1,325.3-1,325.7 m (4,348–4,349.5 feet), GEO N-2 samples were from 1,286.1-1,286.6 m (4,219.5–4,221 feet), and 1,304.8-1,305.3 m (4,281–4,282.5 feet), and Oxy samples were from 1,339.4-1,339.9 m (4,394.5–4,396 feet).

The whole cores were smoothened and treated to obtain 2.54 by 5.08 cm (1 by 2 inch) core specimens for the triaxial compressive tests. All tuff specimens are marked with “V” and “H” denoting the direction, vertical and horizontal to the bedding plane. The locations and directions of the rock specimens extracted from the drill cores are shown in Figure 23.

Mancos shale is one of the emerging unconventional reservoirs which was studied as a major source rock of the Uinta-Piceance Province (Kirschbaum, 2003). Two Mancos shale specimens were tested in this study (Figure 24). In addition, two carbonate specimens from Middle East were tested (Figure 24). Additional information including coring direction, depth recovered, etc. are unavailable.

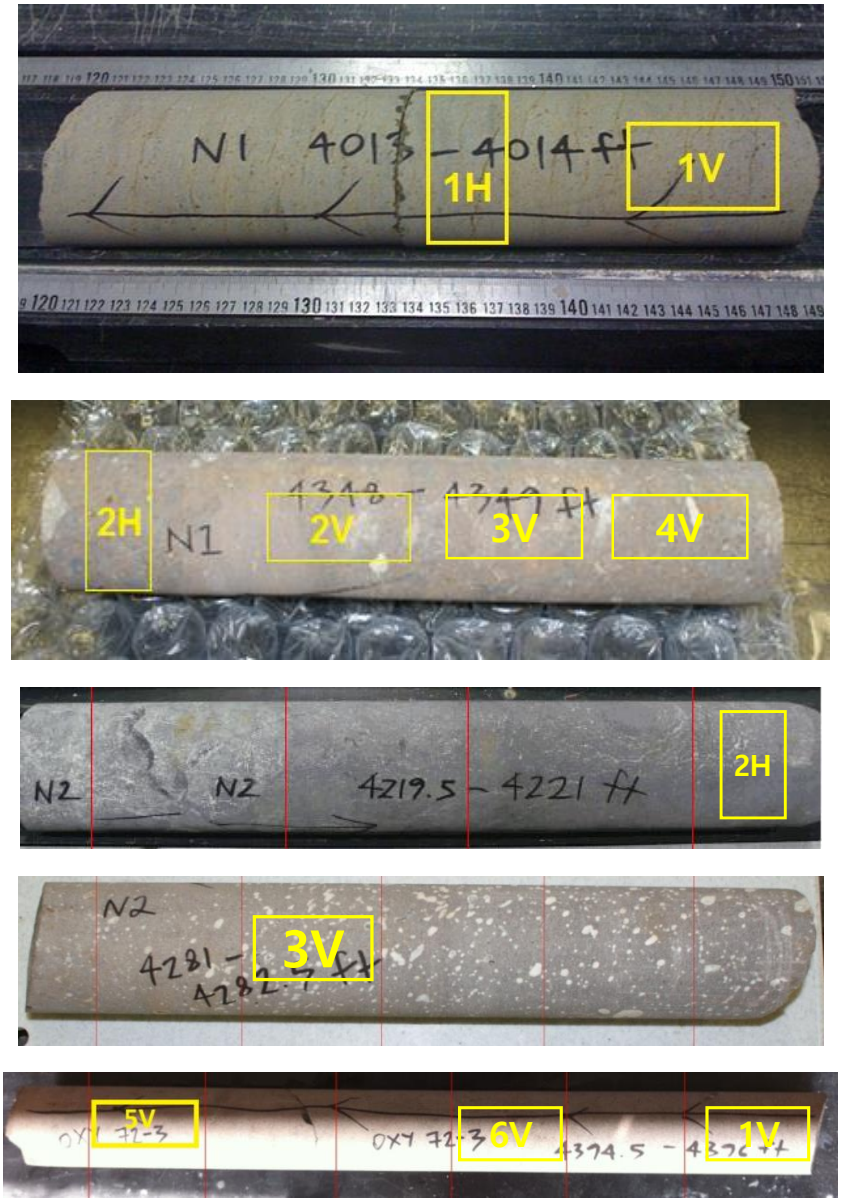

Figure 23. Obtained drill cores from Geo N-1, N-2 and Oxy wells.

Figure 24. Mancos shale (left) and Middle East (right) carbonate specimens.

5.3 Natural Fracture Identification by X-ray Computerized Tomography

Prior to triaxial testing, each plug was scanned by the X-ray computerized tomography (CT) to detect natural fractures and vesicles. The CT scan process was conducted in the Department of Petroleum Engineering in Texas A&M university and Texas A&M university at Qatar. Each core plug was scanned in 10 to 12 slices with the thickness of 0.1 inch and the overall 3D images were constructed.

The 3D CT image of N1-4013-1H detected a vertical natural fracture at the center of the specimen (Figure 25 (a)). The image of N1-4013-1V shows the specimen contains a lateral natural fracture which does not cut through the specimen (Figure 25 (b)). The fractures in both specimens were completely healed and filled with secondary minerals (Wang et al., 2016).

(a)

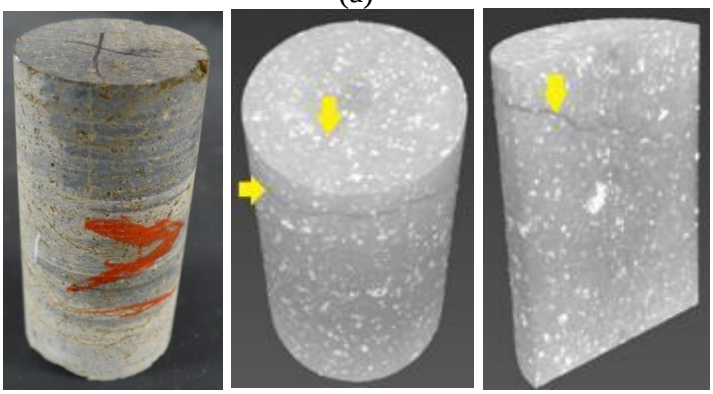

(b)

Figure 25. Pictures and 3D CT images of (a) specimens N1-4013-1H and (b) 1V before compressive tests. The yellow arrows indicate natural fractures.

As shown in Figure 26 (a), the N2-4219.5-2H contains a recognizable natural fracture, which is completely filled with secondary minerals. Many tiny vesicles were observed on the surface of specimen N2-4281-3V, most probably produced by vapor bubbles emerging from fluid inclusions. From the CT image, sparsely distributed macro pores were detected (Figure 26 (b)).

Three specimens from the Oxy-4394.5 drill core were examined. It was found that the rock is dense with very little visible porosity. Figure 27 shows that the specimen 5V

contains a natural fracture which is healed and filled with secondary minerals (Wang et al., 2016).

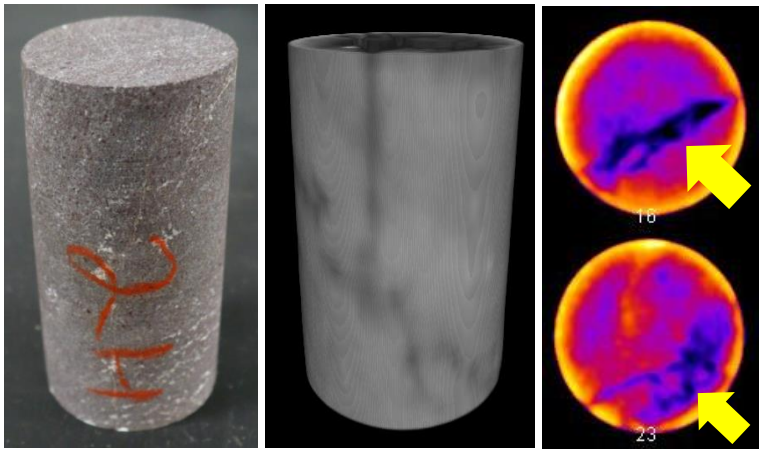

(a)

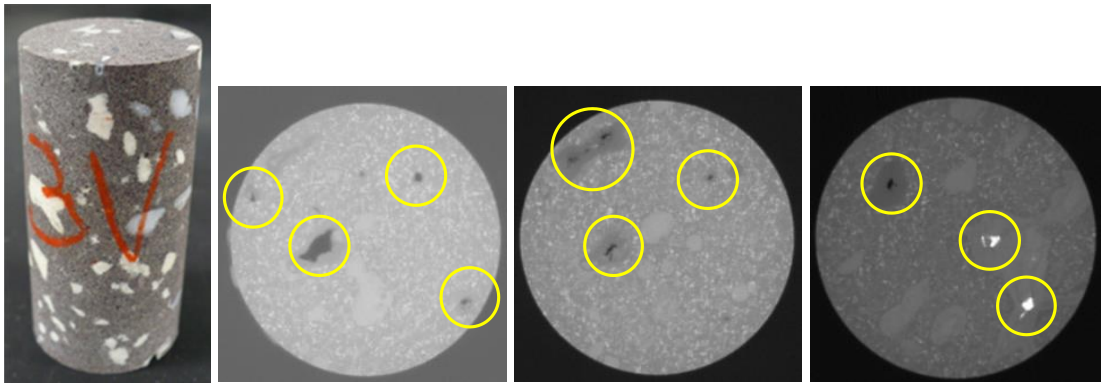

(b)

Figure 26. Pictures and 3D CT images of (a) specimens N2-4219.5-2H and (b) N2-4281-3V before compressive tests. The yellow arrows and circles indicate natural fractures and macro vesicles.

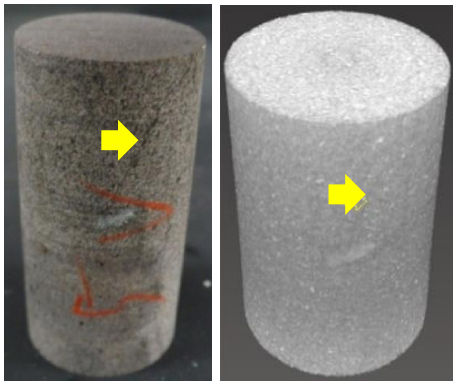

Figure 27. A picture and a 3D CT image of specimen Oxy-4394.5-5V. The yellow arrows indicate a natural fracture.

5.4 Measured Properties and Its Implication

The multistage triaxial compression tests were performed on 15 rock specimens (Table 3). For 4 specimens, N1-4348-3V, Oxy-4394.5-6V and 2 Middle East carbonates, the conventional single stage triaxial tests were performed and the UCS and IFA values are not available.

The measured Young modulus and Poisson's ratios are summarized in Table 4. The Young modulus of each specimen was calculated from the linear portion of the axial strain response to the stress (Figure 28). In our case, the elastic behavior of the rock specimen begins at deviatoric stress, $\sigma_1 - \sigma_3$, 7-14 MPa that is required to close any opened cracks or flaws. The average Poisson's ratio was determined by fitting straight lines to the axial and radial strain curves for the same stress range used for average Young modulus.

Table 3. Tested Specimens and Types.

Lithology	Well	Depth, feet	ID	Test Types
Newberry Tuff	Geo N1	4013	1H	Multistage test
			1V	Multistage test
		4348	2H	Multistage test
			2V	Multistage test
			3V	Conventional triaxial test
			4V	Multistage test
	Geo N2	4219.5	2H	Multistage test
		4281	3V	Multistage test
	Oxy	4394.5	1V	Multistage test
			5V	Multistage test
			6V	Conventional triaxial test
Mancos shale	-	-	#1	Multistage test
	-	-	#2	Multistage test
Middle East Carbonate	-	-	#1	Conventional triaxial test
	-	-	#2	Conventional triaxial test

Table 4. Measured Elastic Properties.

Pc, MPa (psi)	Well	Depth, ft	ID	3.45 (500)	10.34 (1500)	13.79 (2000)	17.24 (2500)	24.14 (3500)	31.03 (4500)
Young Modulus, GPa	N1	4013	1H	25.88	27.23	-	27.83	27.47	27.20
			1V	25.71	28.34	-	28.43	28.20	-
		4348	2H	-	15.18	16.34	16.22	16.40	16.56
			2V	-	11.17	13.40	13.76	13.38	-
			3V	-	-	-	-	13.99	-
			4V	-	13.24	14.27	14.38	14.26	13.76
	N2	4219.5	2H	-	20.90	21.60	18.85	-	20.02
		4281	3V	-	30.48	40.18	41.56	42.81	43.43
	Oxy	4394.5	1V	-	56.94	58.12	58.15	58.75	57.41
			4V	-	-	-	-	-	45.73
			5V	-	53.83	54.75	52.02	48.95	46.35
			6V	-	-	-	-	39.88	-
	Mancos Shale		#1	-	17.49	21.49	22.64	23.78	24.97
			#2	13.26(Pc=6.9MPa)		16.29	17.68(Pc=20.69MPa)		-
	Middle East Carbonate		#1	-	-	29.69	-	-	-
			#2	-	-	35.90	-	-	-
Average Poisson's Ratio	N1	4013	1H	0.31	0.34	-	0.36	0.40	0.42
			1V	0.28	0.33	-	0.36	0.39	-
		4348	2H	-	0.29	0.31	0.30	0.29	0.28
			2V	-	0.32	0.36	0.37	0.36	-
			3V	-	-	-	-	0.22	-
			4V	-	0.31	0.34	0.34	0.33	0.31
	N2	4219.5	2H	-	0.19	0.21	0.19	-	0.20
		4281	3V	-	0.16	0.26	0.27	0.28	0.30
	Oxy	4394.5	1V	-	0.21	0.27	0.26	0.32	0.37
			4V	-	-	-	-	-	0.36
			5V	-	0.32	0.34	0.37	0.39	0.41
			6V	-	-	-	-	0.33	-
	Mancos Shale		#1	-	0.17	0.30	0.33	0.32	0.34
			#2	0.25(Pc=6.9MPa)		0.30	0.33(Pc=20.69MPa)		-
	Middle East Carbonate		#1	-	-	0.32	-	-	-
			#2	-	-	0.31	-	-	-

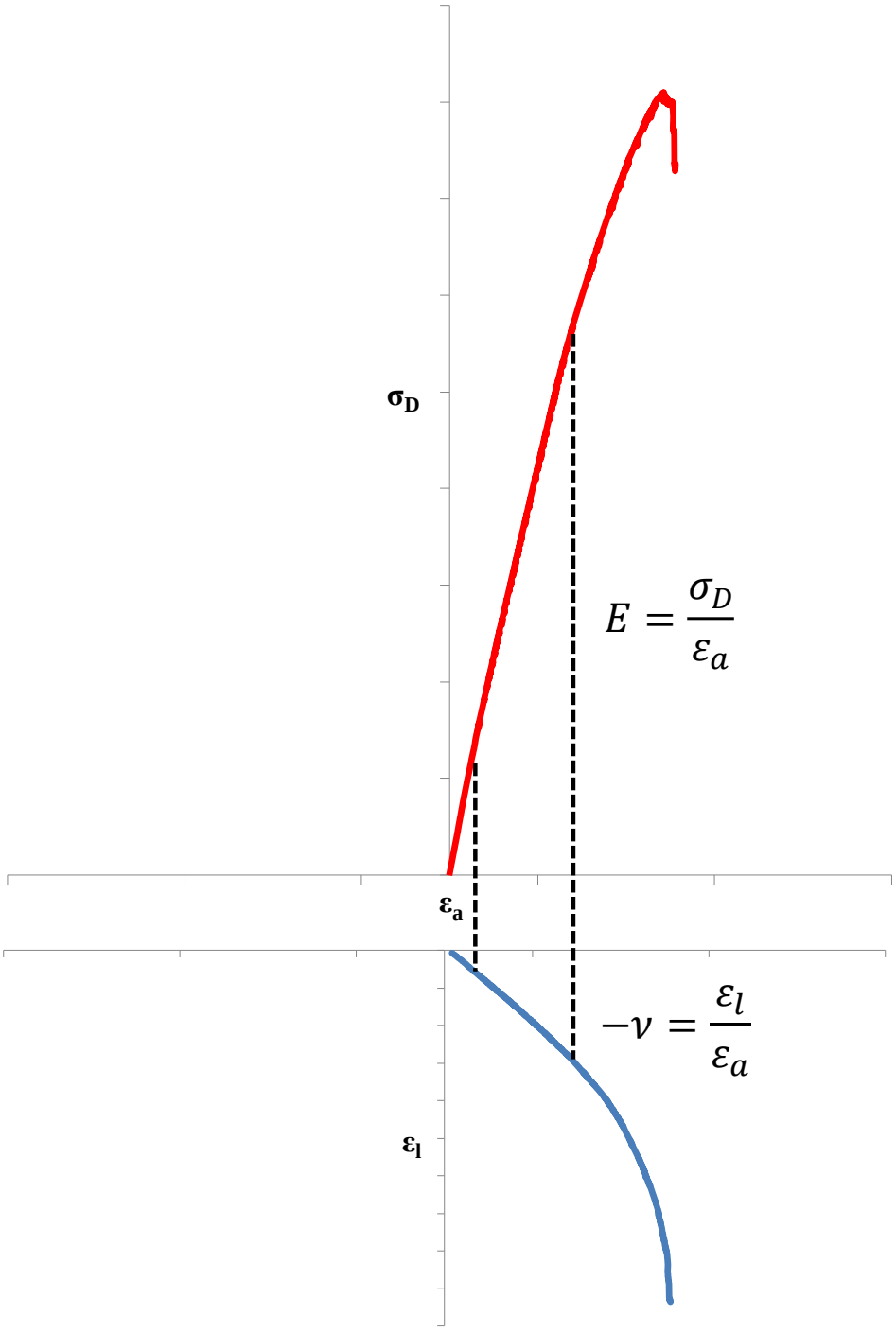

Figure 28. Young modulus and Poisson's ratio calculated from stress-strain curve.

The Mohr circles and the failure envelope are determined from stopping points and the peak strength at the last stage (Figure 11). The left and right edges of the dashed circles are the confining pressure and the axial stress at the stopping points, respectively. Four the solid circles representing the failure point of the rock is drawn with the confining pressure and the compressive strength at the last stage. The failure envelope is shown as a black line with the linear equation in the form of (3.3). A summary of the failure criterion parameters is presented in Table 5.

The unconfined compressive strength (UCS) can be estimated by drawing a circle tangent to the failure envelope (Figure 12). The compressive strength values for given confining pressure conditions were estimated by the same approach.

Table 5. Mohr-Coulomb Failure Criterion Parameters.

Parameter	Well	Depth, ft	ID	Value
Cohesion, MPa	N1	4013	1H	24.73
			1V	32.55
		4348	2H	22.32
			2V	17.04
			4V	29.48
	N2	4219.5	2H	22.06
		4281	3V	61.35
	Oxy	4394.5	1V	61.61
			5V	20.90
	Mancos shale #1			25.76
	Mancos shale #2			29.83
Internal Friction Angle, ^{o}	N1	4013	1H	45.8
			1V	34.0
		4348	2H	23.7
			2V	19.3
			4V	15.6
	N2	4219.5	2H	29.2
		4281	3V	21.3
	Oxy	4394.5	1V	29.7
			5V	40.3
	Mancos shale #1			28.0
	Mancos shale #2			28.9

Table 6. Compressive Strengths.

Pc, MPa	Well	Depth, ft	Plug	3.45	10.34	13.79	17.24	24.14	31.03
Estimated Compressive Strength, MPa	N1	4013	1H	142.85	184.74	-	226.63	268.53	310.42
			1V	134.76	158.9	-	183.30	207.67	232.04
		4348	2H	-	92.61	100.70	108.79	124.97	141.15
			2V	-	68.56	75.41	82.26	95.95	-
			3V	-	-	-	-	122.38	-
			4V	-	95.62	101.61	107.60	119.57	131.54
	N2	4219.5	2H	-	105.35	115.38	125.42	-	165.55
		4281	3V	-	201.61	208.99	216.37	231.13	245.89
	Oxy	4394.5	1V	-	242.78	253.00	263.22	283.66	304.11
			4V	-	-	-	-	-	213.85
			5V	-	170.22	186.26	202.29	234.37	266.45
			6V	-	-	-	-	278.03	-
	Mancos shale #1				114.47	124.03	133.59	152.70	171.82
	Mancos shale #2			120.93 (Pc=6.90 MPa)		140.74	160.55 (Pc=20.69 MPa)		
	Middle East carbonate #1			-	-	117.18	-	-	-
	Middle East carbonate #2			-	-	102.06	-	-	-
Uniaxial Compressive Strength, MPa	N1	4013	1H	121.87					
			1V	122.33					
		4348	2H	68.35					
			2V	48.01					
			4V	77.67					
	N2	4219.5	2H	75.25					
		4281	3V	179.47					
	Oxy	4394.5	1V	212.11					
			5V	122.10					
	Mancos shale #1			85.79					
	Mancos shale #2			101.11					

5.4.1 Post-Peak Behavior

The post-peak behavior on the stress-strain curves is normally used to characterize the brittleness of the tested rock. According to the most commonly used definition of the brittleness, a brittle rock shows sudden stress-drop after the peak stress and a ductile rock maintains the stress level without losing the ability to sustain (Fjar et al., 2008).

The post-peak modulus was measured by the slope between the peak strength and the last point of the test (Table 7). It should be noted that the post-peak modulus is not available for 3 specimens due to the unexpected termination of the test by systematic problem.

The specimens obtained from N1-4348 drill core showed small post-peak modulus as the stress on the specimens sustained after the peak stress (yellow curves in Figure 29). In addition, the post-peak modulus of the Middle East carbonate #2 specimen is -0.7 (green curve in Figure 29). Otherwise, the post peak modulus values vary and are lower than -3.1.

It appears that the specimens with small post-peak modulus have low Young modulus. The N1-4348 specimens have lower Young modulus (13.76 – 15.16 GPa at 31.02 MPa confining pressure), while those of Oxy-4394.5 are much higher (46.36–57.42 GPa at 31.02 MPa confining pressure). However, the Young modulus of the Middle East carbonate #2 specimen was relatively large (35.90 GPa).

Another property which can be related to the post-peak behavior is IFA, which describes the rock strength increment by confinement. It was found that the specimens with the small post-peak modulus have low IFA values (15.6-28.9°). In addition, the N1-4348 specimens have low UCS values (48.01-77.67 MPa).

Table 7. Measured post-peak modulus.

Specimen ID	Post-peak modulus, GPa
N1-4013-1H	-38.14
N1-4013-1V	N/A
N2-4219.5-2H	-16.60
N2-4281-3V	-73.45
Oxy-4394.5-1V	-12.36
Oxy-4394.5-5V	-60.39
Oxy-4394.5-6V	-54.30
N1-4348-2H	-0.83
N1-4348-2V	N/A
N1-4348-3V	-0.23
N1-4348-4V	-0.24
Mancos Shale #1	N/A
Mancos Shale #2	-22.89
ME carbonate #1	-3.10
ME carbonate #2	-0.70

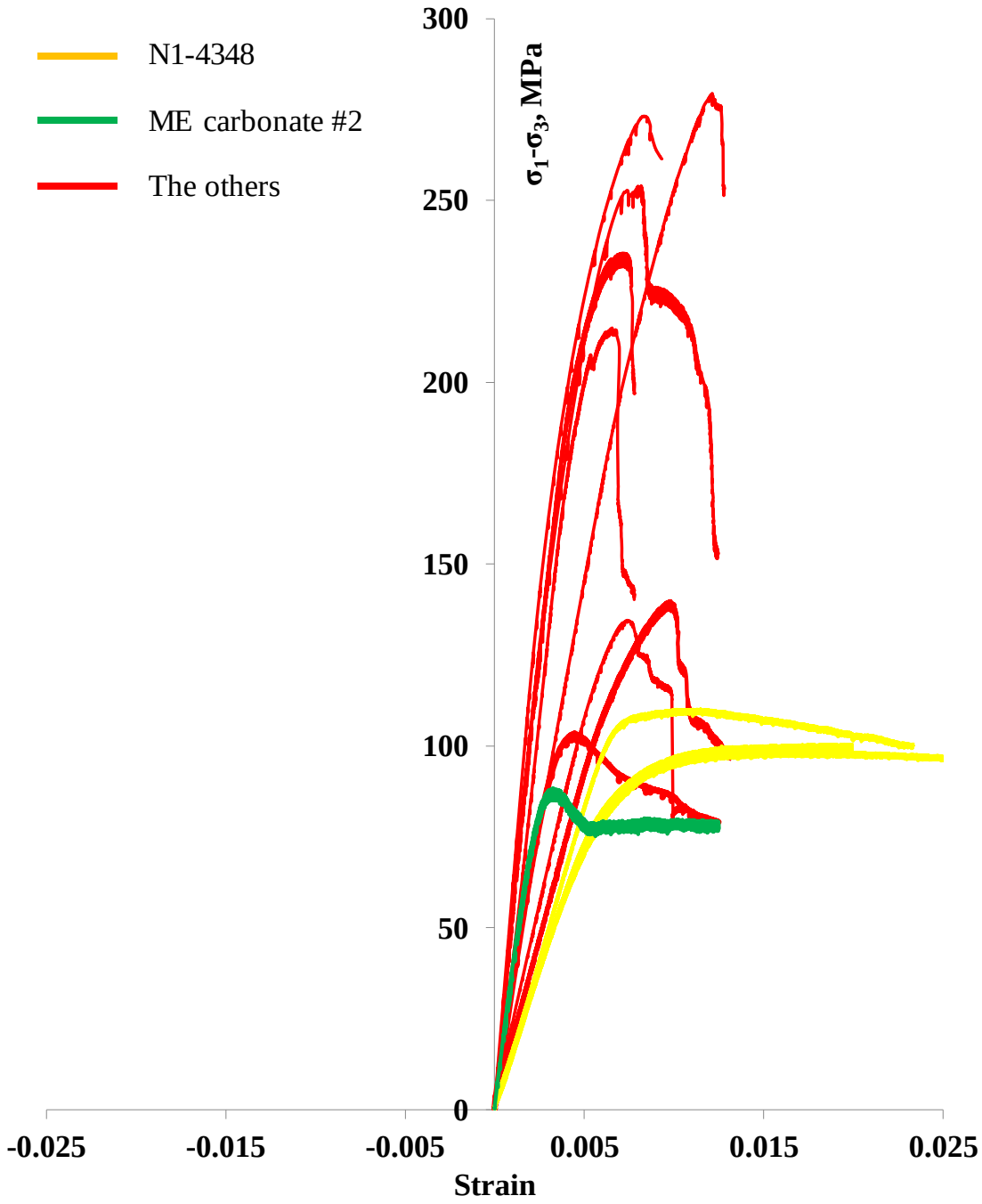

Figure 29. Stress-axial strain curves at the last stage.

5.4.2 Non-Dilatancy

When the rock undergoes irreversible deformation, the volume of the rock increases by microcrack or void formation. The phenomenon is called dilatancy and can be observed on the volumetric strain response obtained during the triaxial test. However, if the failure is accompanied by compaction and pore collapse, dilatancy does not occur as the volume of the rock keeps on decreasing.

As shown in Figure 30, the tested rock specimens showed dilatancy except 3 rock specimens, N1-4348-3V, N2-4219.5-2H and N2-4281-3V. Although the volumes of the non-dilatant rocks increased after the peak stress, their final volumes indicate shrinkage by failure.

The volumetric response of the non-dilatant rocks can be further analyzed with the local Poisson's ratio behavior as described in section 3.1. Figure 31 shows local Poisson's ratio and volumetric strain behaviors of the N1-4013-1H specimen. Under low deviatoric stress, the Poisson's ratio keeps increasing until the open cracks and voids are completely closed. When the rock begins the elastic response, the increment decreases and the local Poisson's ratio remains constant. As the compressive stress rises, the local Poisson's ratio starts to increase again due to formation of new cracks or reopening of existing ones.

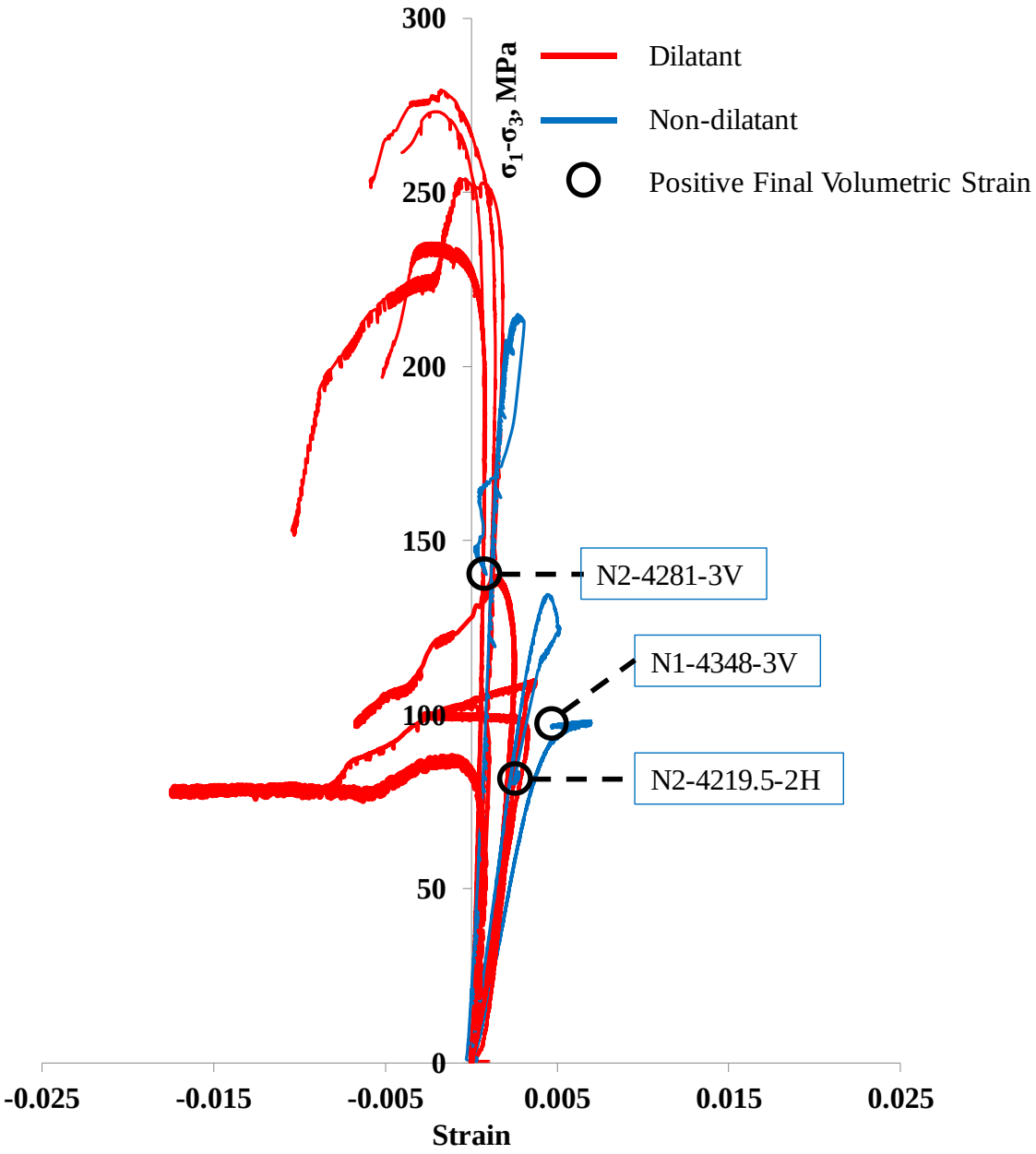

Figure 30. Stress-volumetric strain curves.
The colors indicate dilatancy (red) and non-dilatancy (blue).

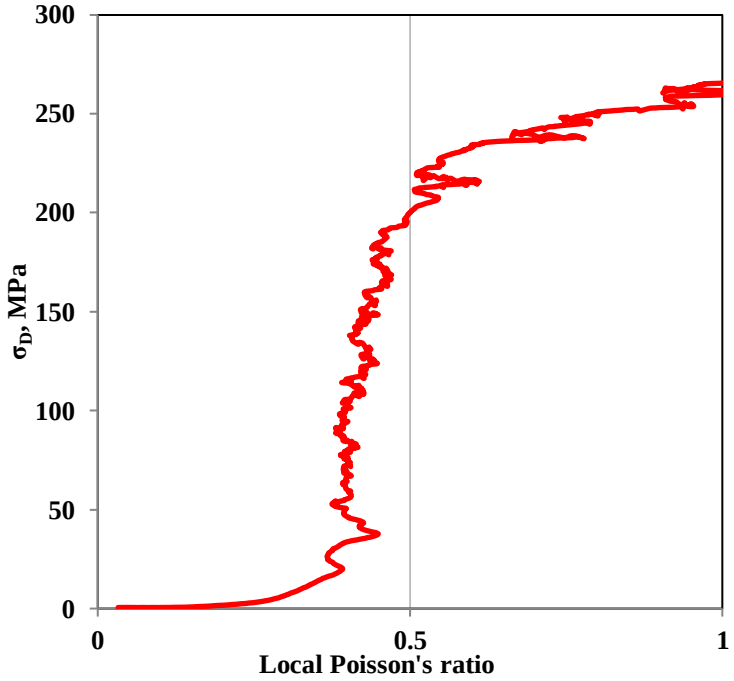

(a)

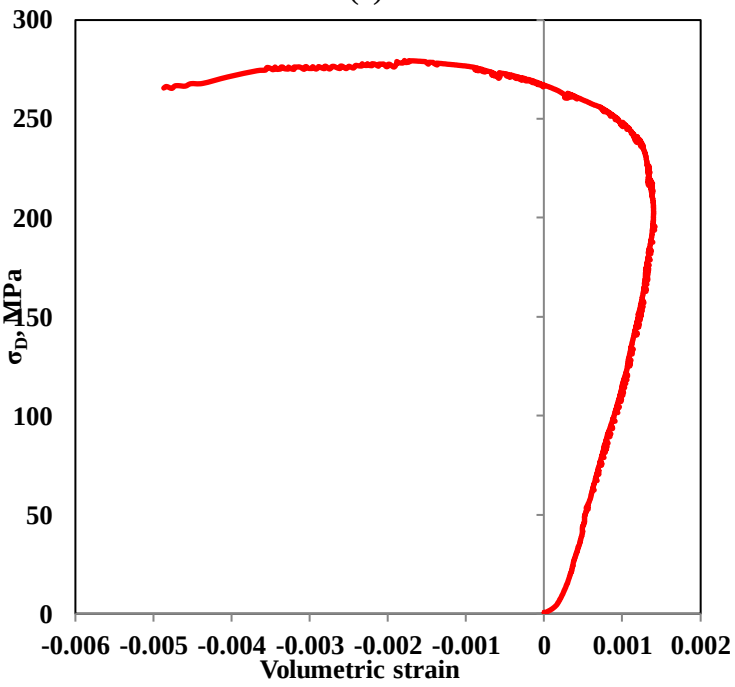

(b)

Figure 31. (a) Local Poisson's ratio and (b) volumetric strain behavior of N1-4013-1H.

On the other hand, the behavior of the non-dilatant rock specimens can be distinguished by the local Poisson's ratio. Although the early time behavior is almost the same, the local Poisson's ratio of the N1-4348-3V remains smaller than 0.5 (Figure 32). The behavior implies that the volume of the rock keeps decreasing until the failure point.

The local Poisson's ratio behavior obtained from the N2-4281-3V shows clearer pore collapse and compaction behavior (Figure 33). Near the failure point, the stress level dropped as the local Poisson's ratio plummeted to negative values (blue circle in Figure 33 (b)). In addition, the same behavior is observed after the rock failure (green circle). It is expected that the clear pore collapse phenomenon can be caused by a number of macro vesicles. These were indeed detected from the CT scanned image (Figure 26 (b)). Meanwhile, the larger oscillations of the local Poisson's ratio might have been caused by the pore collapse as well. The suspicion needs to be analyzed and validated in the future. Consequently, the integrated analysis of the local Poisson's ratio and the volumetric strain behaviors is very useful to investigate the non-dilatancy.

In the same manner, the average Poisson's ratio of the non-dilatant rocks shows very low values (0.20-0.30). Moreover, the N2-4219.5-2H specimen showed the lowest Poisson's ratio as 0.20.

Meanwhile, it was found that the non-dilatancy affects the IFA of the rock. This is because the strength of the rock is not effectively improved by the confinement. The IFA values are 21.3° and 29.2° for the non-dilatant N2-4281-3V and N2-4219.5-2H.

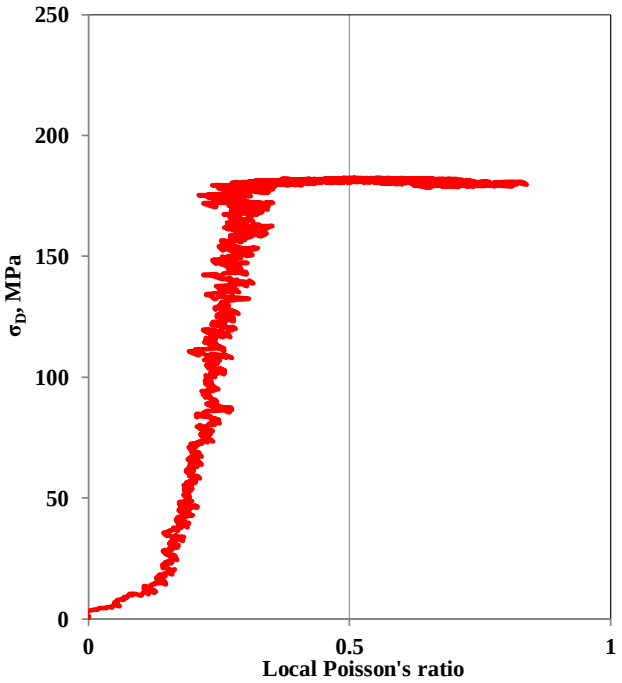

(a)

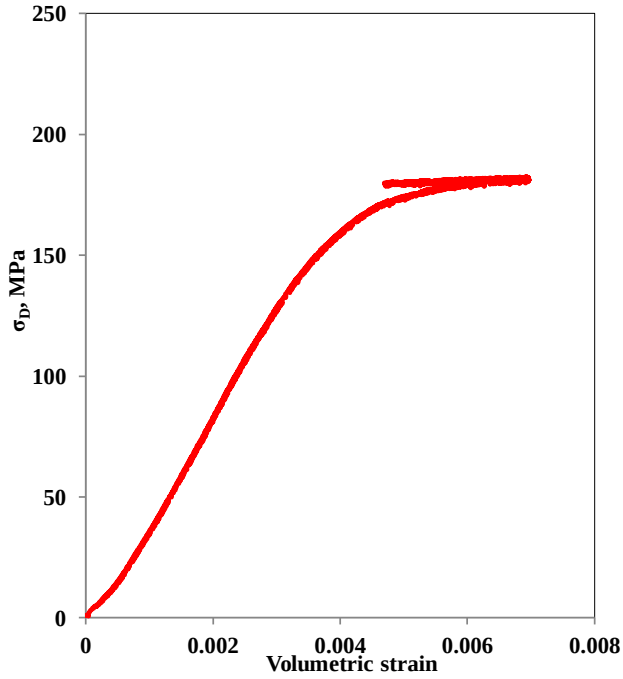

(b)

Figure 32. (a) Local Poisson's ratio and (b) volumetric strain behavior of N1-4348-3V.

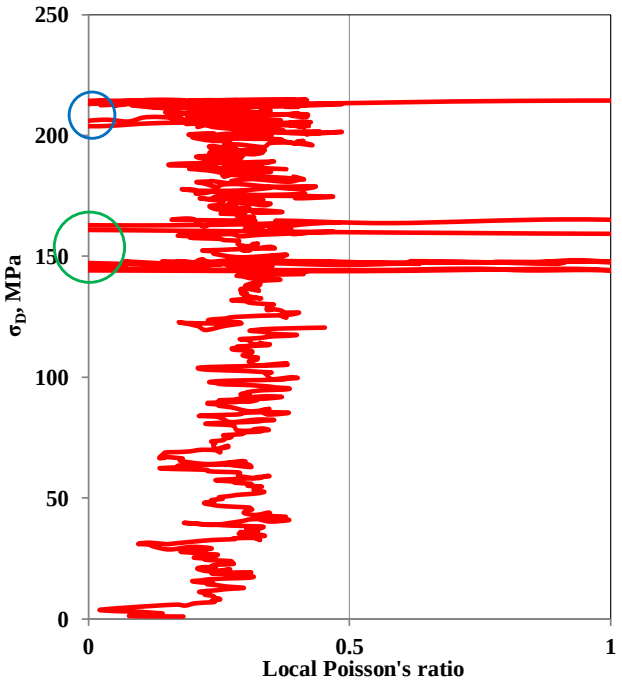

(a)

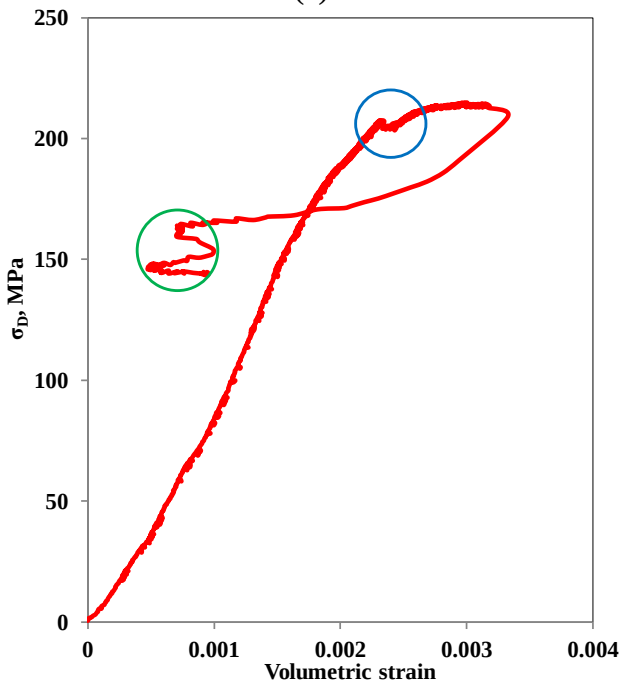

(b)

Figure 33. (a) Local Poisson's ratio and (b) volumetric strain behavior of N2-4281-3V.

5.4.3 Effect of Natural Fracture

Existence of natural fracture has a significant influence on various rock properties (Kovaleva, 1974, Thompson and Brown, 1991). From the CT scanned image analysis in section 5.3, it was found that 3 core specimens contain the natural fractures. In order to analyze the effect of the natural fracture, the measured properties of the specimens were integrated with the other specimens from the same drill core.

The N1-4013-1H specimen contained a vertical natural fracture at the center, while a lateral fracture was observed in the 1V specimen (Figure 25). As shown in Figure 34 (a), the UCS values of both specimens have very small difference of 0.31 MPa (y intercept in Figure 34 (a)). However, the strength increment with confining pressure of 1H is almost twice that of 1V (6.07 vs 3.54 MPa). Since the confinement pressurizes the cylinder-shape rock radially, the strength increment with the confinement is higher for the specimen with vertical discontinuity.

The vertical natural fracture in the Oxy-4394.5-5V induced a similar influence on the rock properties. Even though the UCS of the intact 1V specimen is higher than that of the 5V specimen (212.16 MPa and 122.13 MPa, respectively), the latter has much higher strength increment with confining pressure. Consequently, it is concluded that the IFA values of the specimens with a vertical natural fracture are higher (Table 5).

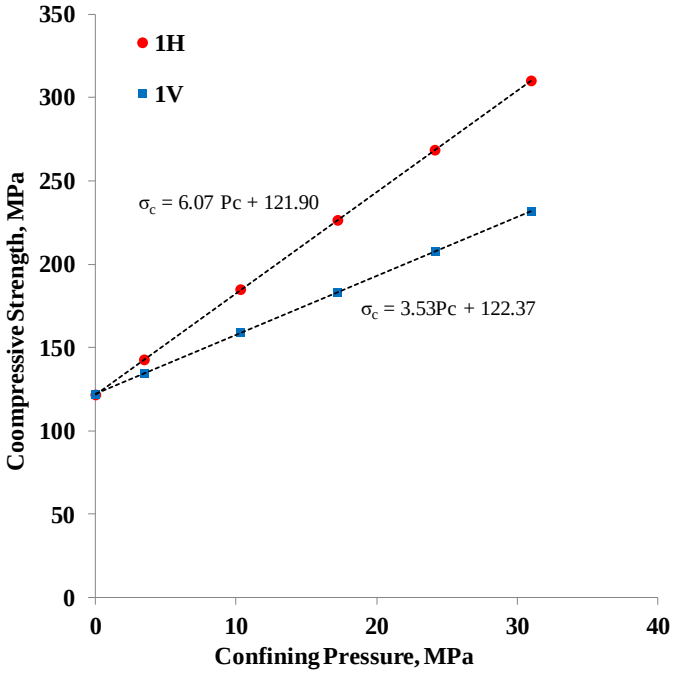

(a)

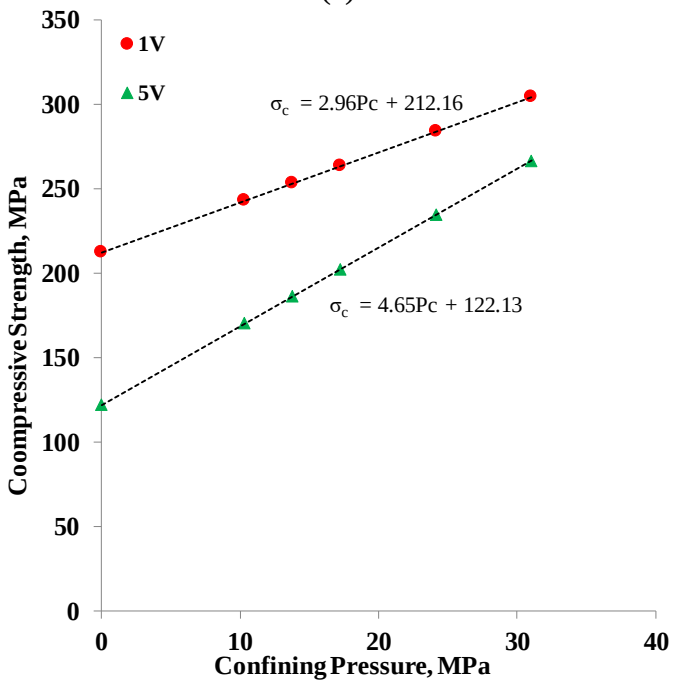

(b)

Figure 34. Compressive strength increment with confining pressure of (a) N1-4013 specimens and (b) Oxy-4394.5 specimens.

5.5 Summary

In this section, the rock mechanical properties of Newberry tuff, Mancos shale and Middle East carbonate specimens were measured by multistage triaxial testing method. The tuff specimens were scanned by X-ray computerized tomography in order to detect the natural fracture or void spaces which would have influence on the measured properties. The specimens N1-4013-1H and 1V contained the vertical and lateral natural fractures which were healed by secondary minerals. The N2-4219.5-2H specimen also contained a healed natural fracture, while many vesicles were observed in the N2-4281-3V. There was a healed fracture detected in the specimen Oxy-4394.5-5V.

The post-peak modulus was measured to quantify the post-peak behavior of rock. It shows that the specimens from N1-4348 drill core and the Middle East carbonate #2 have very small post-peak modulus.

The non-dilatancy of the tested specimens were analyzed with the local Poisson's ratio and the volumetric strain behavior. As a result, it was found that the non-dilatant rocks were deformed and failed with the pore collapse and compaction.

Consequently, the post-peak behavior, non-dilatancy and the existing natural fracture affect the measured properties of the rock specimens. The characteristics will be integrated with the permeability enhancement behavior by failure in section 8.

6. FINITE ELEMENT MODELING OF MULTISTAGE TRIAXIAL TEST[*]

The stress-strain curve is most common tool to represent the behavior of rock under stress. Assuming the rock is purely elastic, the stress-strain response in a test can be estimated using elastic properties, such as Young modulus and Poisson's ratio. However, the behavior of rock is neither pure elastic nor solely represented by a linear relationship.

From the permeability enhancement point of view, analyzing the volumetric strain behavior is crucial because non-dilatancy causes permeability deterioration by pore collapse or flow path compaction (Heap et al., 2015). In spite of its importance, modeling the dilatancy/non-dilatancy phenomenon on the stress-strain curve is complicated since both can occur simultaneously during deformation (Vajdova et al., 2004).

In this section, we provide a simple approach to simulate the nonlinear behavior of the rock below the stopping point. Using 2D FEM model, the stress-strain curves of both dilatant and non-dilatant rock specimens will be constructed by updating local elastic properties.

[*] Reprinted with permission from "Laboratory scale characterization of brittleness and permeability enhancement due to rock failure." by Jihoon Wang, Peter Valko and Ahmad Ghassemi, accepted for publication in forthcoming issue of *International Journal of Oil, Gas and Coal Technology*.

6.1 Formula Derivation

As described in the section 5.4, the tested specimens can be categorized into dilatant and non-dilatant rocks by the volumetric strain behavior. When the rock is dilatant, the volume starts to increase at a certain stress level as the local Poisson's ratio attains 0.5 (Figure 7). For non-dilatant rocks, however, the phenomenon is not present as its volume keeps decreasing with increasing stress. Therefore, the local Poisson's ratio behavior is a key parameter to simulate the stress-strain behavior of the rock during the multistage triaxial test.

6.1.1 Dilatant Rocks

Assuming the axial strain response to the stress is linear, the nonlinearity of the lateral strain is described with a simple power law relation. The axial and lateral strains can be expressed with the stress level.

$$\frac{\varepsilon_a}{\varepsilon_{a,dil}} = \frac{\sigma}{\sigma_{dil}} \tag{6.1}$$

$$\frac{\varepsilon_l}{\varepsilon_{l,dil}} = \left(\frac{\sigma}{\sigma_{dil}}\right)^{\delta} \tag{6.2}$$

where, $\varepsilon_{a,dil}$, $\varepsilon_{l,dil}$ and σ_{dil} are the axial strain, lateral strain and the stress at the dilatancy point. Here δ is the power law index of the lateral strain behavior, and nonlinear behavior is indicated by $0 < \delta < 1$. The local Poisson's ratio, ν_{local} can be calculated as the ratio of derivatives:

$$\nu_{local} = -\frac{d\varepsilon_l}{d\varepsilon_a} = -\frac{\frac{d\varepsilon_l}{d\sigma}}{\frac{d\varepsilon_a}{d\sigma}} = -\frac{\varepsilon_{l,dil}\left(\frac{\sigma}{\sigma_{dil}}\right)^{\frac{1}{\delta}-1} \Big/ \delta\,\sigma_{dil}}{\varepsilon_{a,dil}/\sigma_{dil}} = -\frac{1}{\delta}\frac{\varepsilon_{l,dil}}{\varepsilon_{a,dil}}\left(\frac{\sigma}{\sigma_{dil}}\right)^{\frac{1}{\delta}-1} \tag{6.3}$$

Since the local Poisson's ratio is 0.5 at the dilatancy point, (6.3) can be re-written as

$$-\frac{1}{\delta}\frac{\varepsilon_{l,dil}}{\varepsilon_{a,dil}} = 0.5 \tag{6.4}$$

Therefore, the power law index δ is given by,

$$\delta = -\frac{2\,\varepsilon_{l,dil}}{\varepsilon_{a,dil}} \tag{6.5}$$

Similarly, the nonlinearity on the axial strain behavior can be also estimated.

$$\frac{\sigma}{\sigma_{dil}} = \left(\frac{\varepsilon_a}{\varepsilon_{a,dil}}\right)^{\gamma}, \quad 0 < \gamma \leq 1 \tag{6.6}$$

where, γ is the power law index of the axial strain behavior. If the nonlinearity on the axial strain exists, the local Poisson's ratio can be obtained from

$$\nu_{local} = -\frac{d\varepsilon_l}{d\varepsilon_a} = -\frac{\frac{d\varepsilon_l}{d\sigma}}{\frac{d\varepsilon_a}{d\sigma}} = -\frac{\varepsilon_{l,dil}\left(\frac{\sigma}{\sigma_{dil}}\right)^{\frac{1}{\delta}-1} \Big/ \delta\,\sigma_{dil}}{\varepsilon_{a,dil}\left(\frac{\sigma}{\sigma_{dil}}\right)^{\frac{1}{\gamma}-1} \Big/ \gamma\,\sigma_{dil}} = -\frac{\gamma}{\delta}\frac{\varepsilon_{l,dil}}{\varepsilon_{a,dil}}\left(\frac{\sigma}{\sigma_{dil}}\right)^{\frac{1}{\delta}-\frac{1}{\gamma}} \quad (6.7)$$

The stress at the dilatancy point is calculated by the measured Young modulus.

$$\sigma_{\text{dil}} = E\varepsilon_{a,\text{dil}} \quad (6.8)$$

Figure 35 shows the measured and calculated local Poisson's ratio behaviors at the last stage of the test. At the early time, the local Poisson's ratio steeply increases as 35 MPa of stress is required to close the loosen pore space, microcracks, etc. and to yield elastic response. The suggested nonlinear model provides a fairly good match with the measured data until the dilatancy point. The input data is shown in Table 8.

Table 8. Input parameters for local Poisson's ratio calculation of N1-4013-1H.

Parameter	Value
γ	0.850
$\varepsilon_{a,dil}$	0.0078
$\varepsilon_{l,dil}$	-0.0032
δ	0.697

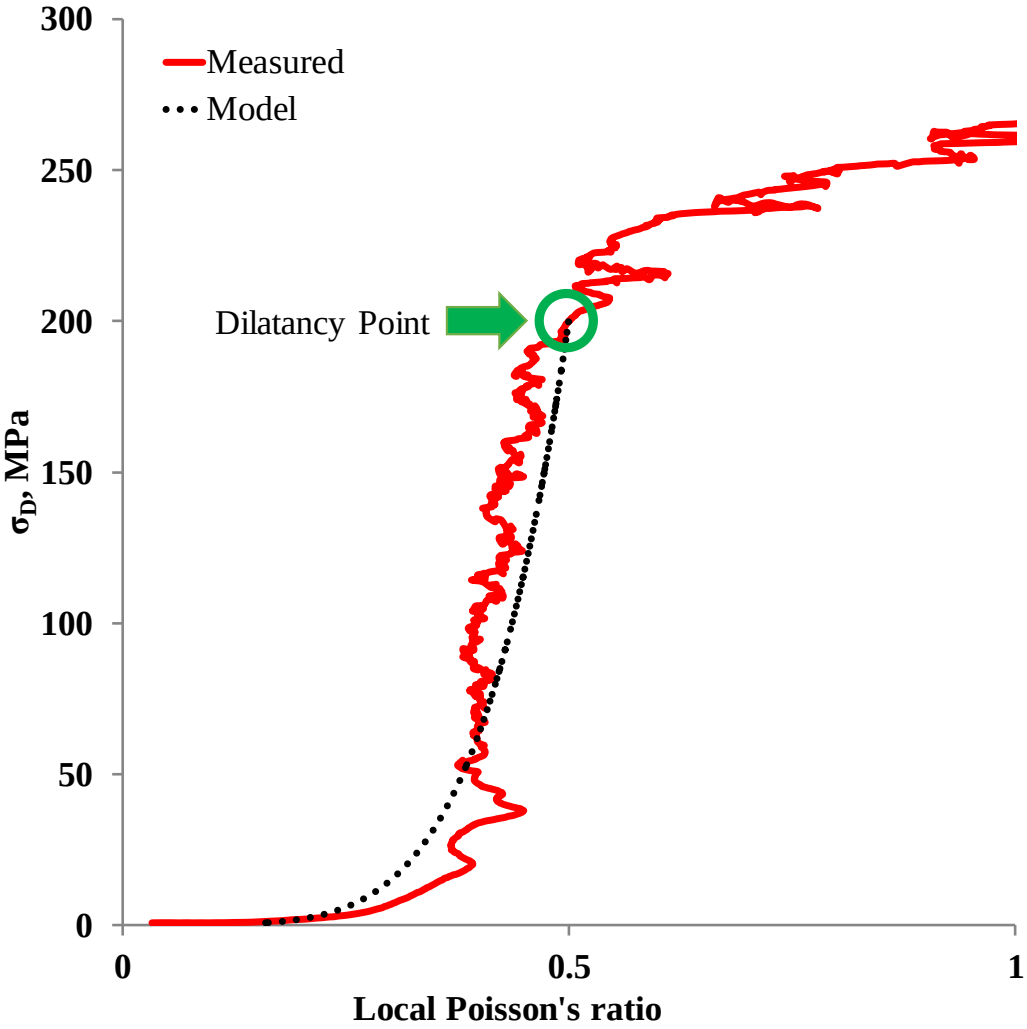

Figure 35. Local Poisson's ratio versus stress of N1-4013-1H at the last stage.

6.1.2 Non-Dilatant Rocks

The non-dilatant behavior is observed from 3 rock specimens, N1-4348-3V, N2-4219.5-2H and N2-4281-3V. As shown in Figure 7 (b), the local Poisson's ratio of non-dilatant specimen does not reach 0.5 until the rock specimen starts irreversible deformation. Recalling (6.3), the local Poisson's ratio for non-dilatancy can be modelled with the suggested method. Unlike the dilatant rock, the local Poisson's ratio at the stopping point is less than 0.5.

$$\frac{1}{\delta_{ND}}\frac{\varepsilon_{l,ND}}{\varepsilon_{a,ND}} = -\nu_{local,ND} \tag{6.9}$$

where, $\varepsilon_{a,ND}$ and $\varepsilon_{l,ND}$ are the axial and lateral strains of the non-dilatant rock and $\nu_{local,ND}$ is the local Poisson's ratio of the non-dilatant rock at the stopping point. Then the power law index δ_{ND} is given by,

$$\delta_{ND} = -\frac{1}{\nu_{local,ND}}\frac{\varepsilon_{l,ND}}{\varepsilon_{a,ND}}\gamma \tag{6.10}$$

Consequently, the local Poisson's ratio of the non-dilatant rock can be calculated by rearranging (6.7)

$$\nu_{local} = -\frac{\gamma}{\delta_{ND}} \frac{\varepsilon_{l,ND}}{\varepsilon_{a,ND}} \left(\frac{\sigma}{\sigma_{ND}}\right)^{\frac{1}{\delta_{ND}} - \frac{1}{\gamma}} \tag{6.11}$$

where σ_{ND} is the stress at the stopping point.

The local Poisson's ratio behavior of the non-dilatant N2-4219.5-2H specimen is shown in Figure 36. It is expected that the main failure mechanism of the rock is pore collapse and compaction, because the rock is not even dilatant at failure. Moreover, the rock undergoes shrinkage both axially and laterally as the local Poisson's ratio plummets to the negative value. Although it starts to increase later, the phenomenon would considerably deteriorate the permeability of the rock.

Meanwhile, the calculated local Poisson's ratio represents well the measured values up to the stopping point. The used parameters are described in Table 9.

Table 9. Input parameters for local Poisson's ratio calculation of N2-4219.5-2H.

Parameter	Value
γ	0.8
$\varepsilon_{a,ND}$	0.00616
$\varepsilon_{l,ND}$	-0.00121
δ_{ND}	0.746
$\nu_{local,ND}$	0.210

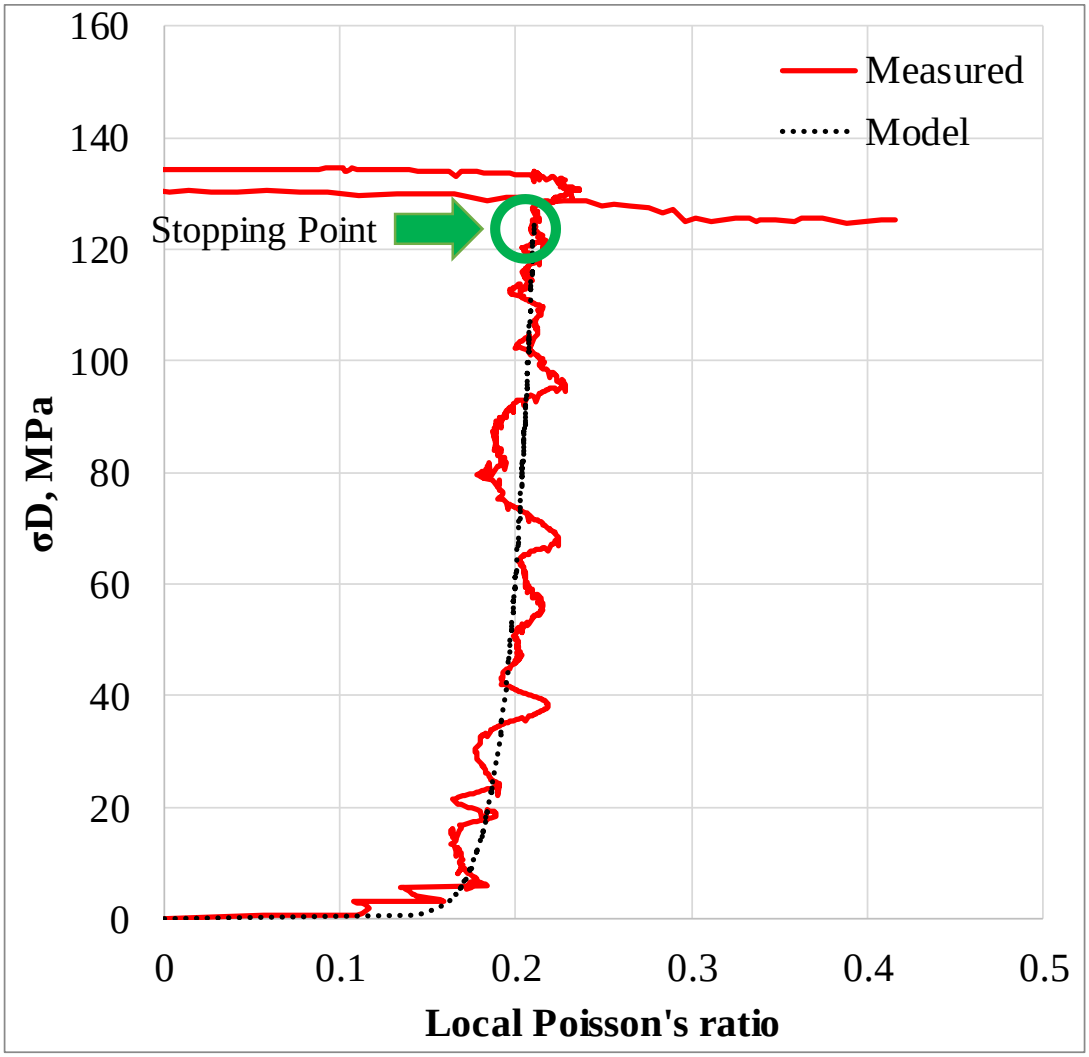

Figure 36. Local Poisson's ratio versus stress of N2-4219.5-2H at the last stage.

6.2 2D Finite Element Method Approach for Multistage Triaxial Tests

The multistage triaxial tests were computationally performed with the FEM model consisting of 435 rectangular elements (Figure 37). The plane stress approach was chosen to formulate the stress-strain behavior over the plane strain. Since the plane strain approach restricts the strain in z-direction, the lateral strain and the dilatancy behavior would be exaggerated.

The tests performed on the dilatant Mancos shale #2 and the non-dilatant N2-4219.5-2H were modeled until the stopping point for each stage. Controlling the axial strain for 100 timesteps, the local Young modulus and the local Poisson's ratio parameters were updated every timestep. The stress value was calculated from the displacement at each element.

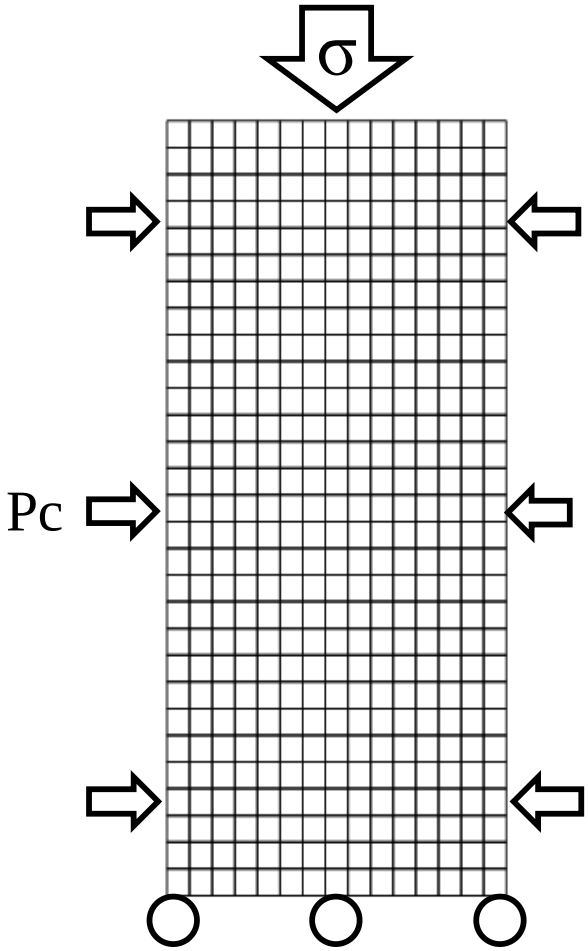

Figure 37. Constructed 2D FEM mesh for multistage triaxial test simulation.

6.2.1 Mancos Shale #2

The Mancos shale #2 specimen was tested under 3 stages. The rock shows dilatancy with relatively low Poisson's ratio (0.25-0.33). With the input parameters described in Table 10, the stress-strain curves for 3 stages were formulated (Figure 38). The FEM with stress dependent local Poisson's ratio reproduced the lateral strain behavior with good accuracy. Meanwhile, the axial strain behavior at the last stage shows discrepancy due to increased nonlinearity.

Table 10. Input Parameters for Mancos Shale #2.

Parameter	Stage1	Stage2	Stage3
Confining pressure, MPa	6.9	13.79	20.69
Young modulus, GPa	13.26	16.29	17.68
$\varepsilon_{a,dil}$	0.005389	0.005944	0.006798
$\varepsilon_{l,dil}$	-0.00098	-0.0016	-0.00216
γ	1.0	0.93	0.88
δ	0.3674	0.5004	0.5542

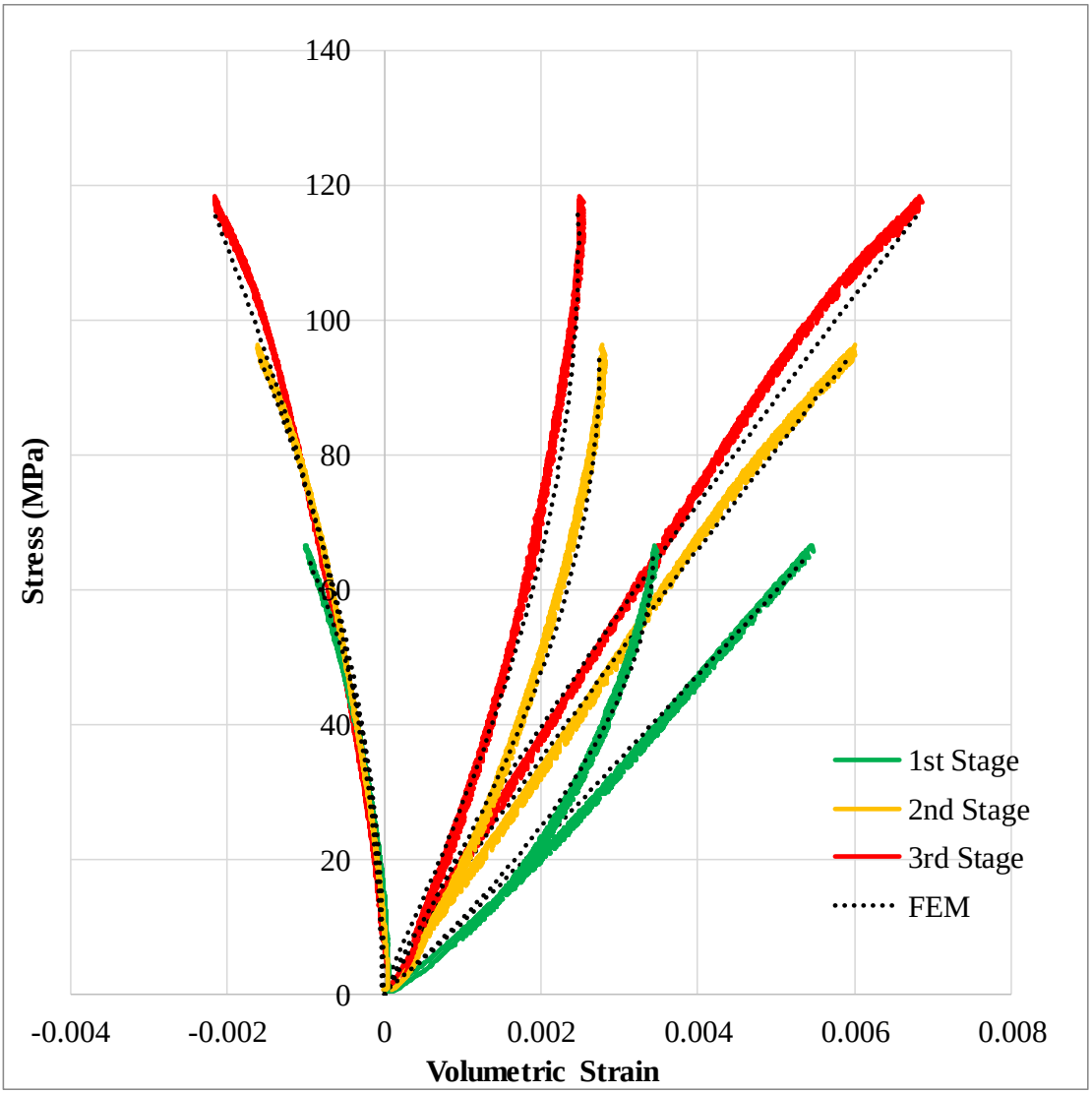

Figure 38. Stress-strain curves of Mancos shale #2 specimen formulated by 2D FEM approach.

6.2.2 N2-4219.5-2H

The multistage triaxial test on the non-dilatant N2-4219.5-2H specimen was tested under 4 stages. The rock showed the lowest average Poisson's ratio in this study (0.19-0.21). Using the formulas derived for non-dilatant rocks, (6.10) and (6.11), the local elastic properties were updated in every timestep using the input parameters shown in Table 11. The FEM results are shown with the measured stress-strain curves in Figure 39. At the first 2 stages, the measured lateral stress-strain behavior is well matched by the FEM model (Figure 39 (a)). However, the axial strain behavior is less accurately reproduced by the FEM results. This is because the stopping point for the non-dilatant rock is when the nonlinearity on the axial strain is observed. Although the discrepancy at low stress levels is larger, the actual stress-strain behavior near the stopping points is well represented with the FEM results.

Table 11. Input Parameters for N2-4219.5-2H.

Parameter	Stage1	Stage2	Stage3	Stage4
Confining pressure, MPa	10.34	13.79	17.24	31.03
Young modulus, GPa	20.90	21.60	18.85	20.02
$\nu_{local,ND}$	0.22	0.23	0.24	0.21
$\varepsilon_{a,ND}$	0.003713	0.004345	0.005614	0.006156
$\varepsilon_{l,ND}$	-0.00067	-0.00104	-0.00124	-0.00121
γ	0.8	0.8	0.8	0.8
δ_{ND}	0.7541	0.7659	0.7068	0.7458

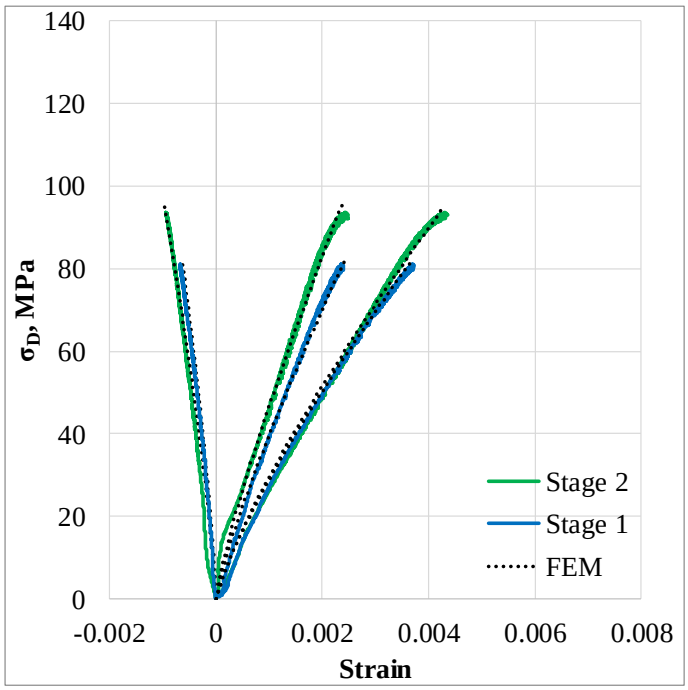

(a)

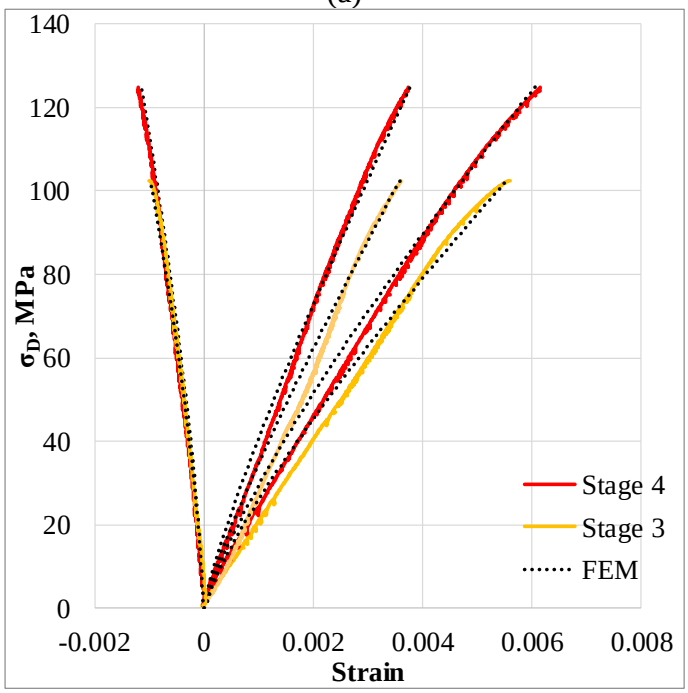

(b)

Figure 39. Stress-strain curves of N2-4219.5-2H specimen formulated by 2D FEM approach. (a) 1st and 2nd stages and (b) 3rd and 4th stages.

6.3 Summary

In this section, the stress-strain behavior during the multistage triaxial test was modeled with a 2-D FEM model with locally updated elasticity parameters. The rock dilatancy was closely analyzed with the local Poisson's ratio behavior until the dilatancy or stopping points. Using a power law function, formulas for the local elasticity parameters were derived. It was found that the local Poisson's ratio of both dilatant and non-dilatant rocks can be reliably represented by the suggested formula based on the power law assumption.

With stress dependent elastic properties, the FEM model showed remarkable ability to reproduce the experimental data involving both specimens.

7. BRITTLENESS QUANTIFICATION BY BRITTLENESS INDEX THEORIES[*]

The brittleness index theories have been widely used in the field of petroleum engineering to assess the reservoir productivity when the hydraulic fracturing process is applied. Although many theories were proposed, the consensus on the quantification method and the reliability has not been reached yet.

In this section, the brittleness index theories available in the literatures will be reviewed. Based on the availability of the measured data, the brittleness indices to be used in this study will be selected. Finally, the brittleness index for the rock specimens will be calculated and analyzed.

7.1 Brittleness Index Theories

Due to its importance and attractiveness, a great number of approaches have been suggested for brittleness quantification. Table 12 shows the summary of the 19 brittleness index theories available in the literature.

[*] Reprinted with permission from "Laboratory scale characterization of brittleness and permeability enhancement due to rock failure." by Jihoon Wang, Peter Valko and Ahmad Ghassemi, accepted for publication in forthcoming issue of *International Journal of Oil, Gas and Coal Technology*.

Table 12. Proposed Methods for Brittleness Index Determination.

Source	Characteristics of brittleness	Formula	Description	Reference
Stress-Strain Curve	Higher reversible strain before failure	$\frac{\varepsilon_r}{\varepsilon_T} \cdots [1]$	ε_T : Total strain ε_e : Elastic strain ε_r : Reversible strain ε_P : Post-peak strain ε_{Tp} : Total irreversible post-peak strain W_e : Elastic energy W_r : Reversible energy W_T : Total energy W_{ir} : Pre-peak irreversible energy	Coates and Parsons (1966), Hucka and Das (1974)
	Higher reversible energy before failure	$\frac{W_r}{W_T} \cdots [2]$		Hucka and Das (1974)
		$\frac{W_{ir}}{W_e} \cdots [3]$		
	Higher reversible strain after failure	$\frac{\varepsilon_P}{\varepsilon_e} \cdots [4]$		He et al. (1990)
		$\frac{\varepsilon_{Tp}}{\varepsilon_e} \cdots [5]$		
	Low capacity of sustaining failure from the elastic energy	$\frac{dW_r}{dW_e} = \frac{M-E}{M} \cdots [6]$	dWr : post-peak rupture energy, dWe : withdrawn elastic energy dWα : released energy M : post-peak modulus E : unloading elastic modulus	Tarasov (2011)
		$\frac{dW_\alpha}{dW_e} = \frac{E}{M} \cdots [7]$		
		$\frac{M}{M+E} \cdots [8]$		Bergman and Stille (1983)
		$\frac{M}{E} \cdots [9]$		
Strength	Higher ratio of compressive to tensile strength	$\frac{\sigma_c - \sigma_t}{\sigma_c + \sigma_t} \cdots [10]$	σ_c : Compressive strength σ_t : Tensile strength	Altindag (2003)
		$\frac{\sigma_c}{\sigma_t} \cdots [11]$		
		$\frac{\sigma_c \times \sigma_t}{2} \cdots [12]$		

Table 12. Continued

Strength	Higher UCS (Unconfined Compressive Strength)	$UCS\ or = \frac{UCS}{S_{max}}\ if\ S_H > S_V \cdots [13]$	S_{max} : Maximum in-situ stress	Su et al. (2014)
Mohr's Failure Envelope	Higher IFA	$\sin(IFA) \cdots [14]$	-	Hucka and Das (1974)
Protodyakonov Impact Test	Formation of fines when impacted	$q \times UCS \cdots [15]$	q : Percentage of fines formed (-28 mesh) in the test	Hucka and Das (1974)
Indentation Test	More fractures are generated	$\frac{H_u - H}{constant} \cdots [16]$	H_u : Micro- H : Macro-indentation hardness	Hucka and Das (1974)
Elastic Properties	Higher Young modulus and Lower Poisson's ratio	$\frac{E_B + \nu_B}{2} \cdots [17]$	$E_B = \frac{E-1}{8-1} \times 100\ [10^6 \times psi]$ $\nu_B = \frac{\nu - 0.4}{0.15 - 0.4} \times 100$	Rickman et al. (2008)
Mineral Composition	Lower Clay, Calcite and Total Organic Content(TOC)	$\frac{V_{SiO_2}}{V_{Clay} + V_{CaCO_3} + V_{SiO_2}} \cdots [18]$		Jarvie et al. (2007)
		$\frac{V_{SiO_2} + V_{Dolo}}{V_{Clay} + V_{Dolo} + V_{CaCO_3} + V_{SiO_2} + TOC} \cdots [19]$		Wang and Gale (2009)

Since the stress-strain curve is one of the most common tools to analyze the rock behavior under the stress, the concept of the brittleness using the post-peak behavior on the curve is widely used, especially in the lab scale data analysis (Fjar et al., 2008). On the stress-strain curves, brittle rocks lose the stress sustainability right after the peak strength, while ductile rocks do not lose the ability to sustain the stress even after the peak strength.

In the same manner, brittleness indices based on stress-strain curves focus on the strain or strain energy which the rock specimen absorbs under external force. The strain energy indicates the surrounded area by the stress-strain curve (shaded area in Figure 40). If the rock is brittle, the absorbed energy is released by creating a set of fractures. However, if the rock is ductile, the absorbed energy is not released and is stored in the rock.

Coates and Parsons (1966) proposed the index quantified with elastic strain and the total strain on a pre-failure part of stress-strain curve ([1], Figure 40 (a)).

$$BI\ [1] = \frac{\varepsilon_r}{\varepsilon_T} \tag{7.1}$$

where, ε_r is the reversible strain and ε_T is the total strain before the peak strength. According to the authors, if the irreversible strain is larger, then the rock has a capacity to hold the strain energy and is more likely to behave ductile. They suggested that the rock is ductile if more than 25% of the total strain before failure is permanent.

Based on a similar idea, Hucka and Das (1974) suggested the formulas ([2] and [3]) using the reversible and irreversible strain energy (shaded areas in Figure 40 (a)).

$$BI\ [2] = \frac{W_r}{W_T} \tag{7.2}$$

$$BI\ [3] = \frac{W_{ir}}{W_e} \tag{7.3}$$

where, W_r is the reversible strain energy, W_T is the total strain energy, W_{ir} is the irreversible strain energy and W_e is the elastic strain energy. Adopting the concept of the strain energy, the brittleness indices [2] and [3] take into account for the stress level for a given strain values. [2] focuses on the pre-failure state of the rock, while [3] calculates the strain energy from the elastic behavior of the rock.

The indices proposed by He et al. (1990) ([4] and [5]) focus on the post-failure strain behavior.

$$BI\ [4] = \frac{\varepsilon_P}{\varepsilon_e} \tag{7.4}$$

$$BI\ [5] = \frac{\varepsilon_{Tp}}{\varepsilon_e} \tag{7.5}$$

where, ε_P is the post-peak strain, ε_e is the elastic strain and ε_{Tp} is the total irreversible post-peak strain (Figure 40 (b)). The authors indicated that the brittleness

index is the failure property of rock and the formula needs to contain the failure behavior.

Tarasov (2010; 2011) and Tarasov and Randolph (2011) suggested two formulas for the brittleness index calculation. Focusing on the failure process of the rock, the authors suggested that the brittleness can be quantified with the withdrawn elastic energy and the post-peak rupture energy during failure.

$$BI\ [6] = \frac{dW_r}{dW_e} = \frac{M - E}{M} \tag{7.6}$$

$$BI\ [7] = \frac{dW_\alpha}{dW_e} = \frac{E}{M} \tag{7.7}$$

where, dW_r is the post-peak rupture energy, dW_e is the withdrawn elastic energy, dW_α is the released energy during rock failure, M is the post-peak modulus and E is the unloading elastic modulus. The authors insisted that the value calculated from the equations above determines the capacity of the self-sustaining the failure from the elastic energy (Figure 40 (b)). An absolutely brittle rock has a value of 0 in [6] and 1 in [7].

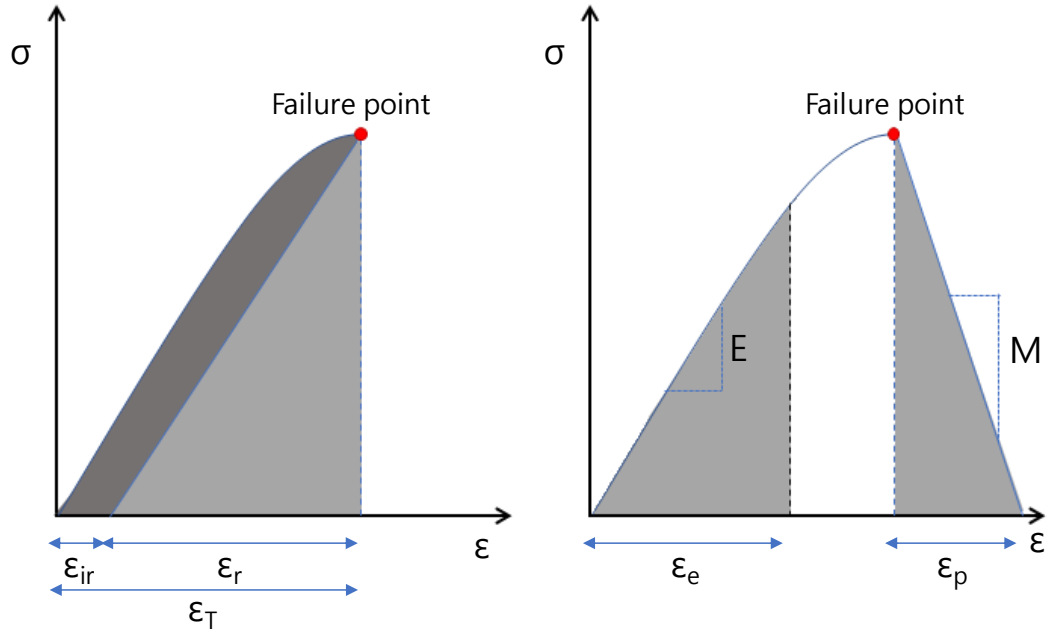

(a) (b)

Figure 40. Identical stress-strain curves and the parameters used in the BI calculation. (a) A curve unloaded at the failure point and (b) a full curve.

Bergman and Stille (1983) suggested a similar method for brittleness calculation using M and E.

$$BI\ [8] = \frac{M}{M + E} \tag{7.8}$$

$$BI\ [9] = \frac{M}{E} \tag{7.9}$$

However, the indices [8] and [9] were found to be inconsistent because of a zone of discontinuity in calculated value (Tarasov and Potvin, 2013).

Assuming that more brittle rock will have higher compressive strength and lower tensile strength, Altindag (2003) suggested 3 equations representing the ratio between compressive and tensile strengths of the rock.

$$BI\ [10] = \frac{\sigma_c - \sigma_t}{\sigma_c + \sigma_t} \tag{7.10}$$

$$BI\ [11] = \frac{\sigma_c}{\sigma_t} \tag{7.11}$$

$$BI\ [12] = \frac{\sigma_c \times \sigma_t}{2} \tag{7.12}$$

where, σ_c is the compressive strength and σ_t is the tensile strength.

Focusing on drilling penetration rate prediction, the author found that the index [12] is the best predictor on the drillability.

UCS is one of the most widely used rock properties in brittleness characterization (Hajiabdolmajid et al., 2000, Hucka and Das, 1974, Su et al., 2014). Moreover, Su et al. (2014) insisted that the ratio of UCS to the maximum in-situ stress characterizes the rock over-consolidation and directly represents the rock brittleness.

$$BI\ [13] = \ UCS\ \ or\ \ \frac{UCS}{S_{max}} \tag{7.13}$$

where, S_{max} is the maximum in-situ principal stress.

Not only did Hucka and Das (1974) summarize the proposed brittleness indices, but they also suggested a BI which can be quantified with the Mohr failure envelope. According to the description, the internal friction angle can be used as a brittleness indicator, since brittle rocks have higher friction angles than ductile rocks.

$$BI\ [14] = \ \sin(IFA) \tag{7.14}$$

The next two indices are derived from specific testing methods. [15] relies on the idea that more fines are formed during an impact test if the rock sample is more brittle. Index [16] can be calculated from micro- and macro-indentation hardness.

$$BI\ [15] = \mathrm{q} \times \mathrm{UCS} \tag{7.15}$$

$$BI\ [16] = \frac{H_u - H}{constant} \tag{7.16}$$

where, q is the percentage of fines larger than 28 mesh formed during the impact test, H_u and H are the micro- and macro-indentation hardness, respectively.

In [16], the macro hardness is always lower than the micro hardness because more fractures are generated during the macro-indentation test. However, this approach is not recommended due to its imprecision (Hucka and Das, 1974).

One of the most widely used brittleness indices in the petroleum industry is due to Rickman et al. (2008). The main idea is that a more brittle rock has higher Young modulus and lower Poisson's ratio. The elastic properties or at least their dynamic variants can be obtained from measured wave velocities during standard well logging.

$$BI\ [17] = \frac{E_B + \nu_B}{2} \tag{7.17}$$

where, E_B and ν_B are given by

$$E_B = \frac{E - 1}{8 - 1} \times 100 \tag{7.18}$$

$$\nu_B = \frac{\nu - 0.4}{0.15 - 0.4} \times 100 \tag{7.19}$$

where, E is the Young modulus with the unit of 10^6 psi and ν is the Poisson's ratio.

Another approach was proposed by Jarvie et al. (2007), who focused on mineralogy. The authors suggested an index that can be calculated from volume fraction

of quartz, calcite and clay in the rock. Wang and Gale (2009) revised the equation by adding dolomite and total organic content to the list of predictors.

$$BI\ [18] = \frac{V_{SiO_2}}{V_{Clay} + V_{CaCO_3} + V_{SiO_2}} \tag{7.20}$$

$$BI\ [19] = \frac{V_{SiO_2} + V_{Dolo}}{V_{Clay} + V_{Dolo} + V_{CaCO_3} + V_{SiO_2} + TOC} \tag{7.21}$$

7.2 Brittleness Selection

Prior to the brittleness quantification from the measured rock properties, it is necessary to select the appropriate methods among the 19 indices reviewed in the previous section.

There are 9 brittleness indices using the stress-strain behavior of the rock. The indices [1-3] appears inappropriate because there is no correlation between the pre-failure and post-failure behavior of the rock (Tarasov and Potvin, 2013). There are more researches insisting that the brittleness needs to be correlated with the failure properties, not the properties obtained from the pre-failure state of the rock (He et al., 1990, Safari et al., 2015).

[4-5] might be misleading if the triaxial test is not performed until the residual strength of rock specimen is very small. However, the tests in this study were finished before the axial strain reaches 2% in order to avoid the system damage.

[8-9] do not yield consistent results because the calculated index has a zone of discontinuity (Tarasov and Potvin, 2013). Moreover, both brittle and ductile rocks have either positive or negative values, which would cause misleading results.

Although [6] and [7] use similar concept as the others do, the parameters used in the equations have less potential in misinterpretation because those are less biasedly calculated from the slope of the stress-strain curves. In addition, [6] has a positive value range would be better to indicate the brittleness. Therefore, the [6] was chosen to quantify the rock brittleness with the stress-strain curves and labeled as $BI_{Tarasov}$.

Moreover, based on the availability of the data, 3 additional brittleness indices were selected ([13], [14] and [17]) and are labeled as UCS, $BI_{Hucka\ and\ Das}$ and $BI_{Rickman}$, respectively.

7.3 Brittleness Quantification by Measured Rock Properties

The $BI_{Tarasov}$ is calculated from the Young modulus in the last stage and post-peak modulus (Table 13). As the stress-strain curves show, the N1-4348 specimens have smaller post-peak modulus and lower Young modulus (yellow curves in *Figure 29*). Consequently, the calculated $BI_{Tarasov}$ values are higher than the others (21.07-61.12). In addition, the $BI_{Tarasov}$ of the Middle East carbonate #2 is 52.29 as the specimen has a small post-peak modulus. Otherwise, the calculated $BI_{Tarasov}$ values are in the range of 1.61-10.57 (Table 14).

The UCS values are varied from 48.02 to 212.17 MPa. Similar to the $BI_{Tarasov}$, the UCS values are lower for the N1-4348 specimens (68.37, 48.02 and 77.69 MPa), while the others are in the range of 101.11-212.17 MPa (Table 14). Meanwhile, the UCS of N2-4219.5-2H and Mancos #1 are relatively low (75.27 and 85.79 MPa).

The $BI_{Hucka\ and\ Das}$ is calculated by a simple formula, sine of IFA. In our case, the specimens with the small post-peak modulus have lower IFA values (less than 23.73°). In spite of its large post-peak modulus values, 2 specimens, N2-4219.5-2H and N2-4281-3V, showed low IFA values (29.25° and 21.30°, respectively). As described in section 5.4.2, failure on the 2 specimens caused the volume shrinkage (positive final volumetric strain) which implies that the macro natural fracture and the macro vesicles might have collapsed by compressive stress. Due to this void collapse phenomenon, it appears that the confining pressure does not effectively support the strength of the 2 specimens and thus the IFA values of the specimens are low.

Based on the Young modulus and Poisson's ratio, the $BI_{Rickman}$ was calculated for each specimen (Table 14). Instead of using the converted parameters from the dynamic properties, the static properties measured during the laboratory testing were used without manipulation. The index varied widely with range 14.72 - 59.47.

Table 13. Measured Young modulus, Poisson's ratio, post-peak modulus and IFA.

Specimen ID	Young modulus, GPa	Poisson's ratio	Post-peak modulus, GPa	IFA, °
N1-4013-1H	27.21	0.42	-38.14	45.83
N1-4013-1V	28.20	0.39	N/A	34.01
N2-4219.5-2H	20.03	0.20	-16.60	29.25
N2-4281-3V	45.01	0.30	-73.45	21.30
Oxy-4394.5-1V	57.42	0.37	-12.36	29.71
Oxy-4394.5-5V	46.36	0.41	-60.39	40.25
Oxy-4394.5-6V	39.89	0.33	-54.30	N/A
N1-4348-2H	16.57	0.28	-0.83	23.73
N1-4348-2V	13.38	0.36	N/A	19.29
N1-4348-3V	13.99	0.22	-0.23	N/A
N1-4348-4V	13.77	0.31	-0.24	15.61
Mancos Shale #1	24.97	0.34	N/A	28.00
Mancos Shale #2	17.68	0.33	-22.89	43.60
ME carbonate #1	29.69	0.32	-3.10	N/A
ME carbonate #2	35.90	0.31	-0.70	N/A

Table 14. $BI_{Tarasov}$, UCS, $BI_{Hucka\ and\ Das}$ and $BI_{Rickman}$.

ID	$BI_{Tarasov}$	UCS, MPa	$BI_{Hucka\ and\ Das}$	$BI_{Rickman}$
N1-4013-1H	1.71	121.90	0.72	17.04
N1-4013-1V	N/A	122.37	0.56	23.04
N2-4219.5-2H	2.21	75.27	0.49	53.60
N2-4281-3V	1.61	179.52	0.36	59.47
Oxy-4394.5-1V	5.65	212.17	0.50	58.33
Oxy-4394.5-5V	1.77	122.13	0.65	38.87
Oxy-4394.5-6V	1.73	N/A	N/A	48.17
N1-4348-2H	21.07	68.37	0.40	34.02
N1-4348-2V	N/A	48.02	0.33	14.72
N1-4348-3V	61.12	N/A	N/A	43.35
N1-4348-4V	59.29	77.69	0.27	25.11
Mancos Shale #1	N/A	85.79	0.47	31.12
Mancos Shale #2	1.77	101.11	0.48	24.26
ME carbonate #1	10.57	N/A	N/A	39.95
ME carbonate #2	52.29	N/A	N/A	47.67

8. RESULTS OF PERMEABILITY ENHANCEMENT OF ROCK BY FAILURE*

The primary objective of the hydraulic fracture is to enhance the productivity of the reservoir by creating the high conductive fractures. In a reservoir engineering point of view, not only is how much area can be stimulated by the induced fracture important, but how much permeability enhancement can be achieved is also interested.

In this section, the rock permeability before and after failure is measured. Based on the characteristic time ratio, the permeability enhancement ratio will be addressed.

8.1 Experimental Apparatus and Procedures

Before and after the compression test, the permeability of the specimens was measured using the pulse decay permeameter proposed by Brace et al. (1968) (Figure 41). The rock specimen is completely dried prior to saturation with argon gas at the desired pore pressure for 2-3 days. Then a small pressure pulse of 0.3-0.5 MPa located at the upstream volume starts to flow as the test begins. The pressure behavior at the top and the bottom of the specimen is continuously recorded during the test, until the pressure is completely stabilized. The permeability value is calculated by analyzing the dynamic pressure difference between the upstream and downstream.

---

* Reprinted with permission from "Laboratory scale characterization of brittleness and permeability enhancement due to rock failure." by Jihoon Wang, Peter Valko and Ahmad Ghassemi, accepted for publication in forthcoming issue of *International Journal of Oil, Gas and Coal Technology*.

Figure 41. Pulse decay permeability measurement device.

8.2 Characteristic Time

In the section 4, we have seen that the equivalent permeability can be effectively measured using the characteristic time during the pulse decay permeability measurement, even if the rock specimen contains a heterogeneity. In this section, we will see the characteristic time is a reliable factor representing the transport property of rock. If the testing system and pore pressure are consistent, the characteristic time can be used to determine the permeability alteration.

The upstream and downstream pressure behavior in the homogeneous rock specimen can be analytically calculated by the equation (4.6).

$$p(x_D, t_D) = p_{pulse} \cdot \sqrt{\frac{1}{1+\beta+\gamma} + 2\sum_{n=1}^{\infty} \frac{e^{-{\alpha_n}^2 t_D}(\cos(\alpha_n x_D) - \frac{\alpha_n \gamma}{\beta}\sin(\alpha_n x_D))}{(1+\gamma+\beta-\frac{{\alpha_n}^2\gamma}{\beta})\cos(\alpha_n) - \alpha_n(1+\gamma+2\gamma/\beta)\sin(\alpha_n)}} \quad (4.6)$$

As can be seen in the analytical solution, the pressure behavior during the pulse decay permeability measurement test only depends on the variables α_n, β and γ given by,

$$\alpha_n\beta(\gamma+1)\cos(\alpha_n) + (\beta^2 - {\alpha_n}^2\gamma)\sin(\alpha_n) = 0 \quad (4.7)$$

$$\beta = \frac{\phi V_s}{V_u} \tag{4.8}$$

$$\gamma = \frac{V_d}{V_u} \tag{4.9}$$

Therefore, if the testing system is identical, i.e. upstream and downstream volume are consistent and the porosity is assumed negligible, the characteristic time is always achieved at the same t_D.

$$t_D = \frac{kt}{\phi \mu c_g L^2} \tag{4.11}$$

Managing the testing condition consistently, the characteristic time only depends on the permeability and porosity. Since it is not possible to measure the precise volume of the specimen after failure, the porosity and the length of the specimen are assumed to be constant.

Then the permeability enhancement is given by

$$ke = \frac{k_{post}}{k_{pre}} = \frac{t_{ch,pre}}{t_{ch,post}} \tag{8.1}$$

Therefore, the permeability enhancement ratio due to failure k_{post}/k_{pre} can be directly obtained from the characteristic time ratio, $t_{ch,pre}/t_{ch,post}$.

Figure 42 shows the pressure behaviors at the upstream and downstream of N1-4013-1V specimen before and after failure. The characteristic time of pre-failure state of the rock is 2640.11 seconds, which is much longer than that of the post-failure state, 68.40 seconds. As a result, the permeability enhancement ratio of the rock specimen is 38.60.

In addition, the characteristic time can be also effectively applied to the stress dependent permeability measurement. If the effective confining pressure is only controlled by the confining pressure, i.e. with constant pore pressure, the stress dependent permeability can be calculated with the characteristic time ratio.

$$\frac{k}{k_0} = \frac{t_{ch\,0}}{t_{ch}} \tag{8.2}$$

where, k_0 and $t_{ch\,0}$ are the permeability and the characteristic time of the reference condition.

The stress dependent permeability test was performed on the N2-4281-3V specimen with the constant pore pressure of 3.9 MPa. As shown in the Figure 43, the characteristic time increases with the confining pressure. The condition and the measured characteristic time are shown in Table 15.

Table 15. Testing condition and measured characteristic time during the stress dependent permeability test on N2-4281-3V specimen.

Confining Pressure, MPa	Effective Pressure, MPa	Characteristic Time, sec
7.99	4.08	29.27
8.94	5.02	33.53
10.02	6.10	40.64
12.10	8.18	71.09
13.45	9.53	130.36
15.24	11.33	608.47

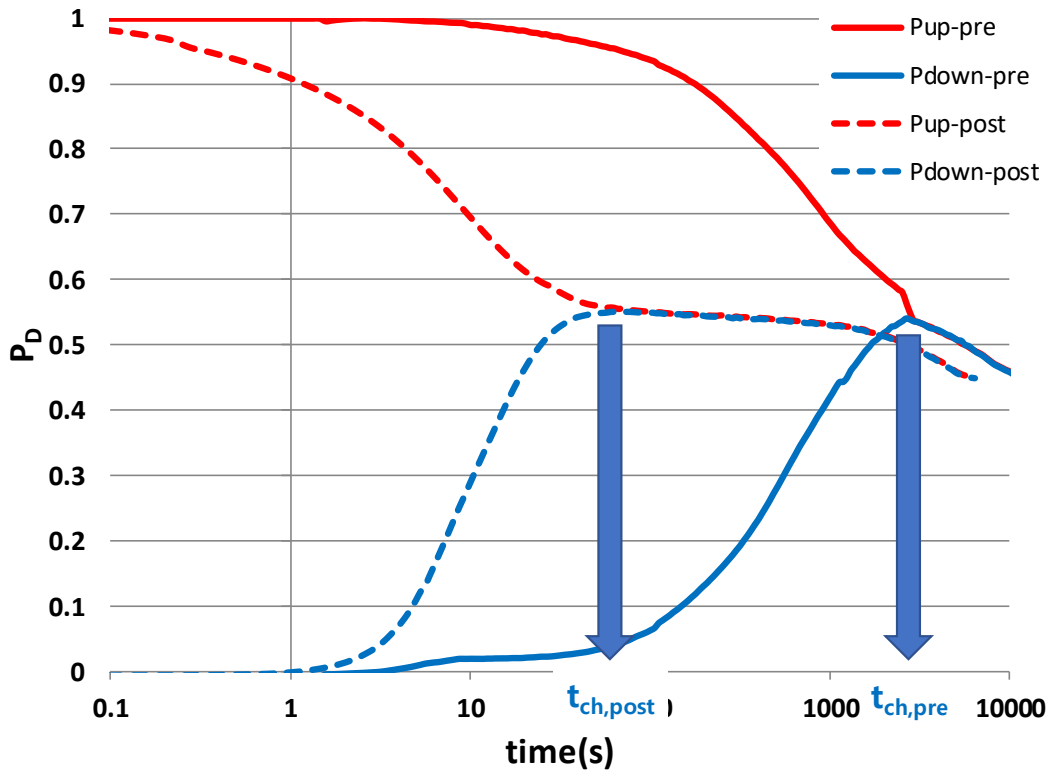

Figure 42. Pressure behavior at the upstream and downstream during pressure pulse permeability measurement. Characteristic times before failure ($t_{ch,pre}$) is 2640.11 seconds and after failure ($t_{ch,post}$) is 68.40 seconds.

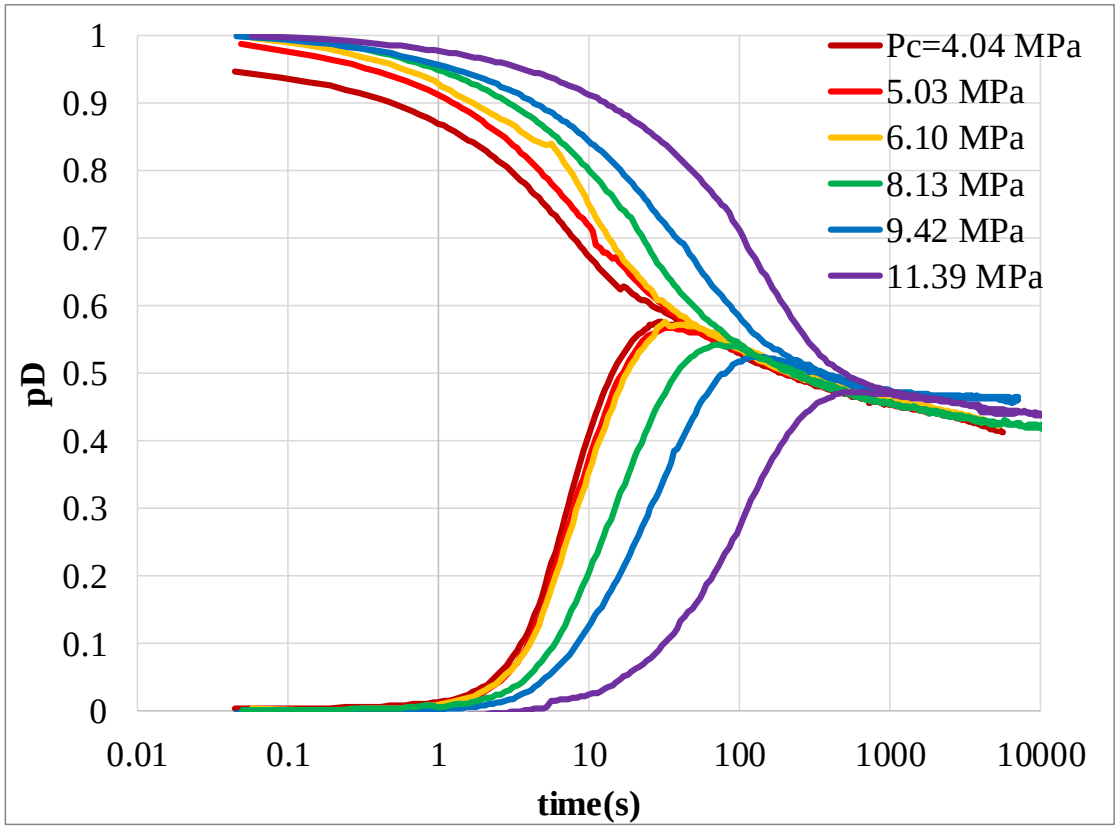

Figure 43. Pressure behavior during stress dependent permeability measurement on N2-4281-3V specimen.

8.3 Permeability Enhancement by Failure

As seen in the previous section, the characteristic time can be used to calculate the permeability enhancement ratio before and after failure. In order to make the assumptions valid, the upstream and downstream volumes are maintained same and the pore pressure of each specimen was constant. The effective confining pressure before and after failure is maintained as consistent as possible (Table 16).

Even though the results show that the permeabilities of all the specimens enhanced by failure, the values vary in very wide range (1.02-954.54). Based on the magnitudes of the permeability enhancement ratio, the tested rock specimens can be categorized into 2 groups.

In one group, the permeability enhancement ratio is at least two orders of magnitude or more. As anticipated, the first group consists of the specimens with the low post-peak modulus, based on the behavior of the stress-strain curve. It is expected that the sudden drop of the sustained stress induced micro fractures and effectively increased the permeability of the sample. In this respect, sample Oxy-4394.5-5V responded the most “positively” to the load causing failure. It is possible that natural fractures contained in the specimens, that had been completely cemented with secondary minerals (Figure 27), “re-opened”, but it is also possible that the micro fractures evolved completely during the test itself.

The other group showed moderate permeability enhancement ratio (less than one order of magnitude). As anticipated, the specimens belong to this group have small post-peak modulus, based on the post-peak behavior on the strain-stress curves.

In addition, it is found that there are 2 specimens showing sudden stress drop at failure indicate the low perm enhancement ratio (N2-4219.5-2H and N2-4281-3V). This is caused by the volume shrinkage of the specimens which deteriorates the fluid transport ability by flow path blockage. As shown in Figure 26 and as described in 5.4.2, the macro void space detected from the CT scanned images could have been collapsed. In addition, the N1-4348-3V, which shows both the post-peak modulus of -0.23 and the volume shrinkage. As a result, the characteristic time of N1-4348-3V increased only by 2 % due to failure.

Table 16. Effective confining pressure condition for the permeability measurement test.

Core ID	Before or after failure	Effective Confining pressure, MPa	Characteristic Time, s	Characteristic Time ratio (before/after)
N1-4013-1H	Before	6.77	134. 54	21.49
	After	4.85	6.21	
N1-4013-1V	Before	5.01	2,640.11	38.60
	After	4.69	68.40	
N2-4219.5-2H	Before	5.83	29.68	4.47
	After	5.56	6.65	
N2-4281-3V	Before	4.04	41.76	3.11
	After	3.94	13.41	
Oxy-4394.5-1V	Before	3.61	7,318.89	2.42
	After	3.73	3,028.55	
Oxy-4394.5-5V	Before	4.69	8,275.83	954.54
	After	4.79	8.67	
Oxy-4394.5-6V	Before	6.02	11,514.35	408.93
	After	6.80	28.16	
N1-4348-2H	Before	4.78	61.88	3.32
	After	5.83	18.65	
N1-4348-2V	Before	6.16	35.56	2.00
	After	6.70	17.76	
N1-4348-3V	Before	7.14	102.33	1.02
	After	6.88	100.24	
N1-4348-4V	Before	6.34	18.37	1.45
	After	6.26	12.63	
Mancos shale #1	Before	6.92	8629.27	9.87
	After	6.19	874.18	
Mancos shale #2	Before	6.06	3236.70	15.54
	After	6.03	208.30	
ME carbonate #1	Before	6.00	1937.68	11.50
	After	5.71	168.48	
ME carbonate #2	Before	7.29	30.95	2.80
	After	6.93	11.07	

8.4 Summary

In this section, the permeability of the rock specimens was measured before and after failure. According to the analytical solution of the pressure behavior during the pulse decay permeability measurement, the characteristic time ratio can be reliably used for the permeability enhancement ratio determination if the testing system and condition are consistent. Moreover, the stress dependent permeability test can be performed more effectively with the characteristic time approach.

According to the results of the permeability enhancement, the ratio relies on 3 characteristics of the rock. The first thing is the existence of the natural fracture, which would be reactivated and be opened by failure to create additional flow paths. It appears that the non-dilatancy has a negative effect on the permeability enhancement. Moreover, the post-peak behavior on the stress-strain curve can be an indicator of the permeability enhancement.

9. RELATIONSHIP BETWEEN THE BRITTLENESS INDICES AND PERMEABILITY ENHANCEMENT*

When dealing with unconventional resources, the major goal of brittleness quantification is to predict the formation response to hydraulic fracturing, or - simply put - to predict the achievable productivity. While such a prediction depends on many factors involving well spacing, fracture spacing, amounts of proppant and fluid used, pumping schedules and so forth, some aspects of the achievable productivity are directly related to an observable quantity on the laboratory scale. We will call this quantity the permeability enhancement ratio due to rock failure. It is anticipated that more brittle rocks show more profound permeability enhancement ratio measured by the ratio of characteristic times of pulse permeability measurement before and after rock failure.

In this section, we consider the relation between quantified brittleness indices above with the observed characteristic time ratios. We emphasize that the various brittleness indices and the permeability enhancement ratios were determined from observations on the same rock specimen.

* Reprinted with permission from "Laboratory scale characterization of brittleness and permeability enhancement due to rock failure." by Jihoon Wang, Peter Valko and Ahmad Ghassemi, accepted for publication in forthcoming issue of *International Journal of Oil, Gas and Coal Technology*.

9.1 $BI_{Tarasov}$

The $BI_{Tarasov}$ is calculated by the unloading (Young) modulus and the post-peak modulus. Since the post-peak modulus is negative, the rock with complete brittleness has a value of 1.

$$BI_{Tarasov} = \frac{dW_r}{dW_e} = \frac{M - E}{M} = 1 - \frac{\mathrm{E}}{\mathrm{M}} \tag{7.6}$$

Unlike the conventional notion, the strong brittleness can be achieved when the rock has low Young modulus and rapid stress drop after peak.

Figure 44 shows the Young modulus, post-peak modulus and $BI_{Tarasov}$ versus characteristic time ratio. Since the volume shrinkage during the test would deteriorate the permeability enhancement, the rocks with the volume shrinkage are marked in red. As shown in Figure 44 (a), the Young modulus shows a linear relationship with the permeability enhancement on the semi-log scale, except 3 specimens. Similarly, the post-peak modulus has also a linear trend, except 1 specimen with the volume shrinkage. In opposition to the main assumption, the permeability enhancement is higher for the higher Young modulus. Meanwhile, the post-peak modulus shows an accordance result as it shows better permeability enhancement for the low post-peak modulus.

According to the relationship between $BI_{Tarasov}$ and the characteristic time ratio, the specimens with higher brittleness showed more favorable permeability enhancement (Figure 44 (c)). The specimens with higher than 20 of the $BI_{Tarasov}$ showed only 1 order

of magnitude permeability enhancement. Consequently, the $BI_{Tarasov}$ quantifying the rock brittleness from the stress-strain curves can be used as the permeability enhancement predictor with extra care taken for the possibility of volume shrinkage. However, using the index solely to predict the permeability enhancement is not suitable because the permeability enhancement ratio values are very scattered for the rocks with strong brittleness. In our case, the dilatant specimens with $BI_{Tarasov}$ less than 2 have a wide range of the characteristic time ratio (15.54 - 954.54).

Table 17. Young modulus, post-peak modulus, $BI_{Tarasov}$ and characteristic time ratio

ID	Young modulus, GPa	Post-peak modulus, GPa	$BI_{Tarasov}$	Characteristic Time ratio (before/after)
N1-4013-1H	27.21	-38.14	1.71	21.49
N1-4013-1V	28.20	N/A	N/A	38.60
N2-4219.5-2H	20.03	-16.60	2.21	4.47
N2-4281-3V	45.01	-73.45	1.61	3.11
Oxy-4394.5-1V	57.42	-12.36	5.65	2.42
Oxy-4394.5-5V	46.36	-60.39	1.77	954.54
Oxy-4394.5-6V	39.89	-54.30	1.73	408.93
N1-4348-2H	16.57	-0.83	21.07	3.32
N1-4348-2V	13.38	N/A	N/A	2.00
N1-4348-3V	13.99	-0.23	61.12	1.02
N1-4348-4V	13.77	-0.24	59.29	1.45
Mancos #1	24.97	N/A	N/A	9.87
Mancos #2	17.68	-22.89	1.77	15.54
ME carbonate #1	29.69	-3.10	10.57	11.50
ME carbonate #2	35.90	-0.70	52.29	2.80

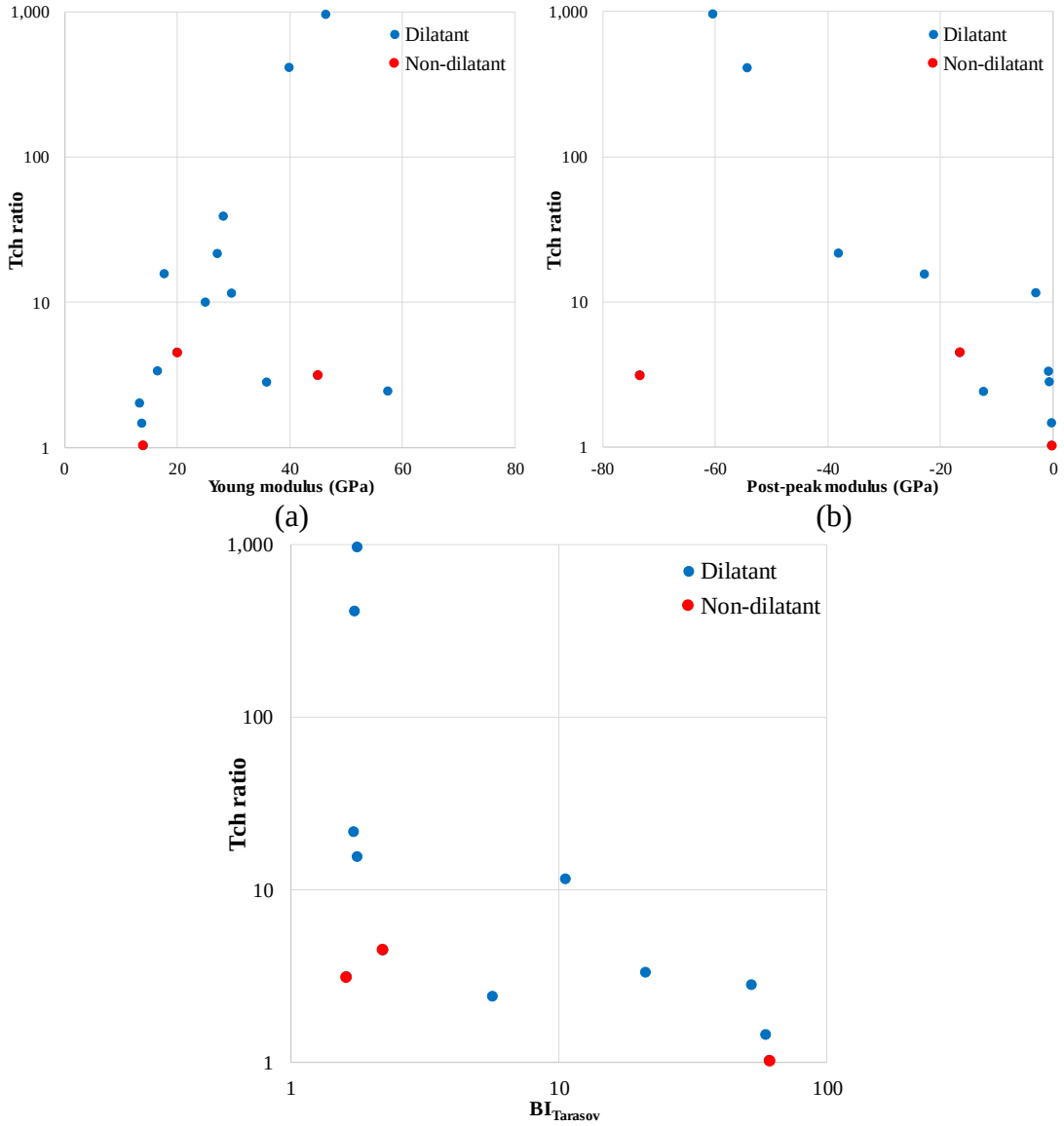

Figure 44. Characteristic time ratio versus (a) Young modulus, (b) post-peak modulus and (c) $BI_{Tarasov}$.

9.2 Unconfined Compressive Strength

In general, rock with high strength is thought to be more brittle because the high stress level at failure will effectively generate and propagate the fracture. The relationship of the permeability enhancement and the rock strength was investigated with UCS. As shown in Figure 45, the characteristic time ratio increases with the UCS except 2 specimens.

In addition to the non-dilatant N2-4281-3V specimen, the Oxy-4394.5-1V showed less favorable permeability enhancement, although it had very high UCS (Table 18).

Table 18. UCS and characteristic time ratio

ID	UCS, MPa	Characteristic Time ratio (before/after)
N1-4013-1H	121.90	21.49
N1-4013-1V	122.37	38.60
N2-4219.5-2H	75.27	4.47
N2-4281-3V	179.52	3.11
Oxy-4394.5-1V	212.17	2.42
Oxy-4394.5-5V	122.13	954.54
Oxy-4394.5-6V	N/A	408.93
N1-4348-2H	68.37	3.32
N1-4348-2V	48.02	2.00
N1-4348-3V	N/A	1.02
N1-4348-4V	77.69	1.45
Mancos #1	85.79	9.87
Mancos #2	101.11	15.54
ME carbonate #1	N/A	11.50
ME carbonate #2	N/A	2.80

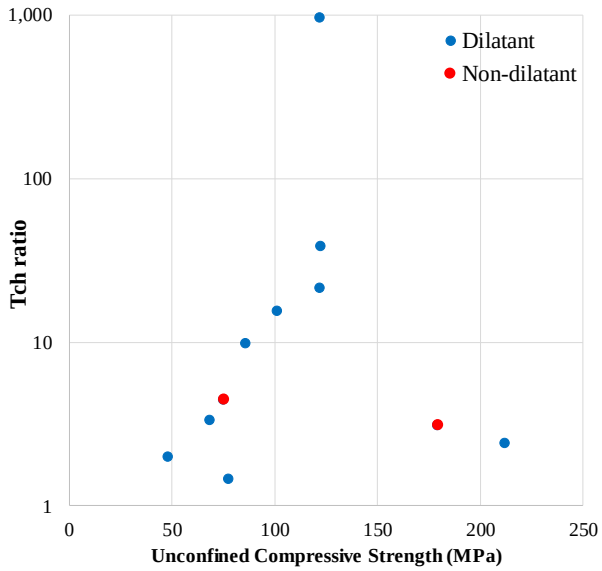

Figure 45. Characteristic time ratio versus Unconfined Compressive Strength.

9.3 $BI_{\text{Hucka and Das}}$

Since IFA describes the strength increment by depth, it is a crucial parameter in geomechanical analysis of reservoirs. Hucka and Das (1974) proposed a simple formula based on the idea that brittle rocks have higher IFA than ductile rocks.

$$BI_{Hucka\ and\ Das} = \sin(IFA) \tag{7.14}$$

The IFA and $BI_{\text{Hucka and Das}}$ are shown with the characteristic time ratio as shown in Table 19 and Figure 46. The index favorably represents the permeability enhancement,

including the volume shrinkage rocks marked in red. This is because the $BI_{Hucka\ and\ Das}$ are in accordance with the 3 characteristics of rocks for favorable permeability enhancement as described in section 8.3.

Firstly, the rock specimens with the small post-peak modulus have low IFA. It is expected that the confining pressure increment does not effectively strengthen these rocks.

The IFA values are higher if vertical natural fracture exists and the fracture is re-opened during the failure which in turn - improves the permeability. As shown in Figure 25, the N-4013-1H contained a vertical natural fracture and had a higher IFA (45.8°) than the 1V which contained a lateral natural fracture (34.0°). Since the confinement pressurizes the cylinder-shape rock radially, the shear strength increment with the confinement is higher for the specimen with vertical discontinuity. For the Oxy-4395-5V specimen, which contained a natural vertical fracture before testing, had higher IFA than the 1V (40.3° and 29.7°, respectively)

In addition, the volume shrunk specimens N2-4219.5-2H and N2-4281-3V showed the lowest IFA values among the brittle specimens (29.2° and 21.3°, respectively). Therefore, the same mechanism decreased the rock strength with the confinement and the permeability.

Consequently, it appears that the $BI_{Hucka\ and\ Das}$ calculated from the IFA depends on 3 characteristics affecting the permeability enhancement, existence and direction of the natural fracture and the volume shrinkage by void collapse.

Table 19. IFA, $BI_{Hucka\ and\ Das}$ and characteristic time ratio

ID	IFA, °	$BI_{Hucka\ and\ Das}$	Characteristic Time ratio (before/after)
N1-4013-1H	45.83	0.72	21.49
N1-4013-1V	34.01	0.56	38.60
N2-4219.5-2H	29.25	0.49	4.47
N2-4281-3V	21.30	0.36	3.11
Oxy-4394.5-1V	29.71	0.50	2.42
Oxy-4394.5-5V	40.25	0.65	954.54
Oxy-4394.5-6V	N/A	N/A	408.93
N1-4348-2H	23.73	0.40	3.32
N1-4348-2V	19.29	0.33	2.00
N1-4348-3V	N/A	N/A	1.02
N1-4348-4V	15.61	0.27	1.45
Mancos #1	28.00	0.47	9.87
Mancos #2	28.90	0.48	15.54
ME carbonate #1	N/A	N/A	11.50
ME carbonate #2	N/A	N/A	2.80

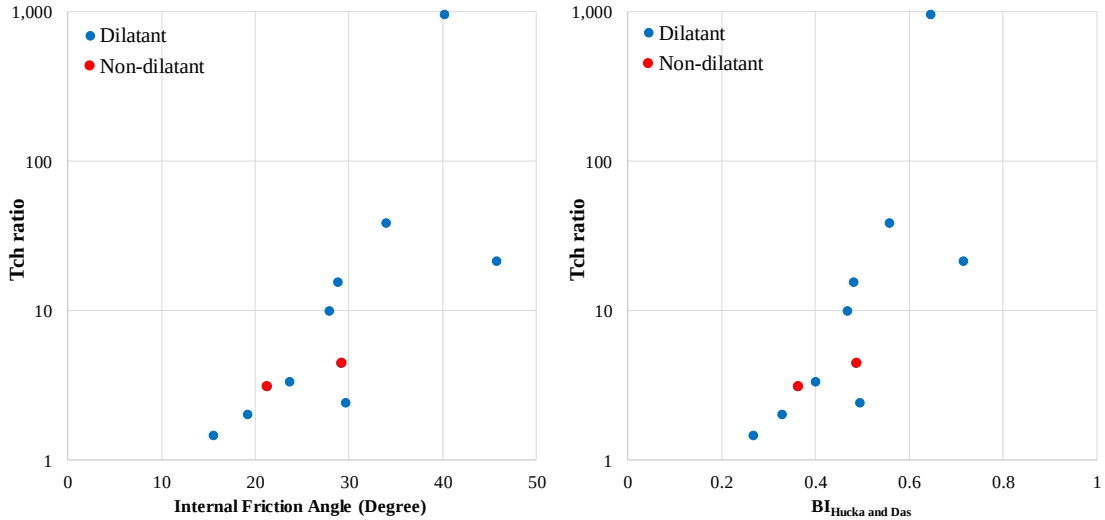

Figure 46. Characteristic time ratio versus (a) Internal Friction Angle and (b) $BI_{\text{Hucka and Das}}$.

9.4 BI_{Rickman}

The brittleness index proposed by Rickman et al. (2008) is the most widely used method due to the fact that the basic elasticity parameters needed are usually available from logs. The main assumption is that the brittle rocks have higher Young modulus and lower Poisson's ratio.

$$BI_{Rickman} = \frac{E_B + \nu_B}{2} \tag{7.17}$$

where, E_B and ν_B are given by

$$E_B = \frac{E - 1}{8 - 1} \times 100 \tag{7.18}$$

$$\nu_B = \frac{\nu - 0.4}{0.15 - 0.4} \times 100 \tag{7.19}$$

The calculated $BI_{Rickman}$ values are shown in Table 20 with the corresponding elastic properties obtained directly from the multi-stage triaxial test. It seems that the Young modulus values are well matched with the characteristic time ratio except for a few specimens, but the Poisson's ratio does not seem to have any relation with permeability enhancement (Figure 47 (a) and (b)). Although the authors suggested that the Poisson's ratio would represent the rocks ability to fail under stress, the low Poisson's ratio would also indicate the non-dilatancy which negatively affect the permeability enhancement by failure. Consequently, it appears that the $BI_{Rickman}$ does not correlate well with the permeability enhancement on the lab scale (Figure 47). Based on our experience, this index should not be used to predict permeability enhancement due to failure.

Table 20. Young modulus, Poisson's ratio, $BI_{Rickman}$ and characteristic time ratio

ID	Young modulus, GPa	Poisson's ratio	$BI_{Rickman}$	Characteristic Time ratio (before/after)
N1-4013-1H	27.21	0.42	17.04	21.49
N1-4013-1V	28.20	0.39	23.04	38.60
N2-4219.5-2H	20.03	0.20	53.60	4.47
N2-4281-3V	45.01	0.30	59.47	3.11
Oxy-4394.5-1V	57.42	0.37	58.33	2.42
Oxy-4394.5-5V	46.36	0.41	38.87	954.54
Oxy-4394.5-6V	39.89	0.33	48.17	408.93
N1-4348-2H	16.57	0.28	34.02	3.32
N1-4348-2V	13.38	0.36	14.72	2.00
N1-4348-3V	13.99	0.22	43.35	1.02
N1-4348-4V	13.77	0.31	25.11	1.45
Mancos #1	24.97	0.34	31.12	9.87
Mancos #2	17.68	0.33	24.26	15.54
ME carbonate #1	29.69	0.32	39.95	11.50
ME carbonate #2	35.90	0.31	47.67	2.80

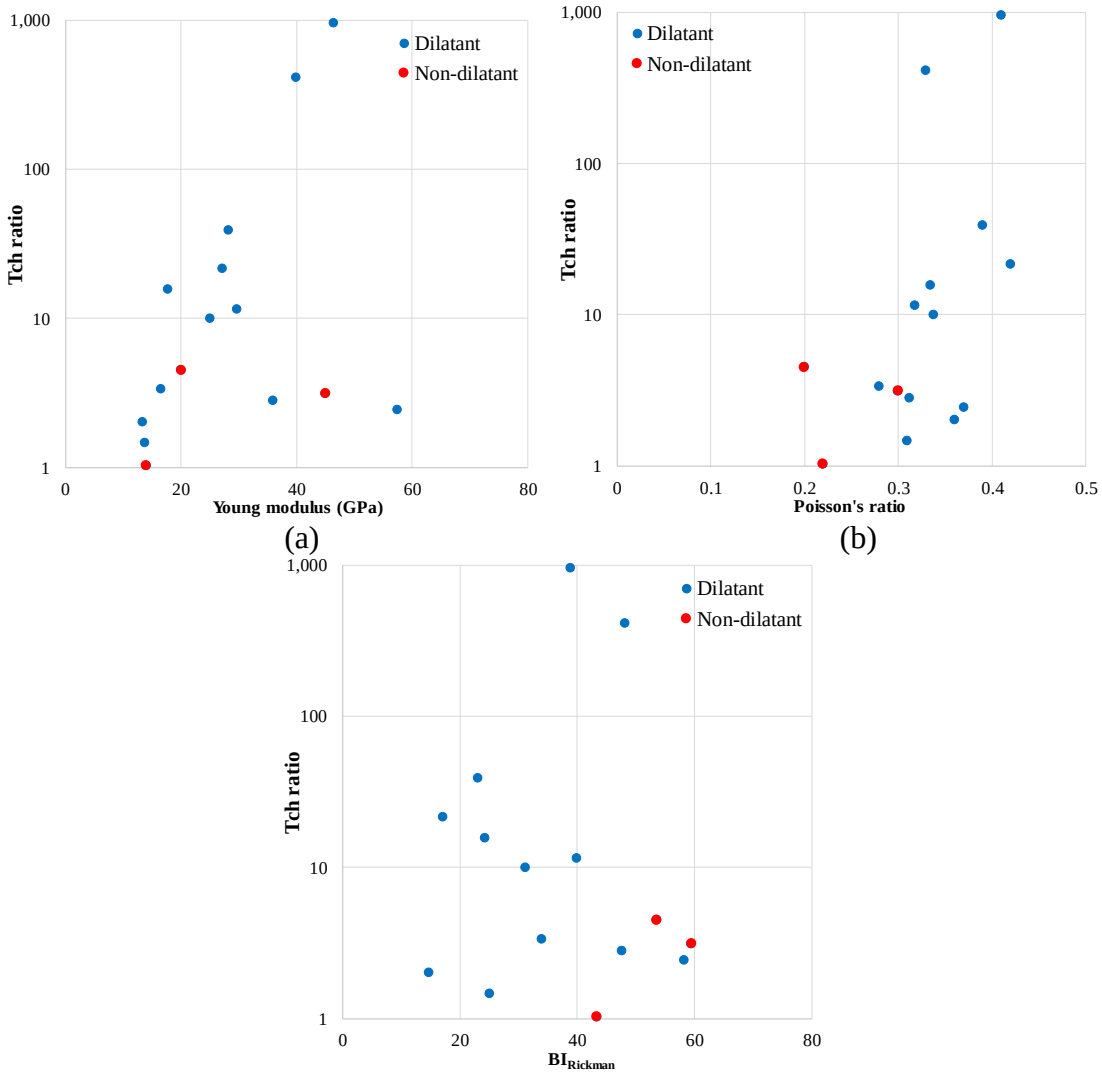

Figure 47. Characteristic time ratio versus (a) Young modulus, (b) Poisson's ratio and (c) $BI_{Rickman}$.

9.5 Summary

In this section, the predictability of the selected brittleness indices on the permeability enhancement was investigated. It was found that the $BI_{Tarasov}$ quantified from the rock stiffness and post-peak behavior is a good predictor of permeability enhancement due to rock failure, if volume shrinkage does not occur. Another index, the $BI_{Hucka\ and\ Das}$, which is calculated from the IFA can be used as a reliable predictor, because being also affected by natural fracture and volume shrinkage, it varies monotonically with the permeability enhancement ratio.

Consequently, it is found that the $BI_{Tarasov}$ and the $BI_{Hucka\ and\ Das}$ represent the dominant factors of the permeability enhancement due to rock failure. Applying both indices would be more predictive to characterize the *potential* permeability enhancement achievable in the stimulated reservoir volume created by a hydraulic fracturing treatment.

10. CONCLUSIONS AND RECOMMENDATIONS

In this study, the practical applicability of the rock brittleness index as a predictor of laboratory-scale permeability enhancement due to failure was investigated. The conclusion and the recommendation for the future work will be addressed in this section.

10.1 Conclusion

Characterizing the unconventional reservoir is very challenging even in the lab scale. This is mainly caused by the complex pore structure and the heterogeneous characteristics of the rocks. In order to overcome the difficulties, a number of researches attempted to modify the conventional methods or to suggest new methods for measuring rock properties. In this study, the multistage triaxial testing method and the pulse decay permeability measurement method were selected and adopted.

The conventional analysis of the pulse permeability measurement was performed by the analytical solutions with the assumption that the rock specimen is homogeneous. Since the transport property of rock strongly depends on the heterogeneity, especially the nonuniformly distributed fractures, it is necessary to take into account the heterogeneity effect to obtain reliable results. Therefore, the pressure behavior during the measurement was modeled using the Finite Element Method utilizing various assumptions on the structure of heterogeneity. As a result, it was found that the heterogeneity yields distinctive pressure behavior at both the upstream and downstream vessels. However, the

characteristic time of the heterogeneous specimen is basically identical with the homogeneous specimen of the same equivalent permeability. Therefore, reliable permeability enhancement ratios can be obtained by comparing characteristic times even if the rock specimen contains unexpected heterogeneity. During further analysis of the analytical solution, we found that the characteristic time can be used as a useful tool in permeability alteration measurement, if the testing system and conditions are maintained consistently. With the mathematical approach and experimental examples, we have seen this is valid for the measurement of the permeability enhancement by failure and for characterization of stress dependent permeability.

The success of rock property measurement with the multistage triaxial testing method depends on the careful selection of the stopping point at each confining pressure stage. We found the zero volumetric strain as a suitable condition for stopping the individual stages. For the non-dilatant specimens, the stress-strain behavior was closely monitored to stop the loading when the nonlinear axial response could be observed.

It was found that the measured rock properties are affected by the rock characteristics, such as post-peak behavior, non-dilatancy and existing natural fractures. Especially, the IFA values reflect the small post-peak modulus, non-dilatancy and vertical natural fracture. Since IFA describes the strength increment by the confining pressure, the low IFA values for the non-dilatant rocks indicate they are not confined effectively to increase the strength.

19 brittleness indices were reviewed and analyzed. Based on the availability of the measured data and the consistency of the calculated value, 4 indices were selected.

The calculated brittleness indices were integrated with the permeability enhancement ratio. The results show that the permeability enhancement ratio depends on the post-peak behavior, dilatancy and the existence and direction of natural fracture. Consequently, it was found that the $BI_{Tarasov}$ and the $BI_{Hucka\ and\ Das}$ showed good agreement with the permeability enhancement. Moreover, UCS can estimate the permeability enhancement with few exceptions. However, there was no specific relationship found between the $BI_{Rickman}$ and the permeability enhancement. This is because the low Poisson's ratio may imply the non-dilatancy of the rock, in opposition to the basic concept of the index.

10.2 Recommendations for Further Research

The primary idea of the multistage triaxial test is to gather the rock properties under multiple conditions with specific stopping points. For dilatant rocks, the stopping points can be determined by analyzing the local Poisson's ratio and the volumetric strain behaviors. However, the stopping point selection for non-dilatant rocks suggested in this study contains uncertainty because the 2% threshold for the change in the local Young modulus is somewhat arbitrary. In order to avoid the irreversible deformation, a micro-seismic sensor can be attached to the triaxial machine. Monitoring the emitted signal from the rock specimen and detecting change in its spectrum can provide a better way to select the stopping point.

In addition, how to extend the results from the lab scale to the field is also a critical question to be answered. For example, IFA values are commonly determined by

correlation in the field scale. However, further research is needed to determine whether the calculated IFA does or does not contain important information regarding the permeability enhancement. The same statement applies to information obtained from measurements while drilling.

The observations found in this study can be applied in a field development study based on reservoir simulation. One can assume that the failed specimens represent the state of the rock near the main propped fracture in the reservoir, and hence the permeability enhancement ratio concept can be used to determine the grid-block permeability in this region. Further research is needed to clarify how to apply the permeability enhancement ratio concept at those locations within the stimulated reservoir volume that fall further from the main hydraulic fracture.

REFERENCES

Altindag, R. (2003) 'Correlation of specific energy with rock brittleness concepts on rock cutting', *The Journal of The South African Institute of Mining and Metallurgy*, Vol.103 No.3, pp.163-172

Bergman, S.G.A. and Stille, H. (1983) 'Rock burst problems in a 2.6 million m^3 underground crude oil storage in granite'. Paper Presented at the *5th International Society for Rock Mechanics Congress*, 10-15 April 1983. Melbourne, Australia.

Brace, W.F., Walsh, J.B. and Frangos, W.T. (1968) 'Permeability of granite under high pressure', *Journal of Geophysical Research*, Vol.73 No.6, pp.2225-2236

Brezovski, R. and Cui, A. (2013) 'Laboratory permeability measurements of unconventional reservoirs: Useless or full of information? A montney example from the western canadian sedimentary basin'. Paper Presented at the *SPE Unconventional Resources Conference and Exhibition-Asia Pacific*, 11-13 November 2013. Brisbane, Australia.

Britt, L.K. and Schoeffler, J. (2009) 'The geomechanics of a shale play: What makes a shale prospective'. Paper Presented at the *SPE Eastern Regional Meeting*, 23-25 September 2009. Charleston, West Virginia, USA.

Chen, Y., Wei, L., Mastalerz, M. and Schimmelmann, A. (2015) 'The effect of analytical particle size on gas adsorption porosimetry of shale', *International Journal of Coal Geology*, Vol.138, pp.103-112

Coates, D.F. and Parsons, R.C. (1966) 'Experimental criteria for classification of rock substances', *International Journal of Rock Mechanics and Mining Sciences* Vol.3 No.3, pp.181-189

Crawford, A.M. and Wylie, D.A. (1987) 'A modified multiple failure state triaxial testing method'. Paper Presented at the *28th U.S. Symposium on Rock Mechanics* 29 June-1 July 1987. Tucsan, Arizona, USA.

Cui, X., Bustin, A.M.M. and Bustin, R.M. (2009) 'Measurements of gas permeability and diffusivity of tight reservoir rocks: Different approaches and their applications', *Geofluids*, Vol.9 No.3, pp.208-223

Dacunha, J.J. (2014) *Solutions and generalizations of partial differential equations occurring in petroleum engineering*. Master of Science, Texas A&M University, College Station, TX, USA.

Dicker, A.I. and Smits, R.M. (1988) 'A practical approach for determining permeability from laboratory pressure-pulse decay measurements'. Paper Presented at the *International Meeting on Petroleum Engineering*, 1-4 November 1988. Tianjin, China.

Feng, R., Liu, J. and Harpalani, S. (2017) 'Optimized pressure pulse-decay method for laboratory estimation of gas permeability of sorptive reservoirs: Part 1 – background and numerical analysis', *Fuel*, Vol.191, pp.555-564

Fischer, G.J. (1992) 'Chapter 8 the determination of permeability and storage capacity: Pore pressure oscillation method', *International Geophysics*, Vol.51, pp.187-211

Fjar, E., Holt, R.M., Raaen, A.M., Risnes, R. and Horsrud, P. (2008) *Petroleum related rock mechanics*, 2nd ed., Elsevier Science, Oxford, UK.

Goodman, R.E. (1989) *Introduction to rock mechanics*, 2nd ed., Wiley, New York, NY, USA.

Hajiabdolmajid, V., Martin, C.D. and Kaiser, P.K. (2000) 'Modelling brittle failure of rock'. Paper Presented at the *4th North American Rock Mechanics Symposium*, 31 July-3 August 2000. Seattle, Washington, USA.

He, C., Okubo, S. and Nishimatsu (1990) 'A study of the class ii behaviour of rock', *Rock Mechanics and Rock Engineering*, Vol.23 No.4, pp.261-273

Heap, M.J., Farquharson, J.I., Baud, P., Lavallée, Y. and Reuschlé, T. (2015) 'Fracture and compaction of andesite in a volcanic edifice', *Bulletin of Volcanology*, Vol.77 No.6, pp.55

Hucka, V. and Das, B. (1974) 'Brittleness determination of rocks by different methods', *International Journal of Rock Mechanics and Mining Sciences & Geomechanics Abstracts*, Vol.11 No.10, pp.389-392

Islam, M.A. and Skalle, P. (2013) 'An experimental investigation of shale mechanical properties through drained and undrained test mechanisms', *Rock Mechanics and Rock Engineering*, Vol.46 No.6, pp.1391-1413

Jarvie, D.M., Hill, R.J., Ruble, T.E. and Pollastro, R.M. (2007) 'Unconventional shale-gas systems: The mississippian barnett shale of north-central texas as one model for thermogenic shale-gas assessment', *American Association of Petroleum Geologists Bulletin*, Vol.91 No.4, pp.475-499

Josh, M., Esteban, L., Delle Piane, C., Sarout, J., Dewhurst, D.N. and Clennell, M.B. (2012) 'Laboratory characterisation of shale properties', *Journal of Petroleum Science and Engineering*, Vol.88, pp.107-124

Kamath, J., Boyer, R.E. and Nakagawa, F.M. (1992) 'Characterization of core scale heterogeneities using laboratory pressure transients', *SPE Formation Evaluation*, Vol.7 No.3, pp.219-227

Kirschbaum, M.A. (2003) Geologic assessment of undiscovered oil and gas resources of the mancos/mowry total petroleum system, uinta-piceance province, utah and colorado, U.S. Geological Survey, Denver, CO, USA.

Kovaleva, G.A. (1974) 'Mechanical properties of the principal rock-forming minerals of the khibiny apatite — nepheline deposits', *Soviet Mining*, Vol.10 No.5, pp.533-537

Kovári, K. and Tisa, A. (1975) 'Multiple failure state and strain controlled triaxial tests', *Rock Mechanics and Rock Engineering*, Vol.7 No.1, pp.17-33

Kovari, K., TISA, A., Einstein, H.H. and Franklin, J.A. (1983) 'Suggested methods for determining the strength of rock materials in triaxial compression: Revised version', *International Journal of Rock Mechanics and Mining Sciences & Geomechanics Abstracts*, Vol.20 No.6, pp.285-290

Kranz, R.L., Saltzman, J.S. and Blacic, J.D. (1990) 'Hydraulic diffusivity measurements on laboratory rock samples using an oscillating pore pressure method', *International Journal of Rock Mechanics and Mining Sciences & Geomechanics Abstracts*, Vol.27 No.5, pp.345-352

Labuz, J.F. and Zang, A. (2012) 'Mohr–coulomb failure criterion', *Rock Mechanics and Rock Engineering*, Vol.45 No.6, pp.975-979

Lin, C., Pirie, G. and Trimmer, D.A. (1986) 'Low permeability rocks: Laboratory measurements and three-dimensional microstructural analysis', *Journal of Geophysical Research: Solid Earth*, Vol.91 No.B2, pp.2173-2181

Luffel, D.L. and Guidry, F.K. (1992) 'New core analysis methods for measuring reservoir rock properties of devonian shale', *Journal of Petroleum Technology*, Vol.44 No.11, pp.1184-1190

Ning, X., Fan, J., Holditch, S.A. and Lee, W.J. (1993) 'The measurement of matrix and fracture properties in naturally fractured cores'. Paper Presented at the *Society of Petroleum Engineers Rocky Mountain Regional/Low Permeability Reservoirs Symposium*, 26-28 April 1993. Denver, Colorado, USA.

Pagoulatos, A. (2004) *Evaluation of multistage triaxial testing on berea sandstone*. MS Thesis, University of Oklahoma, Norman, Oklahoma, USA.

Prasad, U., Maharidge, R., Franquet, J., Moronkeji, D., Curry, D.A. and Davis, B.J. (2015) 'Shale rock mechanical characteristics: Integration and validation using crossplots'. Paper Presented at the *13th ISRM International Congress of Rock Mechanics*, 10-13 May 2015. Montreal, Canada.

Rickman, R., Mullen, M.J., Petre, J.E., Grieser, W.V. and Kundert, D. (2008) 'A practical use of shale petrophysics for stimulation design optimization: All shale plays are not clones of the barnett shale'. Paper Presented at the *Society of*

Petroleum Engineers Annual Technical Conference and Exhibition, 21-24 September 2008. Denver, Colorado, USA.

Ross, D.J.K. and Bustin, R.M. (2008) 'Characterizing the shale gas resource potential of devonian–mississippian strata in the western canada sedimentary basin: Application of an integrated formation evaluation', *AAPG Bulletin*, Vol.92 No.1, pp.87-125

Safari, R., Gandikota, R., Mutlu, O., Ji, M., Glanville, J. and Abass, H. (2015) 'Pulse fracturing in shale reservoirs: Geomechanical aspects, ductile/brittle transition, and field implications'. Paper Presented at the *Unconventional Resources Technology Conference*, 12-14 August 2015. Denver, Colorado, USA.

Sander, R., Pan, Z. and Connell, L.D. (2017) 'Laboratory measurement of low permeability unconventional gas reservoir rocks: A review of experimental methods', *Journal of Natural Gas Science and Engineering*, Vol.37, pp.248-279

Su, K., Onaisi, A. and Garnier, A. (2014) 'A comprehensive methodology of evaluation of the fracability of a shale gas play'. Paper Presented at the *Unconventional Resources Technology Conference*, 25-27 August 2014. Denver, Colorado, USA.

Taheri, A. and Tani, K. (2008) 'Proposal of a new multiple-step loading triaxial compression testing method'. Paper Presented at the *5th Asian Rock Mechanics Symposium*, 24-26 November 2008. Tehran, Iran.

Tarasov, B. (2010), 'Superbrittleness of rocks at high confining pressure' in *Deep Mining 2010: Proceedings of the fifth international seminar on deep & high stress mining*, Australian Centre For Geomechanics, Perth, Australia, pp.119–133.

Tarasov, B. (2011), 'Universal scale of brittleness for rocks failed at compression' in *13th International Conference of the International Association for Computer Methods and Advances in Geomechanics*, Centre for Infrastructure Engineering and Safety, Sydney, Australia, Vol.1, pp.696-673.

Tarasov, B. and Potvin, Y. (2013) 'Universal criteria for rock brittleness estimation under triaxial compression', *International Journal of Rock Mechanics and Mining Sciences*, Vol.59, pp.57-69

Tarasov, B. and Randolph, M. (2011) 'Superbrittleness of rocks and earthquake activity', *International Journal of Rock Mechanics and Mining Sciences*, Vol.48 No.6, pp.888-898

Thompson, M.E. and Brown, S.R. (1991) 'The effect of anisotropic surface roughness on flow and transport in fractures', *Journal of Geophysical Research: Solid Earth*, Vol.96 No.B13, pp.21923-21932

Tran, D.T., Pagoulatos, A., Sonderge, C.H. and Canh, N.N. (2010) 'Quantify uncertainty of rock failure parameters from laboratory triaxial testings using conventional and multistage approaches'. Paper Presented at the *44th U.S. Rock Mechanics Symposium and 5th U.S.-Canada Rock Mechanics Symposium*, 27-30 June 2010. Salt Lake City, Utah, USA.

Vajdova, V., Baud, P. and Wong, T.-f. (2004) 'Compaction, dilatancy, and failure in porous carbonate rocks', *Journal of Geophysical Research: Solid Earth*, Vol.109 No.B5, pp.1-16

Vásárhelyi, B. (2010) 'Tribute to the first triaxial test performed in 1910', *Acta Geodaetica et Geophysica Hungarica*, Vol.45 No.2, pp.227-230

Wang, F.P. and Gale, J.F.W. (2009) 'Screening criteria for shale-gas systems', *Gulf Coast Association of Geological Societies*, Vol.59, pp.779-793

Wang, J., Jung, W., Lee, Y. and Ghassemi, A. (2016) 'Geomechanical characterization of newberry tuff', *Geothermics*, [online], http://dx.doi.org/10.1016/j.geothermics.2016.01.016 (Accessed 23 May 2017).

Yarali, O. and Soyer, E. (2011) 'The effect of mechanical rock properties and brittleness on drillability ', *Scientific Research and Essays*, Vol.6 No.5, pp.1077-1088

APPENDIX A

MATHEMATICA CODE FOR ANALYTICAL SOLUTION

FOR PULSE DECAY PERMEABILITY MEASUREMENT METHOD

```
main[xD_, tD_] :=
 Sqrt[(1/(1 + β + γ) +
    2
     Sum[((Exp[-((Part[alpha, n, 1])^2) * tD] *
           (Cos[Part[alpha, n, 1] * xD] - Part[alpha, n, 1] * γ / β *
              Sin[Part[alpha, n, 1] * xD])) /
         ((1 + γ + β - ((Part[alpha, n, 1])^2) * γ / β) * Cos[Part[alpha, n, 1]] -
          Part[alpha, n, 1] * (1 + γ + 2 * γ / β) * Sin[Part[alpha, n, 1]]))
       n=2
```

```
For[i = 1, i < 2001, i++,
 For[j = 2, j < 4, j++, If[j < 3, Part[pD, i, j] = main[1, tset * (i)],
   Part[pD, i, j] = main[0, tset * (i)]]]]
For[i = 1, i < 2001, i++, Part[pD, i, 1] = tset * (i) * L^2 / κ]
For[i = 1, i < 2001, i++, Part[pD, i, 4] = tset * (i)]


Data = Import["D:\\Research\\Conventional Pulseperm\\4013-1h.txt", "Table"];

ListLogLinearPlot[{pD[[All, {1, 2}]], pD[[All, {1, 3}]]}, PlotRange → All]
pD // MatrixForm;


ListLogLinearPlot[{Data[[All, {1, 2}]], Data[[All, {1, 3}]]}, PlotRange → All]
Export["D:\\Research\\Pulsedecay\\result\\1.xls", pD]

ListLogLinearPlot[{pD[[All, {4, 2}]], pD[[All, {4, 3}]], Data[[All, {1, 2}]],
  Data[[All, {1, 3}]]}, PlotRange → All]
```

APPENDIX B

2D FEM MATHEMATICA CODE FOR

PULSE DECAY PERMEABILITY MEASUREMENT METHOD

```
Vu = 0.000005; (*cu.m*)
Vd = 0.000005; (*cu.m*)
d = 1. * 2.54 / 100; (*m*)
L = 2 * 2.54 / 100; (*m*)
ϕ = 0.1;
ϕf = 0.1;
kmd = .01; (*md*)
kfmd = 1; (*md*)
hf = d * 0.7; (*fracture width, if existed*)
μ = 1 * 10^-8; (*kPa·s*)
cg = 0.0001; (*kPa-1*)
crock = 0;
ct = cg + crock;
ϕm = (ϕf * hf + ϕ * (d - hf)) / d;
A = (d/2)^2 * Pi;
Lu = Vu/(A ϕm); Ld = Vd/(A ϕm);
ϕu = ϕd = 1;
ku = kd = 1000 * 9.869233 * 10^-16;
(*10 Darcy for the upstream and downstream vessels*)

Tf = hf * kf;
Vs = ϕ A L;
cu = cd = (160 * 10^6)^-1;
ctu = cg + cu;
ctd = cg + cd;
k = kmd * 9.869233 * 10^-16; (*m^2*)
kf = kfmd * 9.869233 * 10^-16; (*m^2*)
Diff = If[y > L, μ/ku (ϕ ctu),
   If[y < 0, μ/kd (ϕ ctd), If[y < L/2, μ/kf (ϕf ct), μ/k (ϕ ct)]]];
ContourPlot[Diff, {x, 0, 0.0254}, {y, 0, 0.0508}, AspectRatio → 2]
```

```
Needs["NDSolve`FEM`"]
Ω = Rectangle[{0, -Ld}, {d, L + Lu}];
mesh = ToElementMesh[Ω, "MeshElementType" → QuadElement,
   MaxCellMeasure → 0.000005];
mesh["Wireframe"];
```

$$\text{ufun2} = \text{NDSolveValue}\Big[\Big\{D[u[t, x, y], t] == \frac{1}{\text{Diff}}\,(D[u[t, x, y], x, x] + D[u[t, x, y], y, y]),\ u[0, x, y] == \text{UnitStep}[y - L]\Big\},\ u,\ \{t, 0, 30000\},\ \{x, y\} \in \text{mesh},\ \text{Method} \to \{\text{"MethodOfLines"}, \text{"SpatialDiscretization"} \to \{\text{"FiniteElement"}\}\}\Big];$$

```
ContourPlot[(ufun2[.01, x, y])^.5, {x, 0, d}, {y, 0, L}, AspectRatio → 2,
 AxesLabel → Automatic, PlotPoints → 100,
 PlotLegends → BarLegend[{Automatic, {0, 1}}, {Automatic, 5}],
 ColorFunction → ColorData[{"Rainbow", {0, 1}}], ColorFunctionScaling → False]
ContourPlot[(ufun2[.3, x, y])^.5, {x, 0, d}, {y, 0, L}, AspectRatio → 2,
 AxesLabel → Automatic, PlotPoints → 100,
 PlotLegends → BarLegend[{Automatic, {0, 1}}, {Automatic, 5}],
 ColorFunction → ColorData[{"Rainbow", {0, 1}}], ColorFunctionScaling → False]
ContourPlot[(ufun2[1, x, y])^.5, {x, 0, d}, {y, 0, L}, AspectRatio → 2,
 AxesLabel → Automatic, PlotPoints → 100,
 PlotLegends → BarLegend[{Automatic, {0, 1}}, {Automatic, 5}],
 ColorFunction → ColorData[{"Rainbow", {0, 1}}], ColorFunctionScaling → False]
ContourPlot[(ufun2[10, x, y])^.5, {x, 0, d}, {y, 0, L}, AspectRatio → 2,
 AxesLabel → Automatic, PlotPoints → 100,
 PlotLegends → BarLegend[{Automatic, {0, 1}}, {Automatic, 5}],
 ColorFunction → ColorData[{"Rainbow", {0, 1}}], ColorFunctionScaling → False]
```

```
Data1 = Import["D:\\Research\\FEM_Permeameter\\Analysis\\N1-4013-1H\\4013-1H.txt",
   "Table"];
Data = ConstantArray[0, {200, 3}];
For[i = 1, i < 201, i++, Data[[i, 1]] = Data1[[i, 1]]]
For[i = 1, i < 201, i++, Data[[i, 2]] = Data1[[i, 2]]]
For[i = 1, i < 201, i++, Data[[i, 3]] = Data1[[i, 3]]]
data = ConstantArray[0, {300, 3}];
For[i = 1, i < 201, i++, data[[i, 1]] = Data1[[i, 1]]];
For[i = 1, i < 201, i++, data[[i, 2]] = (ufun2[Data1[[i, 1]], d / 2, L + .001])^.5];
For[i = 1, i < 201, i++, data[[i, 3]] = (ufun2[Data1[[i, 1]], d / 2, -0.001])^.5];
For[i = 1, i < 101, i++, data[[i + 200, 1]] = Data1[[200, 1]] + i * 100];
For[i = 1, i < 101, i++,
  data[[i + 200, 2]] = (ufun2[Data1[[200, 1]] + i * 100, d / 2, L + .001])^.5];
For[i = 1, i < 101, i++,
  data[[i + 200, 3]] = (ufun2[Data1[[200, 1]] + i * 100, d / 2, -0.001])^.5];
Export["D:\\Research\\Dissertation\\Code\\FEM_Permeameter\\Case Study\\k1000.csv",
  data];
data1 = ConstantArray[0, {300, 3}];
For[i = 1, i < 201, i++, data1[[i, 1]] = 0.005 * Data1[[i, 1]]];
For[i = 1, i < 201, i++,
  data1[[i, 2]] = (ufun2[0.005 * Data1[[i, 1]], d / 2, L + .001])^.5];
For[i = 1, i < 201, i++,
  data1[[i, 3]] = (ufun2[0.005 * Data1[[i, 1]], d / 2, -0.001])^.5];
Export["D:\\Research\\Dissertation\\Code\\FEM_Permeameter\\Case Study\\k2000.csv",
  data1];
ListLogLinearPlot[{data[[All, {1, 2}]], data[[All, {1, 3}]], Data[[All, {1, 2}]],
  Data[[All, {1, 3}]]}, PlotRange → {{0.0001, 1000000}, {0, 1}},
 AxesLabel → {"t", "pD"}, Joined → True]
```

APPENDIX C

2D FEM MATHEMATICA CODE FOR STRESS-STRAIN CURVE

```
Needs["NDSolve`FEM`"]
d = 0.0254; l = 0.0508;(*Diameter&Height - m*)
YM = 17490;(*Young's Modulus - MPa*)
PR = 0.17;(*Poisson's Ratio*)
εamax = 0.006424009;
εlmax = -0.00160565;
σmax = εamax * YM;
(*σmax=108.35;*)
no = 100;(*number of points*)
rate = εamax / no * l;
α = .95;
β = -(2 εlmax)/εamax * α
(*σmax=εamax*YM*α;*)
-1 / α + 1 / β;
reg = Rectangle[{0, 0}, {d, l}];
dmesh = mesh = ToElementMesh[reg, "MeshElementType" → QuadElement]
mesh["Wireframe"]
materialParameters = {Y → YM * 10^6, v → PR};
result = RandomReal[{-1, 1}, {no, 7}];


planeStrainOperator =
  {Inactive[Div][({{0, -((Y v) / ((1 - 2 v) (1 + v)))}, {-(Y / (2 (1 + v))), 0}}.
       Inactive[Grad][v[x, y], {x, y}]), {x, y}] +
    Inactive[Div][
     ({{-((Y (1 - v)) / ((1 - 2 v) (1 + v))), 0}, {0, -(Y / (2 (1 + v)))}}.
       Inactive[Grad][u[x, y], {x, y}]), {x, y}],
   Inactive[Div][({{0, -(Y / (2 (1 + v)))}, {-((Y v) / ((1 - 2 v) (1 + v))), 0}}.
       Inactive[Grad][u[x, y], {x, y}]), {x, y}] +
    Inactive[Div][
     ({{-(Y / (2 (1 + v))), 0}, {0, -((Y (1 - v)) / ((1 - 2 v) (1 + v)))}}.
       Inactive[Grad][v[x, y], {x, y}]), {x, y}]};
```

```
planeStressOperator =
  {Inactive[Div][({{0, -((Y ν) / ((1 - ν^2)))}, {-(Y (1 - ν) / (2 (1 - ν^2))), 0}}.
       Inactive[Grad][v[x, y], {x, y}]), {x, y}] +
    Inactive[Div][({{-((Y / (1 - ν^2))), 0}, {0, -(Y (1 - ν) / (2 (1 - ν^2)))}}.
       Inactive[Grad][u[x, y], {x, y}]), {x, y}],
   Inactive[Div][({{0, -(Y (1 - ν) / (2 (1 - ν^2)))}, {-((Y ν) / (1 - ν^2)), 0}}.
       Inactive[Grad][u[x, y], {x, y}]), {x, y}] +
    Inactive[Div][({{-(Y (1 - ν) / ((2 (1 - ν^2)))), 0}, {0, -((Y) / ((1 - ν^2)))}}.
       Inactive[Grad][v[x, y], {x, y}]), {x, y}]};

StressCal[{uif_InterpolatingFunction, vif_InterpolatingFunction}, {Y_, ν_}] :=
 Block[{dd, df, mesh, coords, dv, ux, uy, vx, vy, ex, ey, gxy, sxx, syy, sxy},
  dd = Outer[(D[#1[x, y], #2]) &, {uif, vif}, {x, y}];
  df = Table[Function[{x, y}, Evaluate[dd[[i, j]]]], {i, 2}, {j, 2}];
  mesh = uif["Coordinates"][[1]];
  coords = mesh["Coordinates"];
  dv = Table[df[[i, j]] @@@ coords, {i, 2}, {j, 2}];
  ux = dv[[1, 1]];
  uy = dv[[1, 2]];
  vx = dv[[2, 1]];
  vy = dv[[2, 2]];
  gxy = (uy + vx);
  (*for plane stress*)
  c1 = Y / (1 - ν^2);
  c2 = (Y ν) / (1 - ν^2);
  c3 = Y / (1 - ν^2);
  (*for plane strain*)
  (*c1= Y/((1+ν)(1-2ν)) (1-ν);
  c2= Y*ν/((1+ν)(1-2ν));
  c3= Y*(0.5-ν)/((1+ν)(1-2ν));*)
  sxx = c1 * ux + c2 * vy;
  syy = c2 * ux + c1 * vy;
  sxy = c3 * gxy;
```

```
  {ElementMeshInterpolation[{mesh}, sxx],
ElementMeshInterpolation[{mesh}, syy],
ElementMeshInterpolation[{mesh}, sxy]}]

result[[1, 1]] = 0;
result[[1, 2]] = 0;
result[[1, 3]] = 0;
result[[1, 4]] = 0;
result[[1, 5]] = 0;
result[[1, 6]] = 0;
result[[1, 7]] = 0;

For[i = 2, i < no + 1, i++,
 {uif, vif} =
  NDSolveValue[
   {planeStressOperator == {0, NeumannValue[0, True]},
     DirichletCondition[{u[x, y] == 0, v[x, y] == -rate}, y == l - rate * (i - 2)],
     DirichletCondition[{u[x, y] == 0, v[x, y] == 0}, y == 0]} /. materialParameters,
   {u, v}, {x, y} ∈ mesh];

 {sxx, syy, sxy} = StressCal[{uif, vif}, {Y, ν} /. materialParameters];
 result[[i, 1]] = rate * (i - 1) / l;
 result[[i, 2]] = result[[i - 1, 2]] - syy[d / 2, 0] / 10^6;
 result[[i, 5]] = result[[i - 1, 5]] + uif[result[[i - 1, 5]], (l - rate * (i - 2)) / 2];
 result[[i, 3]] = result[[i, 5]] / d * 2;
 result[[i, 4]] = result[ [i, 1]] + result[[i, 3]] * 2;
 result[[i, 6]] = α * (rate * (i - 1) / l / ϵamax)^(α - 1) * σmax / ϵamax;
 result[[i, 7]] = 1/2 (result[[i, 2]] / σmax)^(-1 / α + 1 / β);
 materialParameters = {Y → α * (result[[i, 2]] / σmax)^(1 - 1/α) * σmax / ϵamax * 10^6,
   ν → 1/2 (result[[i, 2]] / σmax)^(-1 / α + 1 / β)};
]

Export["D:\\Research\\Dissertation\\Code\\FEM\\Poisson rev\\test1.xlsx",
 result]
```

D:\Research\Dissertation\Code\FEM\Poisson rev\test3.xlsx